

Trapped between two beams – Higher order laser mode manipulation
for cell rotation

Kai Roman Skodzek

Submitted for the degree of Doctor of Philosophy

Heriot-Watt University

School of Engineering & Physical Sciences / Institute of Biological Chemistry,
Biophysics & Bioengineering

May 2019

The copyright in this thesis is owned by the author. Any quotation from the thesis or use of any of the information contained in it must acknowledge this thesis as the source of the quotation or information.

ABSTRACT

Laser light is an exceptionally powerful tool which has been utilised across all natural sciences and engineering. The very high intensities of extremely controllable light have allowed for a diverse range of studies to be carried out. When the intensities are large enough, the act of redirecting the light can create a force which can be sufficient to move small transparent objects. In biology one application of this phenomenon forms a tool for trapping and handling microscopic cellular samples in a contactless way using two laser beams. Such a laser-based tool is the Optical Stretcher, it was invented for measuring the mechanical properties of single cellular biological samples. The work presented in this thesis built upon the Optical Stretcher and to gain expertise in the field, several different biological samples were tested using it, gaining insights into the impact of particular proteins to cell mechanics. The Optical Stretcher, along with the vast majority of cell trapping experiments utilises a rotationally symmetric laser beam, which allows the cells to be moved and held in place, but their orientation is random and subject to large fluctuations. Controlled orientation of cellular specimen can lead to improved 3D imaging of the sample and is an important field of study. Previous work has shown that it is possible to orient a cell using a specially shaped laser beam, however the experimental setups were not well suited to use in biological labs. Henceforth, this thesis investigated and engineered a Dual Beam Laser Trapping device called the Higher Order Mode Cell Rotator, in short HOMCR, in order to build a powerful all-in-fibre tool for tomographic cell rotation. The major component giving rise to the HOMCR was a polarisation controlling device that alters the state of light by squeezing on the laser fibre and inducing local changes in the polarisation profile of the laser light. By characterising this device, its capability has been shown for the first time to manipulate the two lobe higher order modes travelling in optical fibres, leading to an all-in-fibre dynamic cell rotator which was used successfully to trap and orient individual cells and larger biological samples.

ACKNOWLEDGMENTS

To my beloved parents Karin and Horst Skodzek. Without your love and support I would not be here. I feel blessed and happy to have parents like you. Meine Zeit in Schule und Bildung war wahrlich nicht immer geradlinig. Lustigerweise war Englisch eines meiner schlechtesten Fächer. Dies gehört wohl für Immer der Geschichte an. Love you both.

Graeme

My dear Graeme, as I mentioned to you before, I find the German expression of Doktorvater, again a neat compoundword, very fitting for the journey of the supervisor and the PhD-Student. I was the first and surely not the easiest and I am so thankful for your patience, amazing support and of course all the philosophical explorations we shared.

Witold

I could not imagine my time here in Scotland without the great adventures we shared. Through you I could explore climbing in new ways, not only did you teach me all I know about trad climbing but also how to really try hard. Our chats at Cathcart place always rounded the days of so well!

Frank

Frank, I will always love you. You made me feel at home in the UK. What a great soul you are.

Dom

Mein Bester, die Ferne hat uns zusammengebracht auf unglaubliche Weise. Es ist immer wieder toll mit dir die Welt zu teilen. Ohne dich würden so einige Farben fehlen. Lass die Flamme lodern! Burn bru!

Julia

Thank you for your hugs when I needed them most. The library is the place to be. Will never forget the nights and mornings at Leven Terrace. Trees! Your sense of aestethik and level of focus are inspiring, my architect of dreams.

ACADEMIC REGISTRY
Research Thesis Submission


Name:	Kai Roman Skodzek		
School:	School of Engineering and Physical Sciences		
Version: <i>(i.e. First, Resubmission, Final)</i>	Final	Degree Sought:	Doctor of Philosophy

Declaration

In accordance with the appropriate regulations I hereby submit my thesis and I declare that:

- 1) the thesis embodies the results of my own work and has been composed by myself
- 2) where appropriate, I have made acknowledgement of the work of others and have made reference to work carried out in collaboration with other persons
- 3) the thesis is the correct version of the thesis for submission and is the same version as any electronic versions submitted*.
- 4) my thesis for the award referred to, deposited in the Heriot-Watt University Library, should be made available for loan or photocopying and be available via the Institutional Repository, subject to such conditions as the Librarian may require
- 5) I understand that as a student of the University I am required to abide by the Regulations of the University and to conform to its discipline.
- 6) I confirm that the thesis has been verified against plagiarism via an approved plagiarism detection application e.g. Turnitin.

* Please note that it is the responsibility of the candidate to ensure that the correct version of the thesis is submitted.

Signature of Candidate:		Date:	25/04/2019
-------------------------	---	-------	------------

Submission

Submitted By <i>(name in capitals)</i> :	
Signature of Individual Submitting:	
Date Submitted:	

For Completion in the Student Service Centre (SSC)

Received in the SSC by <i>(name in capitals)</i> :			
Method of Submission <i>(Handed in to SSC; posted through internal/external mail):</i>			
E-thesis Submitted (mandatory for final theses)			
Signature:		Date:	

TABLE OF CONTENTS

1	Introduction.....	1
2	Background.....	5
2.1	Introduction to optical trapping of cells	5
2.1.1	Optical tweezers	7
2.1.2	Dual beam optical traps.....	9
2.1.3	The Optical Cell Rotator.....	12
2.2	Laser mode propagation in cylindrical step index fibres	14
2.3	The <i>LP11</i> mode	19
2.3.1	<i>LP11</i> mode propagation in <i>circular</i> step index fibres	21
2.3.2	Stress birefringence	22
2.3.3	<i>LP11</i> mode generation in <i>circular</i> step index fibres	23
2.3.4	<i>LP11</i> mode propagation in <i>elliptical</i> step index fibres.....	25
3	Investigating cellular mechanical properties via the Optical Stretcher.....	27
3.1	Working principle of the Optical Stretcher	27
3.2	Comparison to other cell rheology techniques	31
3.3	Methods	33
3.3.1	Optical Stretcher fabrication and operation.....	33
3.3.2	Cell culture and treatment	34
3.3.3	Data analysis.....	35
3.4	Findings revealed by the Optical Stretcher	35
3.4.1	Erythrocytes treated with surface acoustic waves are mechanically un-affected	36
3.4.2	U87MG glioblastoma cells containing PTEN are stiffer	37
3.4.3	HEK-293 FUS mutant cells differ in their deformability from WT FUS.....	41
3.4.4	Stiffening effect of <i>Lmna</i> on nuclear deformability.....	44
3.5	Discussion	46
3.6	Conclusion	48
4	Higher-order mode manipulation for cell rotation	51
4.1	Overview of different <i>LP11</i> mode manipulation techniques	52
4.1.1	By fibre grating	52
4.1.2	By fibre loop paddles.....	53
4.1.3	By Spatial Light Modulator	53

4.1.4	By photonic lantern	54
4.2	By Piezo fibre squeezer based polarisation controller (PCD)	54
4.3	Methods	55
4.3.1	Experimental setup.....	56
4.3.2	Characterising the mode signal	58
4.3.3	Mode selection	60
4.4	Results	61
4.4.1	First use of the PCD	62
4.4.2	State of polarisation	64
4.4.3	Polarisation controller voltage ramp	65
4.4.4	Full range raster scan.....	67
4.4.5	Repeatability in retardance	68
4.4.6	Full range of angles by actuating one piezo	71
4.4.7	Repeatability of selected modes	72
4.5	Discussion	74
4.6	Conclusion	76
5	Trapping and rotating in a Higher Order Mode Cell Rotator (HOMCR)	77
5.1	Orienting living cells in suspension	78
5.1.1	Tools for cell rotation	78
5.1.2	Orienting living cells using dual beam laser traps	82
5.2	Integration into a trapping device	85
5.2.1	DBLT out of a PDMS microfluidic chip	86
5.2.2	PDMS chip manufacture & mode calibration	87
5.2.3	Two ways to open dual beam laser trap devices.....	89
5.2.4	In-situ mode calibration	93
5.2.5	Thin mirror deposition.....	96
5.2.6	Cell culture.....	96
5.2.7	Data acquisition	97
5.2.8	Object tracking	97
5.3	Results	97
5.3.1	Rotating in a PDMS chip	97
5.3.2	Trapping in open dual beam laser traps	99
5.4	Successful rotation of K562 cell in an open-PDMS DBLT	103
5.5	Discussion	106
5.6	Conclusion	107

6	Trapping of multicellular objects.....	108
6.1	Trapping and manipulating of cell clusters in an open ferrule trap	109
6.2	Trapping and manipulating of Alginate beads in an open ferrule trap	110
6.3	Discussion	112
6.4	Conclusion	113
7	Conclusion & future outlook	114
8	References.....	120

GLOSSARY

AdOx – Adenosine Dialdehyde

AFM – Atomic Force Microscope

ALS – Amyotrophic Lateral Sclerosis

AR – Augmented Reality

CCD – Charged-couple device

DAQ – Data acquisition device

DBLT – Dual Beam Laser Trap

DMEM – Dulbecco's Modified Eagle Medium

DMF – Dual mode fibre

FBS – Foetal bovine serum

FTD – Front Temporal Dementia

FUS – Fused in sarcoma

HE (EH) – Hybrid laser mode

HEK293 – Immortalised human embryonic kidney cell line 293

HepaRGTM – Immortalised human hepatocyte cell line

HOMCR – Higher Order Mode Cell Rotator

ID – Inner diameter

K562 – Immortalised human leukaemia cell line

LP – Linearly polarised laser mode

LPG – Long period fibre grating

MAF – Mouse Adult fibroblast cell line

OD – Outer diameter

OS – Optical Stretcher

OT – Optical tweezer

PBS – Phosphate-Buffered Saline

PCD – Polarisation control device

PDMS – Poly(di-methyl siloxan)

PMMA – Poly(methyl methacrylate)

PTEN – Phosphatase and tensin homolog

RBC – Red blood cell

ROI – Region of interest

SDS – Sodium dodecyl sulphate

SLM – Spatial light modulator

SMF – Single mode fibre

TE – Transverse electric

TEM – Transverse electro-magnetic

TM – Transverse magnetic

VR – Virtual reality

LIST OF FIGURES

Figure 2–1: A light ray incident on a surface between two media of different refractive indices.	6
Figure 2–2: Ray diagram schematics of optical trapping systems.....	8
Figure 2–3: Resulting forces of fibre alignment in DBLTs.....	10
Figure 2–4: The Optical Cell Rotator (OCR).	12
Figure 2–5: Mode propagation in circular step index fibres.....	14
Figure 2–6: The possible laser modes inside a step index fibre of cylindrical core are drawn dependent on the V parameter..	16
Figure 2–7: Mode propagation in two step index fibres with two different core sizes..	18
Figure 2–8: Examples of the LP_{lm} modes.	19
Figure 2–9: Beam profiles of guided wave modes in a DMF.....	21
Figure 2–10: Stress on a laser fibre induces anisotropy in the material structure.	22
Figure 2–11: LP_{11} mode generation in dual mode fibre.....	24
Figure 2–12: Advancing eccentricity favours the mode propagation of LP_{11} modes over ring modes.....	25
Figure 3–1: The concept of the Optical Stretcher (OS).	29
Figure 3–2: Different cell rheological measurement techniques.....	30
Figure 3–3: Deformability measurements on erythrocytes treated with SAW-waves vs. the control group, using the OS.	36
Figure 3–4: PTEN inhibits the cell invasion in surrounding tissue.....	37
Figure 3–5: Three different types of U87 glioblastoma cells investigated in initial OS experiments.	38
Figure 3–6: Comparing the U87MG PTEN transduced and the U87 GFP transduced control group showed statistical significance.	40

Figure 3–7: Mutations in the FUS gene can lead to cytoplasmic aggregates of FUS protein. HEK293 cells with different FUS- mutations and a GFP control are presented above.....	41
Figure 3–8: Four HEK-293 cell types with different contents of the FUS gene and FUS gene mutations measured in the OS.....	43
Figure 3–9: AdOx treated HEK293-FUS WT cells are investigated in an OS.....	44
Figure 3–10: To investigate the effect of Lmna on cellular deformability three MAF cell types were compared.....	45
Figure 3–11: MAF Lmna knockout cells are compared to wild type cells in the OS....	46
Figure 4–1: Different LP11mode manipulating techniques.	52
Figure 4–2: Working principle of the piezo fibre squeezer based mode manipulation. .	55
Figure 4–3: Schematic of the setup for mode calibration.....	57
Figure 4–4: Experimental setup for mode manipulation and characterization.	58
Figure 4–5: Four examples of LP11modes and their characterisation.	59
Figure 4–6: The cumulative sum of all modes above the threshold of 0.5 (orange) and the mode quality histogram give insight in the distribution of modes and help to adjust the quality threshold to obtain a higher amount of high quality modes.	61
Figure 4–7: The first performance test of the polarisation controller for higher order mode manipulation.....	62
Figure 4–8: Both possible degenerate polarisations of the LP11 mode were observed.	63
Figure 4–9: The raster scanning procedure of the PCD explained.....	65
Figure 4–10: Comparison of differently sized raster scans.	67
Figure 4–11: Repeated patterns in raster scan.	69
Figure 4–12: Adding a defined voltage $V_{\pi}=1.16V$ to the position in V_1, V_2, V_3, V_4 in the raster scan can result in recurring mode examples.	70
Figure 4–13: A monotonic change in mode angles over the range of 180° , whilst only operating V_1	71
Figure 4–14: Reproduction of signals of a dual lobe shape rotated around 180°	72

Figure 4–15: More accurate reproduction of rotated laser modes.	74
Figure 5–1: The idea of the HOMCR.	78
Figure 5–2: Methods for non-contact single-cell rotation.	79
Figure 5–3: Various methods of sample rotation.	81
Figure 5–4: Principles of cell rotation using DBLTs.	83
Figure 5–5: The three types of Dual Beam Laser Traps utilized in this piece of work are displayed.	85
Figure 5–6: a) A PDMS based trapping device cut in half with fibre inserted.	88
Figure 5–7: From manufacturing a PDMS based DBLT to an in-situ mode calibration enabled HOMCR.	90
Figure 5–8: The process of building an open ferrule trap.	91
Figure 5–9: In-situ mode calibration using a custom built mirror.	93
Figure 5–10: Schematic showing the in-situ mode calibration using an E-beam coated Aluminium mirror in an open-ferrule DBLT.	94
Figure 5–11: Mirror manufacturing via e-beam evaporation.	96
Figure 5–12: A cell cluster of two cells trapped in a rotating DBLT, the HOMCR.	98
Figure 5–13: Misaligned fibres lead to an Optical Spanner.	99
Figure 5–14: Fibre misalignment can cause trapped sample to alternate between semi-stable trapping positions.	101
Figure 5–15: The successful rotation of a K562 cell by 540° degrees is displayed. ...	103
Figure 6–1: Trapping of a cell cluster in an open-ferrule trap.	108
Figure 6–2: The trapping and manipulating of a 100µm wide HepaRG™ cell cluster in an open-ferrule trap.	109
Figure 6–3: Trapping of printed Alginate beads with HepaRG™ cells enclosed.	110
Figure 6–4 A more homogeneous refractive index distribution leads to stable trapping.	112

1 INTRODUCTION

One important aspect of bio-physics is the adaptation of tools and techniques from physics and expand them into a new environment, the biological lab, in order to bring fundamental biology forward. In this piece of work, the tools of laser-physics and optical fibre telecommunication were combined to develop a device that enables precise cell orientation for 3D microscopy.

Cells, the smallest / most fundamental self-replicating element in nature, are commonly referred to as the building blocks of life¹. Despite their small size, human beings for example, are composed out of a trillions of cells², they form a complex network of structures and interactions, which science is only the verge of piecing together. A deeper understanding of the cellular nature will lead towards solutions to the riddles of life and death. One of the biggest scientific challenges of the 21st century is to learn enough about cancer in order to discover and produce possible treatments to cure it. One approach to study it, is to grow various forms of cancer cells *in vitro* outside of the body in a lab setting where they can be studied in detail without endangering patients. Cells growing in a lab are clearly in a very different environment than those which are investigated within a patient, requiring the *in vitro* culture methods to become more and more sophisticated to mimic life sufficiently. Printing tumours³⁻⁵ and their surrounding environment allows the study of them in an *in vitro* environment closer to the reality *in vivo*, this is an interesting development. Cancer cells rarely exist isolated, rather they are embedded in extracellular matrix surrounded by healthy tissue. By printing tumours from cells which have been grown from a patient sample, it would be possible to study the effectiveness of different treatments⁶, parallelised by multiplying the cells in culture. This way, the best personalised treatment could be found without inconvenient trials causing unnecessary side effects troubling the patient's health.

When imaging multi-cellular sample such as tumours or embryos under the microscope, limitations in their study persists:

- 1) Light is focussed by an objective so that an imaged point becomes elongated along the optical axis, known as point spreading (up to 4 times). Therefore, the obtainable resolution is not the same in all three dimensions.

2) This limitation and the attached 3D resolution drawback raises when the 3D information is gathered using z-stacking (images captured each differing in the z-position, the position along the optical axis, by a difference of $+\Delta z$ leading to a build-up of a 3D reconstruction of the whole sample). The stepsize of the motor driving the objective is generally larger than the resolution in the imaging plane.

3) A microscope's objective has a maximal working distance. For large samples the objective might not reach the distant parts of the object.

4) For increasing sample size, there are more cells which the microscope is trying to image through, and this lowers the achievable imaging quality. The more cells the subject being imaged is from the microscope's objective, the poorer the imaging quality, as the light is scattered from all the cells in-between. The intensity of transmitted light decays exponentially with the sample depth due to the scattering events⁷. For imaging deeper and deeper into biological sample, this results in high light intensities necessary.

One way to improve this for large samples is to chemically or cryogenically solidify the sample and then slice sections of it⁸. Such techniques kill the sample and may change the sample object. As the biological sample is dead after, only one time-point without any dynamics can be captured, and because of the very unique nature of each living system, fixing multiple samples at different time-points does not necessarily allow the reconstruction of dynamics, thus imaging of live biological sample is often preferred.

Another technique to circumvent some of the perturbation, which is exploited in this work, is by rotating the specimen and imaging it from different directions, this way the length of necessary travel of the collected light, for a spherical multi-cellular object is always at maximum of the radius, rather than the diameter. The necessary light intensity and the perturbation will become only a fraction (4). Halving the objectives maximal travel might also solve the problem 3) of a finite working distance.

Drawbacks 1) and 2) are solved as the microscope always captures in the highly resolved imaging plane. If rotation is executed perpendicular to the imaging axis and around at least 180° , the whole sample's 3D information can be gathered, without any need to change the focus of the objective.

In this thesis, the development of a capable tool for the goal of precise sample orientation is researched. To get a good grip on cellular sample, fragile in nature, a method without harsh physical contact is preferred. The majority of the things we

humans perceive is touched by light and this light is reflected into our eyes (or emitted directly from its source). This general life experience of light makes it hard to believe, that photons can be used for more than just imaging. Yet, light can actually trap and hold microscopic objects! The versatility of using light as a tool is immense.

Laser light already revolutionised modern life by permeating through many layers of our everyday life: From the checkout machine in the supermarket that reads our products' barcodes, to our computers and smartphones that are powered by semi-conductors produced using laser based photolithography⁹ to our automobiles that were assembled via laser-welding¹⁰ - a modern humanity without the advancements brought by laser technology is unimaginable.

Likewise, laser development allowed the scientific community to intensify the research into hard questions of all major fields of science. Laser technology has proven to be well capable of providing both extremes, melting metal and holding biological specimen safely. The basis for this work were laid in 1970, ten years after the first laser was presented by Maiman¹¹, when Ashkin showed the possibility to trap micron-sized particles in liquid stably, using two co-axially aligned laser beams¹². The light trap formed by two co-axially aligned laser beams will henceforth be referred to as a Dual Beam Laser Trap (DBLT). This discovery lead Ashkin on his path to research laser trapping further and in 2018 he was awarded the Nobel Prize in Physics 2018: "For optical tweezers and their application to biological systems".

DBLTs have been shown to be capable of more than simply holding an object in place, after their initial introduction they were later refined further to be even capable of measuring cellular deformability by increasing the laser power in the tool called the Optical Stretcher (OS)¹³. Results obtained during this doctorate investigate the deformability of different cell populations via the OS are presented in Chapter 3 after the background of the whole work is laid out in Chapter 2.

Modifying the DBLT even further, by shaping the laser light of one of the beams in its profile can add another layer of control and option to manipulate the trapped objects. Using a purposefully shaped beam profile which orientates the trapped sample reliably, then by having full control over the orientation of this signal, it will allow for control over the sample orientation. The tool investigated in this project to shape the laser signal for the creation of an all-in-fibre cell rotating device (all components are kept in fibre, no free space optics) is a polarisation control device (PCD) based on piezo-

electric fibre squeezing¹⁴. This form of device is common in fibre optic telecommunication but is novel in laser beam shaping and is the subject of study in Chapter 4. After showing the ability of this approach to orient a laser signal in the desired manner, Chapter 5 shows the journey towards different DBLTs enabled to facilitate the PCD, merging the beam shaping and laser trapping into one device, leading to the controlled stepwise sample rotation that proved the success of the project (shown in Section 5.4). This device will be named Higher Order Mode Cell Rotator (HOMCR).

As motivated in the first paragraphs of this introduction, multi-cellular objects are a prosperous sample for 3D tomography where sample rotation lowers the perturbation light experiences from the areas of the sample the furthest away from the objective. Chapter 6 presents first results of DBLTs that are capable of holding larger cellular objects. In future work these devices will be utilised to gain 3D data to study fascinating multi-cellular objects.

Representing 3D data is about to fundamentally change in the years to come. For decades, representation of data was bound to a two dimensional plane on paper or later the computer screen. While attempts have been previously made to change this via stereo head-mounted display, the human brain did not evaluate the quality of those representation as good enough to fully dive into it and experience this form of 3D as close to a second reality¹⁵. Technology has improved massively ever since and is on the verge to revolutionise humanity's experience of 3D on screen. With modern head-mounted displays for Virtual Reality (VR) that offer a large field of view and high-resolution panels, the viewer can experience 3D data in an immersive and thus more engaging way¹⁶. VR finds itself already widely employed in different fields of education and training such as medicine¹⁷, surgery¹⁸ and the military. But also other technologies like Augmented Reality (AR) give the user a genuine feel for the true nature of the studied object. By moving a phone or tablet around a virtual object the AR software views the object as in fact the observer moves around it. Studying three dimensional biological objects with a true feeling of their spatial nature, while even being able to zoom in, take a virtual walk inside and explore every detail is surely a tool scientist of past decades were dreaming of. The future is prosperous.

2 BACKGROUND

The two pillars supporting the research presented here are the trapping of biological cells using counter propagating laser light emanating from optical fibres, and the beam shaping of laser light within such optical fibres, also referred to as higher order mode manipulation. These two areas of research have been combined in order to controllably orientate microscopic biological specimens, primarily for imaging. While the laser-trapping holds the sample in place, altering the laser signal by higher order mode manipulation orients the sample to image it from different sides. Optical trapping by two counter-propagating laser beams is a well-established technique and has been utilised to answer complex biological questions¹⁹. The approach has also been previously used to hold and rotate cells^{20,21} using complex beam shaping apparatus and precision alignment²¹ which limits the usability of the technique. By using novel higher-order mode manipulation, the required beam shaping can be achieved without such complex apparatus. The laser signal to align and orient the specimen, has two intensity maxima and will be referred to as a dual-lobe signal. To obtain this signal at different orientations to further align the sample accordingly, an approach based on piezo-electric fibre squeezers¹⁴ is chosen. The fibre located between fibre squeezers experiences different stresses dependent on the applied voltage, this alters the propagation of the light leading to a change in the signal leaving the facet. To understand the idea of stress based higher order mode manipulation the general propagation of laser light in circular step index fibres of different core size will be motivated (Section 2.2) and how this can lead to a trapping light pattern that is capable of aligning the sample. Yet, to control the sample before rotational alignment can take place, the principles of dual beam laser trapping are essential and discussed below in Section 2.1. After the main background is presented the first Chapter of the results Section will highlight work carried out leading to fond experience in the broader field of dual beam lasing for biology, using a well established concept, the Optical Stretcher²².

2.1 INTRODUCTION TO OPTICAL TRAPPING OF CELLS

Cells generally have a slightly higher refractive index than their surrounding culture medium. As light moves through different refractive indices, it refracts and can change the direction of travel which thus changes the momentum of the light. Further, considering a light beam incident on a surface between two media with different refractive indices, the incident beam carries momentum $p_i = \frac{E \cdot n_1}{c}$. The momentum is

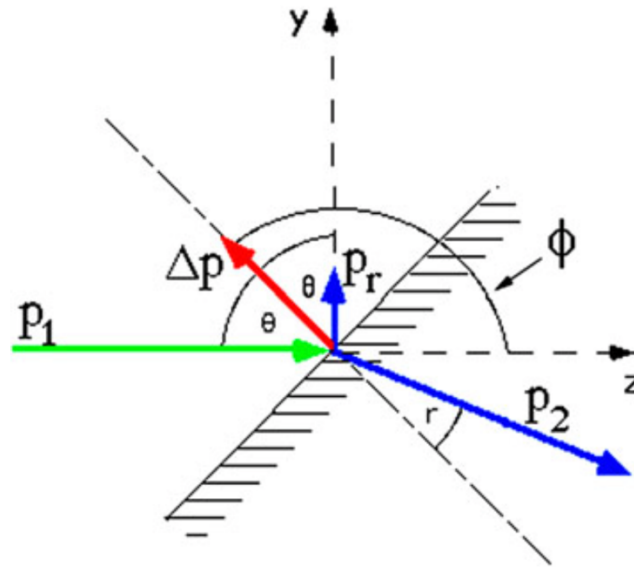


Figure 2–1: A light ray incident on a surface between two media of different refractive indices. The incident light ray (green) carries momentum p_1 which splits into the in blue highlighted parts of transmitted p_2 and reflected light p_r . Adapted from Guck et al.²³.

proportional to the beam's energy E , the refractive index n_1 of the medium divided by the speed of light. This momentum splits at the interface between two different refractive index materials into a reflected and transmitted fraction. This scenario is motivated in Figure 2–1. An incident light beam (green) hits the surface between two media of different refractive indices and a fraction of the light gets reflected (red) and refracted (blue). In this work the laser trapping of cellular sample was the subject of discussion thus, the reflection of light plays a minor part due to the similarity in refractive indices and will be omitted in the following. The light's refraction (blue) depends on the incident angle θ and the refractive index difference. The maximal change in momentum is achieved when incident light hits the surface perpendicularly. As the refractive index of a cell is generally higher than the surrounding media the light's momentum inside the cell increases, $p_2 = \frac{E \cdot n_2}{c} > p_1$. Momentum has to be conserved, therefore the cell will experience a force to balance the momentum change. This force is usually negligible, but when considering microscopic objects such as cells, and high intensity light sources such as lasers, the force can overcome buoyancy and drag, as well as suppress the normal Brownian motion experienced by a microscopic object as molecules of the surrounding medium collide with it. These forces then hold, or "trap" the cell in place, and if the light is moved, allow the cell to be moved around by the force of the light. Ashkin observed and described these forces²⁴ as show in Figure 2-1i) which shows the refraction of light rays passing through a spherical particle symbolising a cell to help demonstrate this concept.

Laser light with a Gaussian beam profile is propagating from left to right. The particle is of higher refractive index than its surrounding and is situated off-centre in reference to the laser beam. The ray diagrams for **a** and **b** show how the incident light is refracted twice when entering the cell and leaving it. The reflection of the light, that is dependent on the transparency is not drawn. The refraction in **a** and **b** result in the forces F_a and F_b . Beam **a** is of higher intensity as indicated by the gradient of the Gaussian profile (TEM₀₀ in Figure 2–2) thus F_a is of bigger magnitude than F_b and so the cell is drawn towards the centre of the beam axis. The force component perpendicular to the laser beam, but in line with the gradient of the laser light's profile, is summarised in the net force F_{grad} (gradient force). The force component parallel to the laser beam is accelerating the particle perpendicular to F_{grad} and called scattering force F_{scat} . Using a second laser co-axial with the first one, the scattering force can be balanced out as shown in Figure 2–2 ii). Stable trapping in between the two beams can be achieved, and was first realised 1970 by Ashkin et al.¹² in their fundamental publication pioneering the field of optical trapping²⁵.

Besides linear momentum, light can also carry angular momentum caused by photon spin and orbital contributions²⁶. Considering the linear momentum of a photon $p = \frac{h \cdot n}{\lambda}$, light with helical phase fronts carries $p_\phi = \left(\frac{h \cdot n}{\lambda}\right) \times \left(\frac{l \cdot \lambda}{2\pi r}\right)$, where h signifies the Planck's constant, l the light's mode index, λ the light's wavelength, r the radial position from the beam axis and n the refractive index of the media the light travels in. While the above discussed Gaussian beam carries no angular momentum, higher order modes can. Padgett and Bowman²⁶ reviewed how using an Optical Tweezer together with vortex beams, the gyration of particles can be achieved. The next section will give a brief overview over the technique of optical tweezing.

2.1.1 Optical tweezers

Later in 1986 Ashkin et al.²⁷ demonstrated, that by using a highly focused beam, it is even possible to trap a dielectric particle against gravity with a single beam (see Figure 2–2 iv)). This technique of single beam trapping, even at times referred to as optical trapping²⁸ full stop, is today known as optical tweezing²⁹ and is a broadly applied tool in bio-physics and the most common technique of optical trapping^{25,28,30}. Looking at the

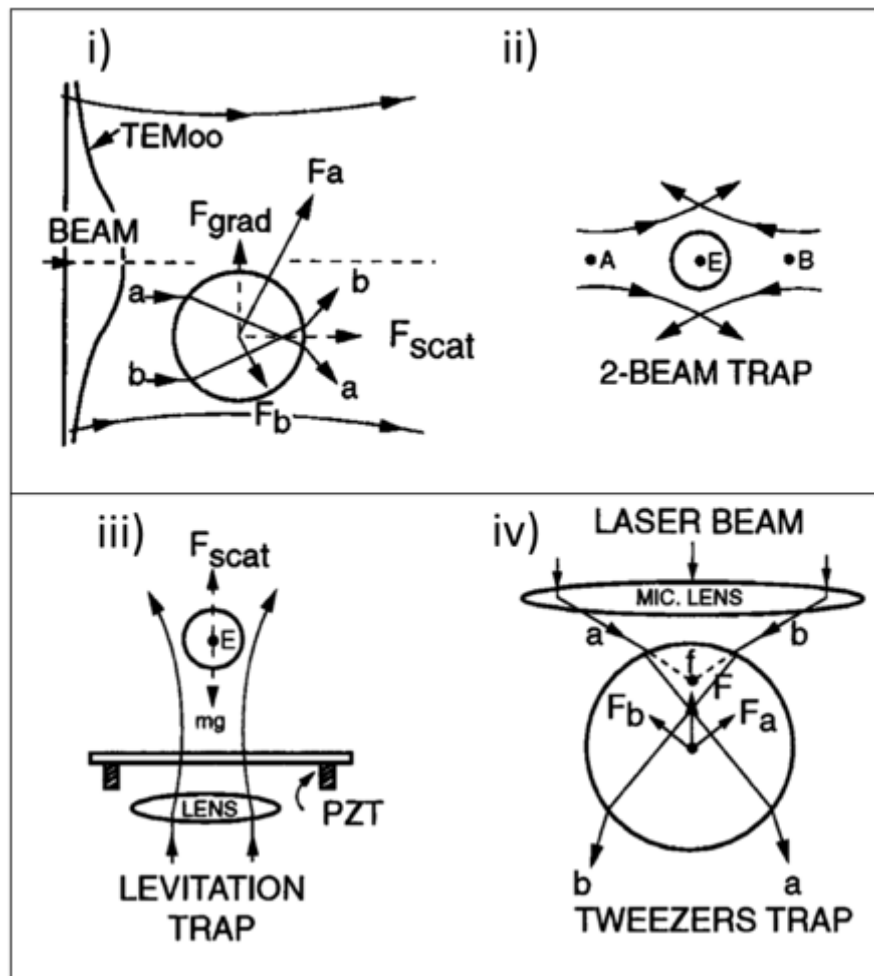


Figure 2-2: Ray diagram schematics of optical trapping systems. Forces arising from a diverging beam i): Forces from a single gaussian beam incident on a high refractive index sphere from the left. Refraction causes the change of momentum of a light ray as shown in beam path *a* and *b* and therefore a trapped particle experiences forces F_a and F_b . As of the beam centre, more light arrives at the beam path *a* and F_a is bigger than F_b . This leads to the force F_{grad} pulling the particle into the centre of the beam. When beam *a* and *b* leave the particle an additional force gets added to the forces present when entering. Both times the photons also push the particle forward which can be summarised in the scattering force F_{scat} . ii) to balance the scattering force a second beam can be used and a Dual Beam Laser Trap is formed. For completion traps with only one beam are displayed in iii) and iv). iii) F_{scat} can be also used to balance gravity and thus form a levitation trap. iv) shows the concept of optical tweezing. With the so called optical tweezer it is possible to trap cells with only one beam. The with a lens highly focused beam gets refracted when entering and leaving the particle, as discussed previously, but the forces F_a and F_b are now acting the opposite direction as before and pull the particle towards the lens as the scattering force is negligible compared to F_a and F_b . Adapted from Ashkin²⁴.

mere citations, Ashkin's later publication in 1986 studying a single beam optical trap outnumbers the original publication by far indicating its relevance. One advantage of optical tweezers (OTs) is that it can be implemented in a microscopic setup using the same objective as the imaging, no parts on the optical stage are necessary. Padgett et al. showed that light bears optical momentum and this can be used to orientate sample, the exerted torque resembling a optical spanner³¹. Using advanced beam shaping and optical tweezing, sophisticated particle manipulation as molecular motors, micromachines can be realised³². Micromachines are miniature, micron sized tools, often steered by optical forces. For various applications, Micromachines can be made dynamically reconfigurable, when for example combined with holography.

Understanding the optical force acting on non spherical objects trapped inside OTs, together with custom manufacturing particles with desired refractive index profile, via two photon polymerisation, enabled a high level of control to utilise OTs in even more creative ways. Phillips et al. demonstrated how to use OTs to create highly sensitive surface scanning probes^{33,34}.

2.1.2 Dual beam optical traps

However, laser traps with two co-axially aligned beams, Dual beam laser traps (DBLT), have advantages. In contrast to optical tweezers they do not need a highly focused beam and thus exert dramatically less optical radiation on the living specimen, and unlike OTs which have specific requirements in terms of the microscope optics and setup, the DBLT is independent of the imaging optics. Constable et al.³⁵ advanced the trap design of Ashkin's DBLTs using optical fibre in the construction, instead of more alignment intensive free space optics. Dependent on the fibre alignment of the optical trap, the trapped specimen experiences different optical forces as shown in Figure 2–3. The figures a) & b) show co-axially aligned fibres where stable trapping is possible. c) shows misalignment in the lateral dimension this causes the sample to circulate in the trapping area without a stable trapping position. For only small misalignment in the lateral dimension the circulation can be suppressed and the offset in forces induces the sample to spin around its own axis. This can also be used positively for sample rotation³⁶ which will be further discussed in Section 5.3. A misalignment in angle presented in d) forces the trapped specimen out of the centre of the trap. The use of optical fibres hugely simplifies the optical setup required to achieve a DBLT, which reduces the size and cost of using them, as well as removing potentially dangerous free-space laser beams.

In coaxially aligned fibre traps Guck et al. showed that the device can be used for mechanical measurements on suspended cells²². As the scattering forces are balanced out on both sides of the trapped specimen, increasing the intensity of the laser exerts more force, which creates a stronger trap, however because the majority of the light is refracted and not reflected, the increased scattering force can also lead to deformation in the form of cell stretching. This deformation can reveal mechanical properties of the trapped object and was widely used in the Optical Stretcher (OS)²² which will be discussed more thoroughly in Chapter 3. As discussed before, cells are very heterogeneous, which requires many similar cells to be measured to be able to make a meaningful statement about that type or population of cells. Initially, cells were loaded

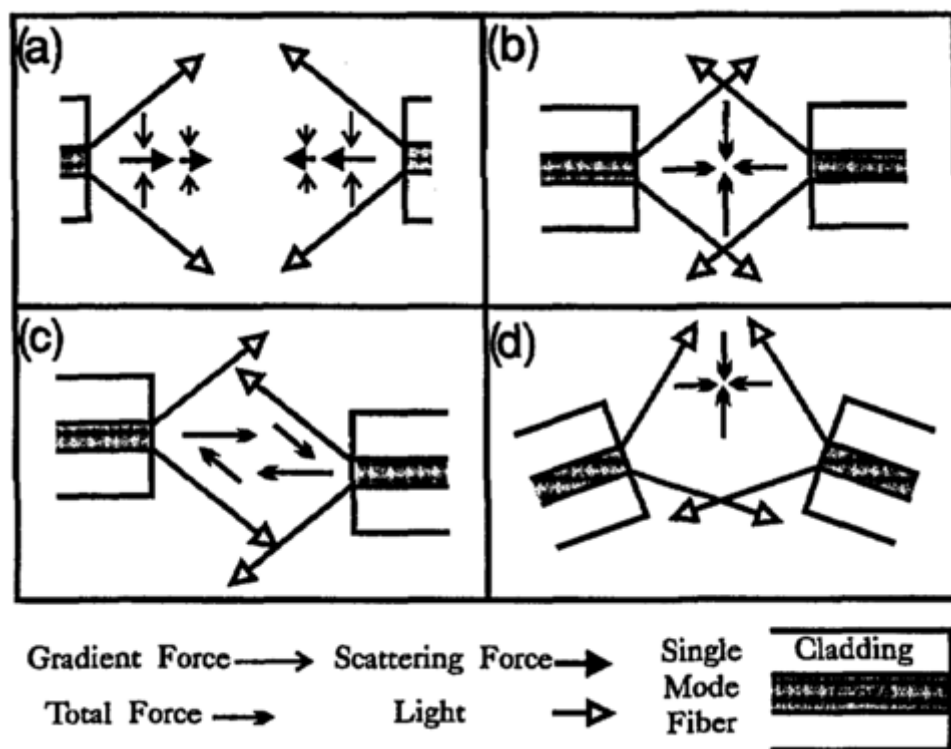


Figure 2-3: Resulting forces of fibre alignment in DBLTs. In the fundamental publication by Constable *et al.*³⁵. The first DBLT assembled using two optical fibres is presented. When the fibres are aligned co-axially as shown in (a) and (b) the optical forces balance and stable trapping can be achieved. (c) shows the forces present when the fibres are transitionally misaligned. The sample trapped in the middle will oscillate between different positions. Further when the lateral offset is very small the sample starts to rotate in plane. In (d) the fibre alignment is imprecise in the angular dimension. The point of equilibrium of forces is out of the centre, but often not practically stable and trapped objects drop out of the setup. Adapted from Constable *et al.*³⁵.

into DBLT using micropipettes by hand, to gain meaningful statistics, the DBLT was developed beyond the DBLT concept inspired by Constable *et al.*³⁵ into a microfluidic environment allowing for fast sample loading. Lincoln *et al.*³⁷ invented a capillary based DBLT using photolithography to accurately construct perpendicular grooves aligning the fibres and the capillary within which the cells were flowed, this way, cells lined up in the microfluidic channel, so one after the other could be measured in quick succession. The experimental work carried out using the OS in Chapter 3 builds upon Lincoln's design.

The faster sample loading in the OS led to meaningful statistics. Correlations of cellular stiffness in relation to cancer³⁸ were found in OS-measurements of cancerous, metastatic fibroblasts and a healthy control group. Only a few measurements ($N \leq 36$) per cell-line were needed to discriminate the healthy from cancerous cells. Further, the visco-elastic properties measured in the process of stretching different lineages of differentiated blood cells, could distinguish the two different populations confidently³⁹, showing the potential of the Optical Stretcher as a device to quickly and accurately identify cell types.

Guck et al. could even show using a DBLT, that the light guiding properties of Müller cells, present in the human eye, have similarities to optical fibre⁴⁰. A Müller cell trapped closely in between two optical fibres guides the light significantly. Even the deformability of the nucleus can be monitored using the OS. By fluorescent imaging, nuclear staining and the OS, Chalut et al. showed that the nuclear deformation is dependent on the chromatin condensation and the expression of the pluripotency marker nanog⁴¹.

For the sake of completeness, it has to be mentioned that, for the laser trapping discussed above, laser coherence did not affect the DBLTs vastly. This is not always the case and for coherent DBLTs the two (or more) beams interfere creating confined intensity maxima in a standing wave pattern. This can enhance axial trapping stability further as the gradient force pulls the trapped object into the point of highest intensity. While this form of trapping is uncommon in DBLTs used for biological trapping, it plays a larger role in the cooling of neutral microscopic particles²⁴.

At the molecular scale, the temperature of a system is proportional to the speed the objects are moving and the degrees of freedom in the objects movement. By applying optical trapping forces, it is possible to suppress motion, and thus cool the sample. To achieve cooling of neutral atoms down to the millikelvin level, a method to further take energy from the specimen can be realised taking advantage of an effect called Doppler cooling. Atoms with an energy close to their first excitation from the ground state experience a slight increase in energy when moving towards the photon that traps them, compared to when the atom moves in the opposite direction, similar to the Doppler effect. This increase in energy can be sufficient to excite the atom. Now when the atom undergoes spontaneous emission, the emitted photon carries energy and momentum and the resulting recoil of the atom is randomly distributed in direction. After many random events, the net kinetic energy of the atom decreases²⁴.

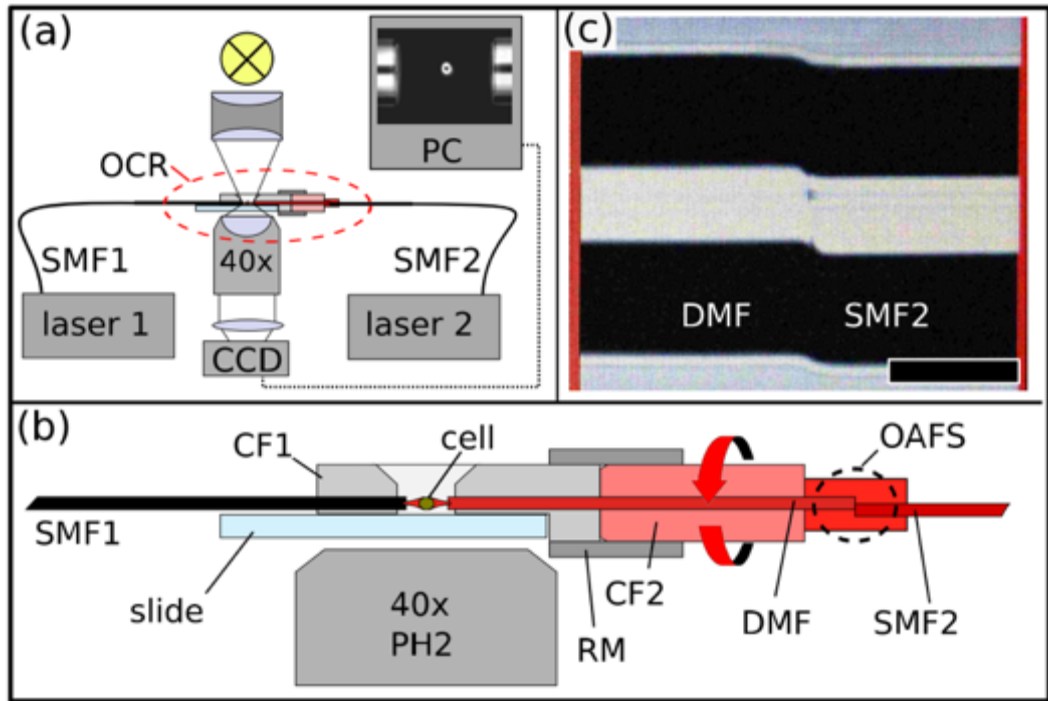


Figure 2-4: The Optical Cell Rotator (OCR). (a) Overview of the setup. A modified DBLT placed above an imaging system (40x objective & CCD camera). Laser 1 feeds into the left single mode fibre (SMF1), laser two into the right hand SMF2. Highlighted in red, SMF2 was connected to a fibre with a larger core, a so called dual mode fibre (DMF). This is magnified in (b). The DMF was spliced offset, as shown in (c) (OAFS= offset arc fusion splice) onto the SMF2, while the DMF was attached to a rotational mount (RM). The offset splice coupled more mode content of a non rotationally symmetrical mode into the DMF, while the RM enabled the rotation of the signal and specimen. Adapted from Kreysing *et al.*²⁰.

In the work presented in this thesis, the utilised optical trapping relies solely fibre optic traps. Using fibre is less alignment sensitive, cheaper and safer than laser light propagating in free space optics, moreover guiding the light inside fibres enables the manipulation of the beam all-in fibre which will be used for the desired sample orientation in this thesis. One DBLT design was the prime inspiration to the invention of the device discussed in this thesis and is discussed in the next Section.

2.1.3 The Optical Cell Rotator

Based on the concept of a DBLT a cell rotating device could be realised. Kreysing *et al.* altered one of the two beam arms of a laser trap, so it guided a laser mode that aligns a cell firmly to its non rotationally symmetric profile, by changing this beam's orientation the specimen followed the laser mode and was rotated²⁰. Most commonly in fibre based DBLTs the optical fibres are operated in single mode guidance, only one laser mode is propagating (Section 2.2). For single mode, the laser signal exiting the end of a cylindrical step index fibre resembles the rotationally symmetric Gaussian profile.

To enhance sample alignment to the trapping beam Kreysing *et al.* replaced the right hand side of the DBLT with a fibre with larger core, that enabled a two lobed laser mode to propagate (see Figure 2–4). The two lobed laser mode, also called LP_{11} mode, and how to manipulate it was crucial to the engineering of the HOMCR. Section 2.3 is addressed to learn about the mode's propagation inside circular step index fibres and Chapter 4 is dedicated to explore LP_{11} mode manipulation via a polarisation controlling device. The offset splice shown in Figure 2–3 c) couples a higher amount of LP_{11} mode into DMF and a similar arrangement will be part of the setup in this thesis

In the work of Kreysing *et al.* the right hand beam arm was attached to a rotational mount, rotating the fibre could rotate the sample synchronously. This and other cell rotating devices will be further examined in Section 5.1.2.

Because of shortcomings of the Optical Cell Rotator (see Section 5.1.2), the cell rotating device invented in this thesis was designed without any macroscopic moving parts. The sample rotation was based on shaping the laser light all in fibre. To manipulate the light inside the fibre one has to first note how the light, here referred to as laser mode, is propagating inside the fibres in use. This will be investigated in the next Section.

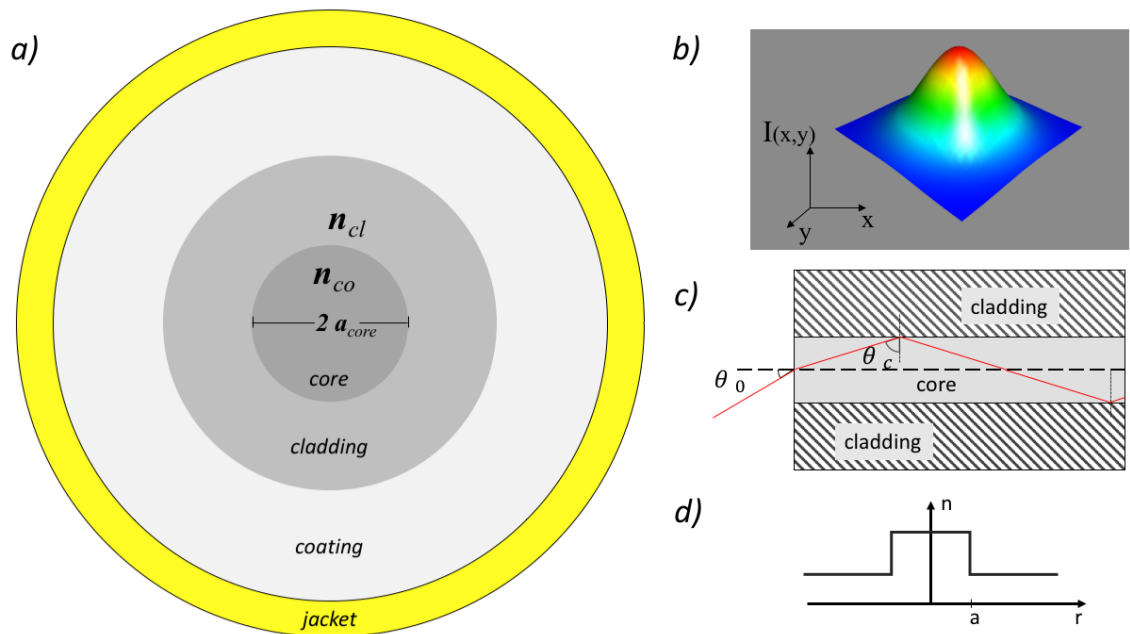


Figure 2–5: Mode propagation in circular step index fibres. a) Schematic of the transverse Section of a cylindrical step index fibre consisting of a higher refractive index core surrounded by a slightly lower refractive index cladding, and protected by a coating and jacket. Laser light propagates mainly in the core and a thin neighbouring area of the cladding. Fibres used in this thesis measured between 6.2 and $8.2\mu\text{m}$ in their core diameter, while their cladding diameter measured $125\mu\text{m}$. b) The refractive index profile in radial direction of core and cladding (dark grey and grey in a)) of a step index fibre from the middle of towards the outside is drawn. The radius of the core is “a”. c) The longitudinal Section of a circular step index fibre. Laser light can only enter/leave a fibre in an angle up to a characteristic parameter θ_0 . Inside the fibre light is reflected by total internal reflection up to a critical angle θ_c . d) The intensity profile of the fundamental mode travelling in a cylindrical step index laser fibre. The heat map, as well as the height of the Gaussian curve, display the intensity distribution in the spatial dimensions x and y . The 3D plot was designed using the program grapher (Apple Inc.).

2.2 LASER MODE PROPAGATION IN CYLINDRICAL STEP INDEX FIBRES

In the following laser mode propagation in a rotationally symmetric (cylindrical) waveguide is considered. The symmetry is important as the main purpose for laser mode manipulation that was explored in this project, was a tomographic rotation of a laser trapped specimen around at least 180° , or preferably 360° degrees. In case of a non-rotational symmetric waveguide, various orientations of light would not be guided the same way as other orientations, and the range of operation of the cell rotating device would be limited. Yet, a certain anisotropy of the trapping laser light was necessary to suppress unwanted random rotation of the specimen, while sufficient torque is needed to align the sample in desired orientation.

The most common and widely known optical fibre is the cylindrical step index fibre, which feature a higher refractive index in the core at the centre, than in the surrounding cladding. This type of fibres is solely used in the projects discussed in this thesis.

Figure 2–5 a) shows a schematic of such a fibre. The laser light propagates in the core and a thin region in the cladding, while core and cladding are protected by a coating and

jacket. The refractive index profile is shown in Figure 2–5 b). This arrangement of refractive indices, allow light within a small range of angles to be guided down the optical fibre, following the path of the core, even around bends – hence their widespread use in guiding light from one place to another. Hence, the term waveguide is commonly used to describe this arrangement. This guiding can be understood by considering total internal reflection at the core-cladding interface, which is provided for light propagating at an angle larger than the critical angle α_c (see Figure 2–5 c)). Light entering or leaving the fibre is refracted according to Snell’s law. The refractive index difference between core/ cladding and the core diameter form the boundary conditions for the light’s propagation. To predict the propagating of the light field in the fibre, the Maxwell equations can be solved for the above bespoke boundary conditions. This leads to the electromagnetic wave equations:

$$I) \left(v_{ph}^2 \nabla^2 - \frac{\partial^2}{\partial t^2} \right) E = 0 \ \& \ \left(v_{ph}^2 \nabla^2 - \frac{\partial^2}{\partial t^2} \right) B = 0 .$$

Where $v_{ph} = \frac{1}{\sqrt{\mu\varepsilon}}$ is the propagation speed of the photons, which is dependent on the permeability μ and the permittivity ε of the medium the light travels in. Relating back to the refractive index, one can exchange the constants to $v_{ph} = \frac{c}{n}$. Now, when separating the variables this leads to

$$II) \quad \left(\frac{\nabla^2 E(r)}{E(r)} - \frac{1}{c^2 T} \frac{d^2 E(t)}{dt^2} \right) = 0,$$

while $E(r)$ are the spacial dependent components of E and $E(t)$ the time dependent , respectively (one can exchange the placeholder E for B to obtain the equation for the magnetic field). The equation is only solvable when both sides equal a constant.

Therefore it is possible to conclude

$$III) \quad \frac{\nabla^2 E(r)}{E(r)} = -k^2 \ \& \ -\frac{1}{c^2 E(t)} \frac{d^2 E(t)}{dt^2} = -k^2$$

Combining I) and III) leads to the Helmholtz equation

$$(\nabla^2 + k^2) E = 0$$

For a fibre that does not exceed a certain core size and refractive index difference of core and cladding (summarised below in the generalized frequency V and plotted in Figure 2–6) the intensity of the basic electromagnetic wave travelling through the wave guide and later leaving the fibre end follows a Gaussian curve. It is referred to as the fundamental mode and an example is shown in Figure 2–5 d). Mode is a term widely

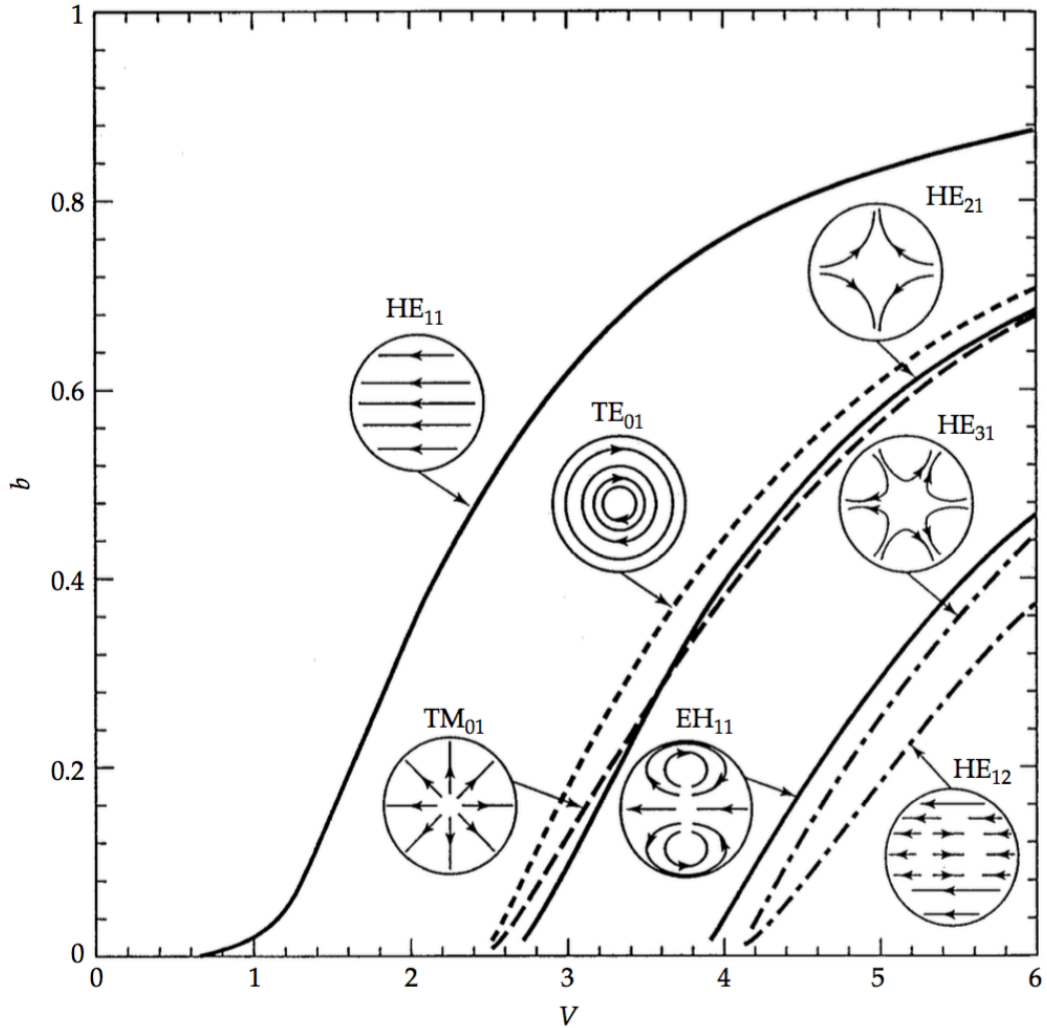


Figure 2-6: The possible laser modes inside a step index fibre of cylindrical core are drawn dependent on the V parameter. While the the polarisation maps are drawn for the modes, the intensity pattern is hard to spot. The very first mode follows a Gaussian intensity and the next three mode examples follow a doughnut shaped pattern. While the first example provides continuous polarisation vectors though the whole mode and therefore intensity pattern, the next higher order modes display a spot of zero intensity right in the centre. The intensity profiles of the first higher order modes can be studied further in the next figure. The ordinate b signifies the generalised guide index. The arrows in the figure indicate the present polarisation. The cut-off for single mode propagation of the fundamental mode HE_{11} lies at 2.405 after that the three modes TM_{01} , TE_{01} and HE_{21} are additionally propagating in the laser fibre. It is to note that TM_{01} , TE_{01} and HE_{21} can interfere with each other to form a linearly polarised mode which will be discussed in the next two figures. The next cut-off after lies at $V=3.817$. The higher order modes after this cut-off will not be of high interest in this thesis. Figure adapted from Chen⁴³.

used to describe the possible state of oscillatory systems. If a fibre only accommodates its fundamental mode, it is referred to as Single Mode Fibre (SMF), which will be a term used more often in this piece of work. The shape of the light travelling in bespoke waveguides can be calculated solving the Maxwell equations for the boundary conditions of the particular laser fibre as motivated above. For fibres with a small refractive index contrast of core and cladding the Maxwell equations can be solved in the weakly guiding approximation⁴², leading to Bessel functions.

The fibre boundary conditions can be summarised by the generalised frequency $V = \frac{2\pi a}{\lambda} \sqrt{n_{co}^2 - n_{cl}^2}$, with the refractive index of the core n_{co} , and cladding n_{cl} , the

wavelength of light λ , and the radius of the core a . Solutions of the Maxwell equation, dependent on the general frequency can be studied qualitatively in the schematics of Figure 2–6, in relation to the bV -diagram. b being the generalized refractive index: $b = \left(\frac{N^2 - n_{cl}^2}{n_{co}^2 - n_{cl}^2}\right)$; $N = \beta \frac{\lambda}{2\pi}$ with β & k noting propagation constants and the wavelength λ .

The first examples above the fundamental mode are the, under rotation invariant, Transverse Electric TE-, Transverse Magnetic TM-mode, and the hybrid modes HE and EH. The fundamental mode often labelled TEM_{00} will be referred to as HE_{11} (see Figure 2–6). It is to note that the HE_{11} mode has two orthogonal eigenstates of polarisation, one linearly horizontal and compared to this, the other linearly perpendicular, while both normal to the direction of propagation. Every other possible polarisation of the HE_{11} mode is a superposition of the two, with different phase and amplitude of the two bespoken polarisations leading to elliptical and circular polarised light. The polarisation maps indicate the direction of the electric field vector and for the fundamental mode this leads to three possible polarisations: linear, circular and elliptical. Not easily visible in the simplified polarisation maps presented above in Figure 2–6 is the magnitude of the electric field vector which is a measure for the intensity of the light, recalling the pointing vector $\vec{S} = \frac{1}{\mu_0} \vec{E} \times \vec{B}$ and relating to the intensity $I = \overline{|\vec{S}|} = \frac{|\vec{E}|^2}{Z_0}$. Opposed to the fundamental mode, that has its maximum intensity right in the centre of the fibre, the polarisation map for the next three higher order modes displays how the field vectors are opposed in the middle, leading to destructive interference and thus minima intensity. TE and TM signify propagation where either the electric or magnetic field is perpendicular to the propagation direction⁴⁴. The modes are numbered according to their *azimuthal* and *radial* mode number l and m (TE_{lm} , TM_{lm} , HE_{lm} , EH_{lm} or TEM_{lm}). The next higher order modes are guided in a fibre dependent on the core size, the wavelength of the light and the refractive indices of the material. The first three mode cut-offs are displayed for increasing V , which in the context of this work this relates to increasing the core radius for constant refractive indices and wavelength. If V is smaller than 2.405, this signifies a cut-off of the propagation of multiple modes, and only the fundamental mode is present in the fibre, therefore the fibre is operated as a SMF. As drawn in Figure 2–6 the next higher cut-off happens for $V < 3.817$ and modes of higher order can propagate beside the fundamental mode. The range of $2.405 < V < 3.817$ will be of particular

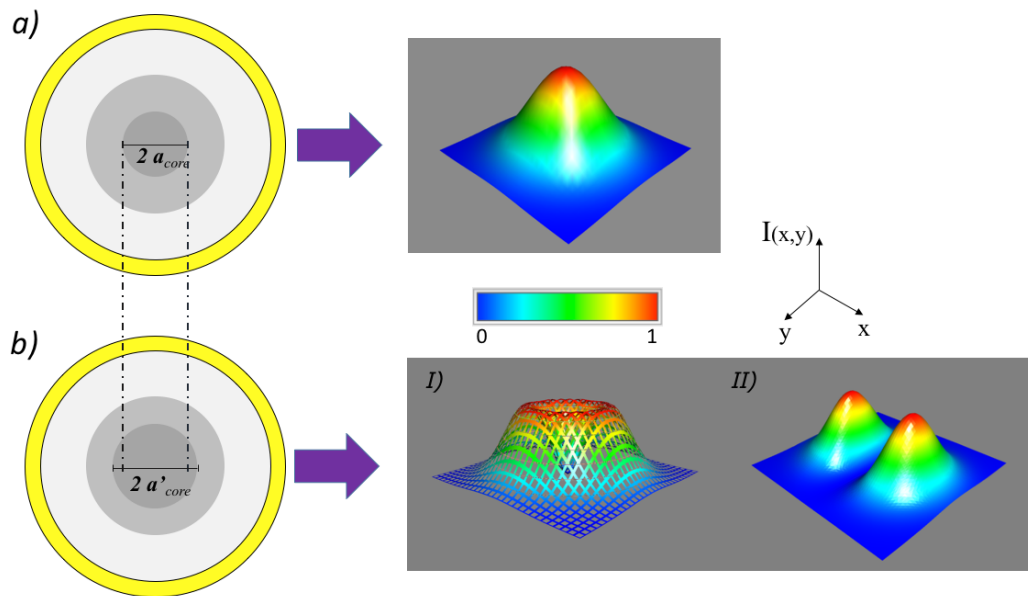


Figure 2-7: Mode propagation in two step index fibres with two different core sizes. a) The fibre is operated in single mode propagation. The intensity of the fundamental mode follows a Gaussian curve for a cylindrical core. In comparison fibre b) has a 30% bigger core, the boundary conditions enable propagation of doughnut shaped modes. I) The intensity profile is plotted in a mesh to allow the sight of the minimum in the middle of the mode. This intensity profile can be achieved by 3 different types of polarisation. Two doughnut modes of the right polarisation can superimpose to the two lobe mode on the right hand side in II). 3D plots were built using the program grapher (Apple Inc.).

interest in this thesis. A fibre being operated in this regime will be referred to as dual mode fibre (DMF) in support of the literature⁴⁵.

Figure 2-7a) and b) shows a SMF compared to a fibre with the same refractive index contrast, but a larger core radius, causing it to be operated above the first cut-off. The intensity profile of the modes shown in Figure 2-6 are plotted in Figure 2-5 b) I). TE_{01} , TM_{01} and HE_{21} form a shape often referred to as doughnut mode, also referred to as ring mode. Similarly to the fundamental mode, the ring modes are rotationally symmetric in their intensity profile and are eigenmodes of the rotationally symmetric system. An Eigen mode refers to modes that fulfil the boundary conditions of the particular fibre and are characteristic for the properties of the fibre without external forces and will propagate through the fibre without a change in intensity pattern. The next two possible modes propagating in this regime are not eigenmodes, but are formed from a superposition of eigenmodes, and so do not maintain their intensity structure as they propagate through the fibre and only occur a regular “beat” intervals. Their intensity offers dual lobes, as shown in Figure 2-7b II). The dual lobe modes are linearly polarised, either parallel or perpendicular to the line of minimum intensity and in the literature referred to as the linearly polarized LP_{11} modes. They are realised in fibre through superposition of two ring modes of different polarisation and type (transversal and hybrid modes). Respectively, either the modes TE_{01} & HE_{21} or

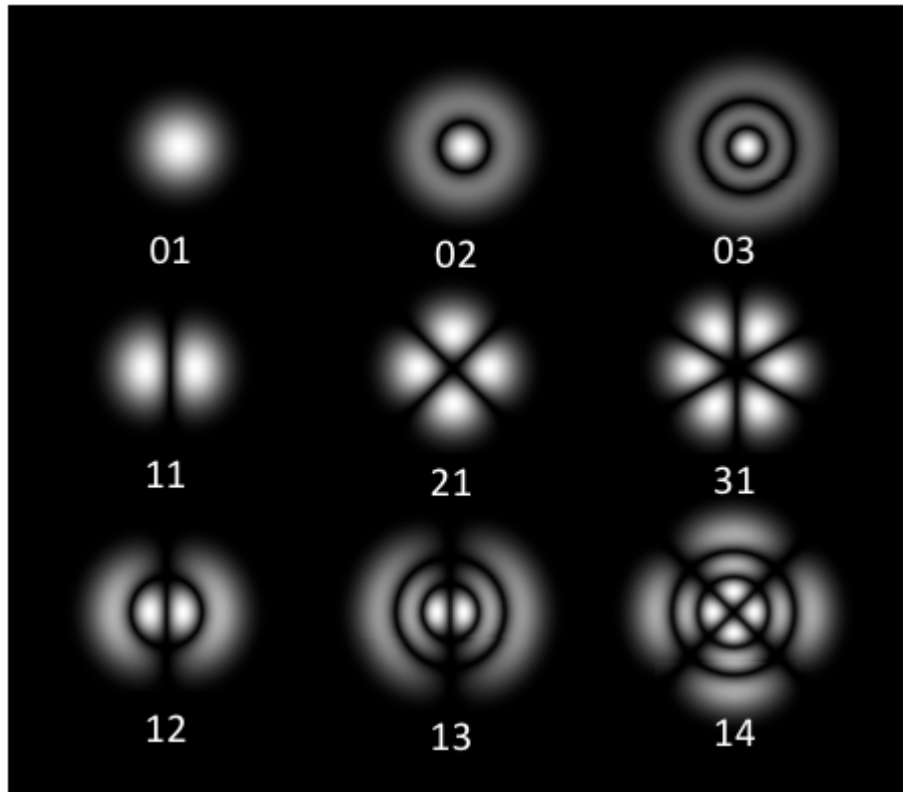


Figure 2–8: Examples of the LP_{lm} modes. $2l$ the azimuthal index l maxima exist azimuthally around the laser axis. In the radial dimension the amount of maxima equals m , the radial index. Adapted from Wikipedia.org.

TM_{01} & HE_{21} (see Figure 2–6). The two different super-positions lead to the two different types of polarisation present in LP_{11} modes. Parallel or perpendicular to the two lobes, discussed in the next Section. The intensity pattern differs fundamentally compared to the ring modes' circular symmetry, as the intensity pattern is reduced to two axes of symmetry. Namely a line from peak to peak and the line of zero intensity in between the peaks (see Figure 2–7b II). As this mode will be the basis of the Higher Order Mode Cell Rotator (HOMCR) discussed in Chapter 4 and Chapter 5, thus the next Section is dedicated to it.

2.3 THE LP_{11} MODE

The propagation of light of a given wavelength in a waveguide with a normalised frequency $V > 2.405$ allows for the guidance of modes that differ from the fundamental mode as discussed previously (see Figure 2–6). A beam with an intensity profile of non circular symmetry will orientate cellular specimen best. In a cylindrical waveguide the first higher order mode that provides this is the two lobe containing, linearly polarized, LP_{11} mode following the commonly used notation LP_{lm} by Gloge⁴⁶, l denotes the

azimuthal index and m the radial index. A mode pattern will have $2l$ intensity maxima azimuthally around the beam axis and m radially (see for Figure 2–8 examples). The notation starts with the LP_{01} mode referring to the Gaussian shaped fundamental mode with one peak of intensity in the centre. The next linearly polarized mode is the LP_{11} mode consisting of two intensity maxima located off-centre (see Figure 2–7 b) II) and Figure 2–9). Changing the rotational orientation of the two maxima proved to be capable for cell-rotation as shown by Kreysing *et al.*^{20,47}. But the LP_{11} mode is not an eigenmode of the cylindrical waveguide, instead the lowest eigenmodes of laser-light above the fundamental mode, are rotationally symmetric. Their field distributions form a ring like pattern (see Figure 2–7 and Figure 2–9) as discussed previously.

The transverse and hybrid modes have a different effective refractive index, thus propagate with a differing phase velocity. As the two set of modes are interfering this creates differing re-occurrence of the modes along the waveguide, known as the beat length of their superpositions⁴⁸. The beat length describes the characteristic length a mode travels to undergo a complete phase shift of 2π . Differing in beat lengths of two or more modes leads to changed interference of the modes at various length of travel. Further, if the orbital angular momentum⁴⁹ of the ring modes is considered, a representation where the spin collective momentum of photons is taken into account, their propagation along the optical axis can be understood as spiral. The polarisation of the transverse modes is self similar under spiral rotation, but the polarisation of the hybrid modes is not. When the different ring modes propagate onwards, this leads to a practical rotation of the LP_{11} mode, either along the optical axis, or the time axis. By controlling the phase difference of the eigenmodes, it is possible to create different output at the fibre end, including rotated LP_{11} patterns. The Section below will describe how this can be used to advantage to cast LP_{11} modes at different orientations, forming the platform for a cell rotating device presented in this thesis.

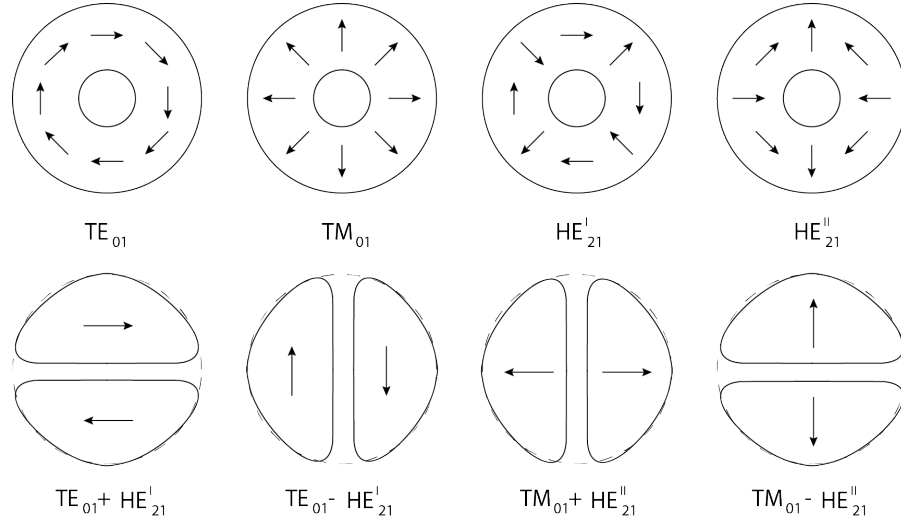


Figure 2-9: Beam profiles of guided wave modes in a DMF. The arrows indicate the orientation of the polarization. In the top row the different eigenmodes are drawn. The hybrid modes are not rotationally symmetric and the two orthogonal states HE'_{21} and HE''_{21} are indicated. Bottom row: Superpositions of different eigenmodes can yield to LP_{11} modes. Schematic inspired by Snitzer et al.⁵⁰.

2.3.1 LP_{11} mode propagation in circular step index fibres

Eigenmodes of a cylindrical, rotationally symmetric waveguide are rotationally symmetric in intensity itself, but not necessarily in polarisation. The different eigenmodes are the Transverse Electric and Transverse Magnetic modes TE_{01} and TM_{01} and the hybrid modes denoted with HE'_{21} or HE''_{21} . Earlier only HE_{21} was mentioned, the notation HE'_{21} and HE''_{21} refer to both possible degenerations of polarisation. As there are two axes of symmetry present in the HE_{21} mode, this helps simplifying the superposition of the TE_{01} or TM_{01} and HE_{21} modes leading to the two different possible polarities of the LP_{11} mode. The eigenmodes, their polarisation and their possible superpositions can be seen in Figure 2-9. TE_{01} interfering either constructive or destructive with HE'_{21} results in an LP_{11} mode with the polarisation either horizontal or vertical and hence a line of minimum intensity. This can be understood as two orthogonal LP_{11} modes of mode angle 0° and 90° , respectively. In other words, the rotated mode pattern can be

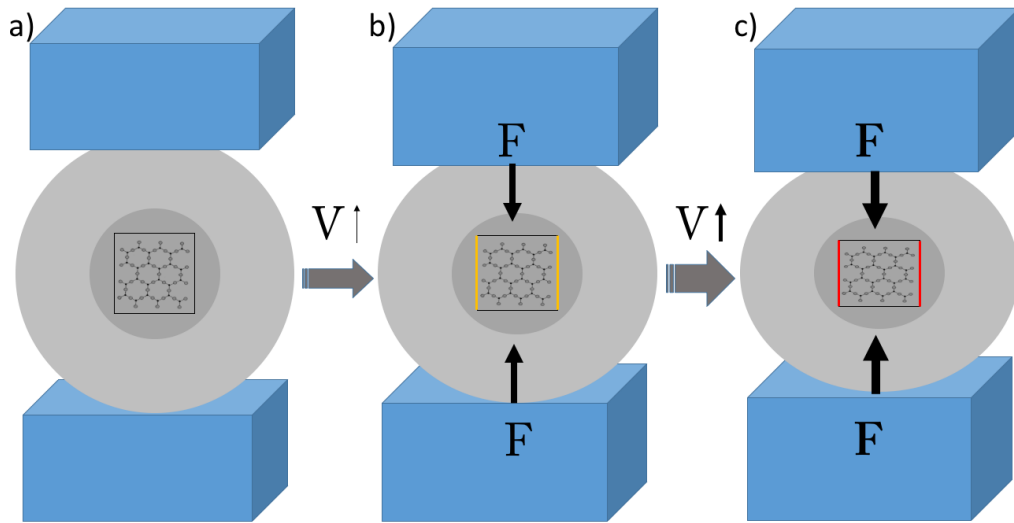


Figure 2-10: Stress on a laser fibre induces anisotropy in the material structure. An optical fibre is placed between two piezo electric elements (a). A basic schematic of the silica crystal structure is drawn inside the core of the laser fibre. The rectangle around it indicates the isotropy of the structure. Now when the voltage on the piezoelectric ceramic is increased it extends and a force F acts on the fibre, deforming it elliptically. (b). In the vertical lines of the rectangle are now compressed, indicated in yellow. Anisotropy in the laser fibre is rising and has a directionality along the compression. In c) even more voltage is applied, the forces increase and the deformation is better visible. The red lines show the ongoing compression and the anisotropy inside the laser guide. This anisotropy demands different velocity depending on the direction of the polarisation of the light. Parallel to the red lines, the propagation is slower as the material became denser, this direction is called the slow axis. Perpendicular to it the fibre is unstressed and the light's speed of propagation is unchanged. The stress and polarisation dependent propagation of light is known under the term stress birefringence and will be exploited in this thesis.

achieved when interfering the ring modes with an additional phase shift of 180° . On the other hand, the degenerate state of polarisation, where the polarisation is perpendicular to the minimum, is obtainable when the TM_{01} mode is interfering with the hybrid mode.

2.3.2 Stress birefringence

Roughly 200 years before this thesis was written, but in the very same city, Edinburgh, Sir David Brewster made an interesting observation⁵¹. By sending the light of a candle through a cured cylinder of calf derived jelly, the light was polarised into two images, but when applying stress on the jelly, Brewster could make this effect void and the light depolarised again. This can be understood concerning that the jelly cured into an anisotropic material structure and when light passed through it, the two orthogonal polarisations, parallel or perpendicular to the main material's organisation had different velocities inside the material. Parallel to the major axis of the molecules or atoms (in a crystal), travels faster than perpendicular. This effect is known as birefringence. When applying pressure, Brewster could increase the microscopic structure's isotropy again and thus cancel the birefringence of the object. In this thesis the opposite effect was utilized. External forces acting on a isotropic glass fibre can induce anisotropy in the material and thus alter the refractive index profile⁵²⁻⁵⁴. This is also known as stress birefringence⁵⁵ or photoelasticity⁵³ and the working principle of many polarisation

controlling techniques. Figure 2–10 motivates stress birefringence inside laser fibre further. Placing a laser fibre between piezoelectric elements and later extending the piezoelectric ceramics via applying increased voltage deforms the fibre, thus its crystal structure. Light polarised parallel to the deformation (indicated yellow or red) will travel slower as its perpendicular respective. If the polarisation is linear and 45° between these two axis, it can be seen as a superposition of two base vectors. One parallel to the unstressed axis, one parallel to the compressed one. Therefore, the light travelling parallel to the latter will be delayed and the whole polarisation changes from linear to elliptical until a phase delay of π where the two base vectors superposition equals again a linear polarisation but rotated. This property of an optical element is known as a half wave plate.

2.3.3 LP_{11} mode generation in circular step index fibres

Briefly, two ways for LP_{11} mode generation in circular step index fibres are discussed here. Periodic microbending and an offset launch of the fundamental mode into the fibre core. Blake *et al.*⁵⁶ coiled copper wires around two poles and placed a dual mode fibre in between, resulting in periodic microbending of the fibre. They demonstrated that this periodic micro-bending can couple the fundamental LP_{01} mode into the dual lobe LP_{11} mode. A periodic differing refractive index profile over a certain length of fibre is widely known as short or long period fibre grating (LPG). For example, Li *et al.*⁵⁷ used a mechanical LPG as shown in turquoise in Figure 2–11 i), consisting of teeth of a desired period and a plate that can exert variable pressure from the top leading to elliptical core deformation. After creating the LP_{11} modes, the rest of the setup serves the purpose of generating different ring modes selectively.

Without deforming the fibre, launching the beam offset can enhance the band-width in multimode fibers⁵⁸, as more higher order modes are attenuated. When changing the launch position, increasing the offset the fundamental mode enters the DMF, the fibre increases the LP_{11} mode content, initially (see Figure 2–11 ii) e)). This can be realised by splicing a SMF off centre onto a DMF. Further captured in Figure 2–11 ii) are the mode intensity profile of the fundamental mode in a SMF (a), compared to in a DMF (b) and launched offset into a DMF (d). While (c) shows the LP_{11} beam profile, indicating the propagating intensity off-centre, and that launching the laser beam off-set can couple into this mode. The calculated coupling efficiency of the modes, is dependent on the offset launch position and can be measured in DMF-radii.

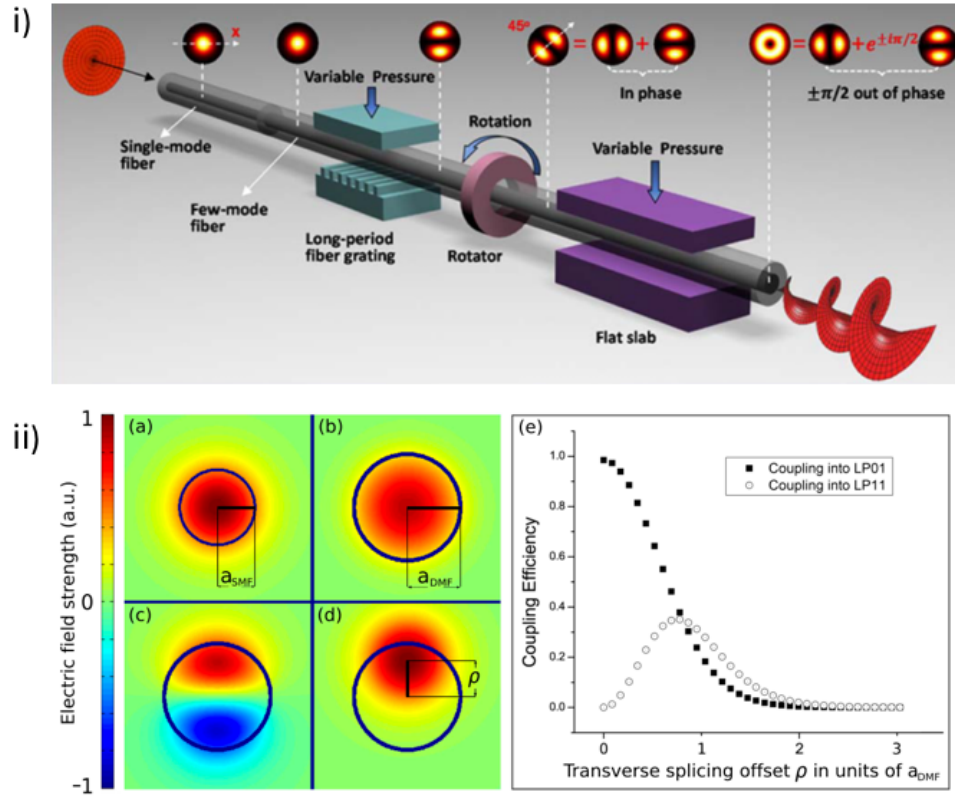


Figure 2–11: LP₁₁ mode generation in dual mode fibre. Bending the fibre periodically, as shown in i), by using a Long period fibre grating (turquoise), can generate LP₁₁ modes by adding a phase delay, through the periodic refractive index changes. Here the setup is intended to rotate ring modes, yet before the purple slab an LP₁₁ mode is orientated via a rotator, hence related to this project. Adapted from Li et al.⁵⁷. Figure ii) shows that launching the fundamental mode offset into a DMF can couple an enhanced LP₁₁ mode content into a DMF. On the left-hand side the two different mode field profiles of the LP₁₁ and the fundamental mode LP₀₁ are drawn, propagating in different fibre. As in this launch method a SMF is spliced offset onto a DMF, the mode field diameter inside a SMF is shown first in (a) and later in (b) the mode field profile of the LP₀₁ mode is launched via a straight splice into a DMF, not creating a dual lobe mode. The laser light is centred. (c) Instead, when inspecting the mode field profile of the LP₁₁ mode propagating inside a DMF, the two maxima are located off centre. (d) Depending on the offset-distance ρ, launching the LP₀₁ mode from a SMF, as shown in (a), into a DMF offset, can create an intensity profile, that one sided mimics the LP₁₁ mode as shown in (c). Optimal offset launching for a high LP₁₁ mode content dependent on the offset ρ is shown in (e). The coupling efficiency of the LP₁₁ mode (white circles) begins to overtake the LP₀₁ mode (black squares) at an offset of approximately one DMF diameter. From this graph it is obvious that for a high LP₁₁ mode content propagating in the DMF highly loss inducing splice is necessary, only a fraction of the modes is launched from the SMF into the DMF. Adapted from Kreysing et al.²⁰.

This is drawn out in (e). Just below an offset of one DMF radius, the LP₁₁ mode couples more into the DMF than the fundamental mode. An offset of approximately one DMF radius was used in this work (see Section 4.3.1) similar to Kreysing et al.²⁰. As Figure 2–11 ii) (e) shows, the overall coupling efficiency drops massively for this sort of fibre splice and a lot of laser power is lost. For this reason in the experimental setup used in this thesis the laser is split 75/25 to adjust the differing power levels in the two beam arms of the formed dual beam laser trap (see 4.3.1)

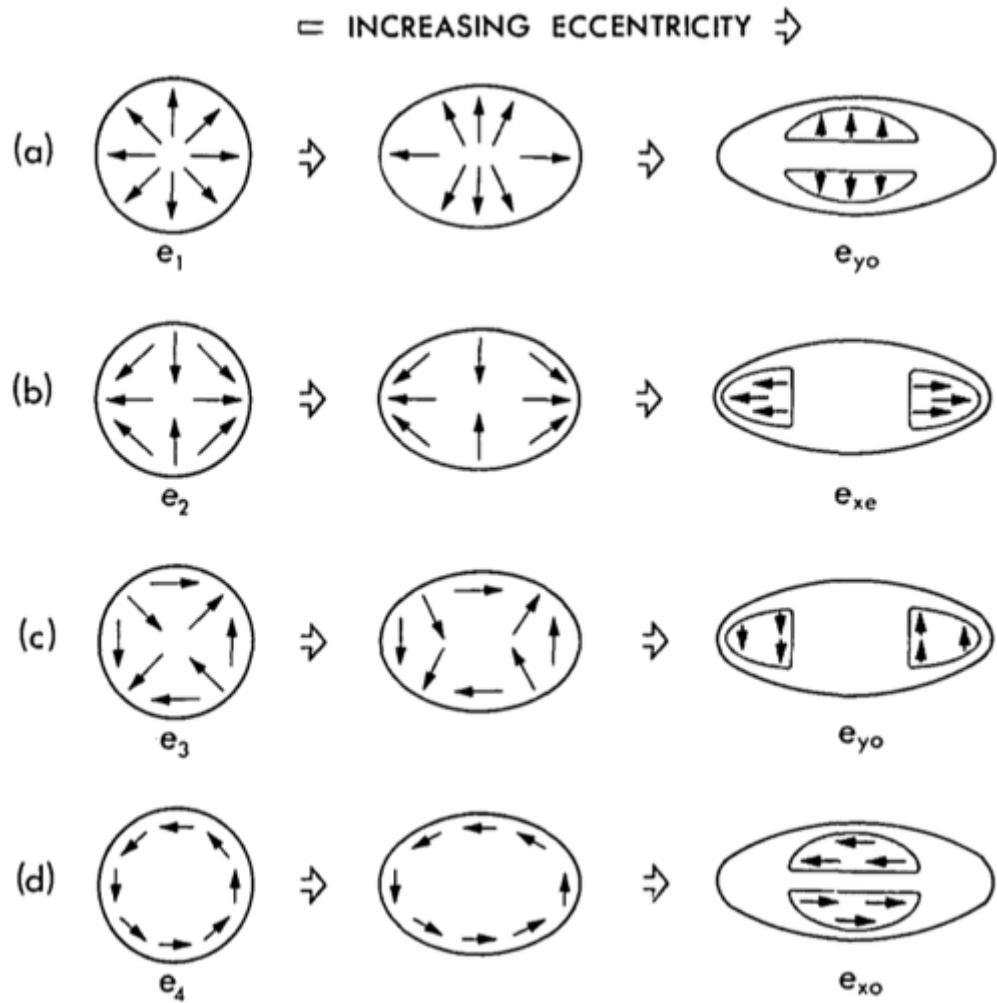


Figure 2-12: Advancing eccentricity favours the mode propagation of LP_{11} modes over ring modes. The notations of transfer as follows: $e_1 = TM_{01}$, $e_2 = HE'_{21}$, $e_3 = HE'_{21}$ and $e_4 = TE_{01}$. Adapted from Snyder and Young⁴⁸.

2.3.4 LP_{11} mode propagation in *elliptical* step index fibres

After illuminating LP_{11} mode propagation in circular step index fibres the equivalent for fibres of elliptical core is explored in the following. Although formerly the remark was made that fibres of circular symmetry are favourable for 360° mode rotation, an elliptic fibre-profile can be the result of deforming a circular fibre under uniaxial stress. Snyder and Young⁴⁸ motivate the higher order mode propagation in fibres of increasing eccentricity as favouring the LP_{11} mode over the doughnut modes, as the intensity profile follows the two fold symmetry of an ellipse. As shown in Figure 2-12 the different ring modes get stretched qualitatively in direction of the long axis and squashed along the short axis of the ellipse. This process assimilates the directions of field vectors either parallel or perpendicular to the long axis. As the elliptical geometry affects various polarisations in different ways this is a form of birefringence. Snyder and Young further point out that the transverse and the hybrid modes differ in propagation constants, moreover the difference increases further with the advancing fibre ellipticity. This directly affects the mode mixing, not only at the elliptically

deformed fibre Section, but for all reference positions in the fibre thereafter, as the modes propagate with different phase delay, interfering differently than before. To transform a circular fibre into an elliptical, stress is necessary. This can be realised using piezoelectric fibre squeezers, commonly embedded in polarisation controlling devices¹⁴. As Snyder and Young stated the induced phase delay, caused by the application of pressure onto core and cladding, can be used to change the interference of laser modes, such as ring modes. This forms one of the building blocks to mode manipulation utilised in this work, so pressure based mode manipulation will be used to orient the LP_{11} laser signal on one side of the dual beam trap (Chapter 4) and therefore be used to rotate the biological specimen.

As precise trapping and handling of cells via DBLTs is necessary for this, the concept of DBLT based cell trapping will be explored in more detail in the following Chapter via working with the cell-rheological tool, the Optical Stretcher. The research carried out with the OS did not only lead to expertise in dual beam laser trapping, but to publishable cell-rheological results.

3 INVESTIGATING CELLULAR MECHANICAL PROPERTIES VIA THE OPTICAL STRETCHER

As introduced in Section 2.1.2, the controlled application of optical forces on the surface area of a cell can be used to gain insight into cellular mechanical properties²². When the optical power in a DBLT is increased significantly, a trapped cell becomes elongated dependent on its deformability. This was first presented in the fundamental work on the Optical Stretcher (OS)²² and has since been used to investigate cell mechanical deformation. The measured deformation (strain) observed for a given increase in laser power (stress) can be linked to the composition of the cell. Different cell types or phenotypes often differ in their response to the increased optical forces. For example, cancer cells often proved to be softer in OS measurements and showed a higher responsiveness to the stresses exerted on them compared to their healthy counterparts of the same cell-type⁵⁹. This higher deformability of cancer cells can be linked to increased invasiveness into connective tissue and therefore the potential for a cancer to form metastasis⁵⁹⁻⁶¹. The Optical Stretcher, since its invention, is a well-established concept for mechanical phenotyping⁶². After a brief discussion of the working principle, the OS will be compared to the state-of-the-art, before experimental findings of utilising the OS to shine light on different biological questions are presented.

3.1 WORKING PRINCIPLE OF THE OPTICAL STRETCHER

As light is refracted through a trapped particle, forces arise on the surface, as described in Section 2.1. One force in particular is now of interest for cell stretching experiments. The trapping beam increases its momentum inside the cell as the cell has a higher refractive index than the surrounding medium. This momentum change has to be conserved and a net force on the cellular outline results in pulling on it instead of indenting it. Technically, every change in refractive index leads to a change of momentum. So even inside the cell at transitions between organelles and the cytoplasm forces arise. The distribution of forces can be calculated in a variety of ways, including ray optics²³, numerical modelling⁶³, or solving Maxwell's equations⁶³. In all cases, the distribution of forces is anisotropic, with larger forces acting along the optical axis as can be studied in Figure 3-1 c). This distribution of forces leads to the particle experiencing an outward pulling force along the optical axis. If this force is large enough, it is possible to deform the object. Thus, to study the mechanical properties of the trapped object, the magnitude of the forces is changed. Commonly this is done in a

stepwise manner (Figure 3–1b)) where the optical power, and thus stress, is instantaneously increased. Each measurement is divided into three phases; trapping phase (I), stretching phase (II) and relaxation phase (III). The trapping phase uses a low optical power to hold the cell stably in the middle of the optical trap. This is essential to allow the measurement of the un-deformed state of the cell, as the trapping power needs to be low enough to not pre-deform the cell, while large enough to easily trap and stably hold the cell against Brownian motion and gravity. After the trapping phase, the optical power is then increased at the start of the stretching phase, and the cell’s response is measured for its duration. This forms the main measurement phase. After a given time, the optical power is reduced back to the trapping level, and the cell is measured as it relaxes. The viscoelastic nature of the cell means that the relaxation back to the un-deformed state is a much longer process, and in the interests of measurement throughput, the entire relaxation is not measured. Taking a closer look at a cell, the predominant component that is connected to the membrane is the cytoskeleton, which in eukaryotic cells consists mainly of actin, microtubules and intermediate filament⁶⁴. To measure the deformation in an OS experiment, the outline of a cell is tracked as shown in Figure 3–1c). For a constant optical force above the trapping force, as in phase (II) of Figure 3–1b), the cell keeps deforming over time, which is drawn in red in Figure 3–1d). The deformation curve follows a non-linear behaviour as the forces acting on the cell change non-linearly together with the cells deformation and its fractional change in shape. The commonly used material model to describe deformations with this property is visco-elasticity⁶⁵. Under load, the material not only follows elastic extension, but also features an additional viscous flow component. As can be seen in Figure 3–1d), the stretching response of a cell in a DBLT under stepwise increased optical force often follows a power law $\varepsilon_{(t)} = \varepsilon_0 t^\beta + c$, where $\varepsilon_{(t)}$ measures the deformation of the cell along the long axis of a fitted ellipsoid at time t . ε_0 gives the initial deformability, β signifies the viscoelasticity and c is a fitting constant. However, depending on the composition of the cell, this relatively simple model doesn’t always hold. More complex models can be constructed which consist of elastic springs and viscous dashpots connected in series and/or parallel in various combinations.

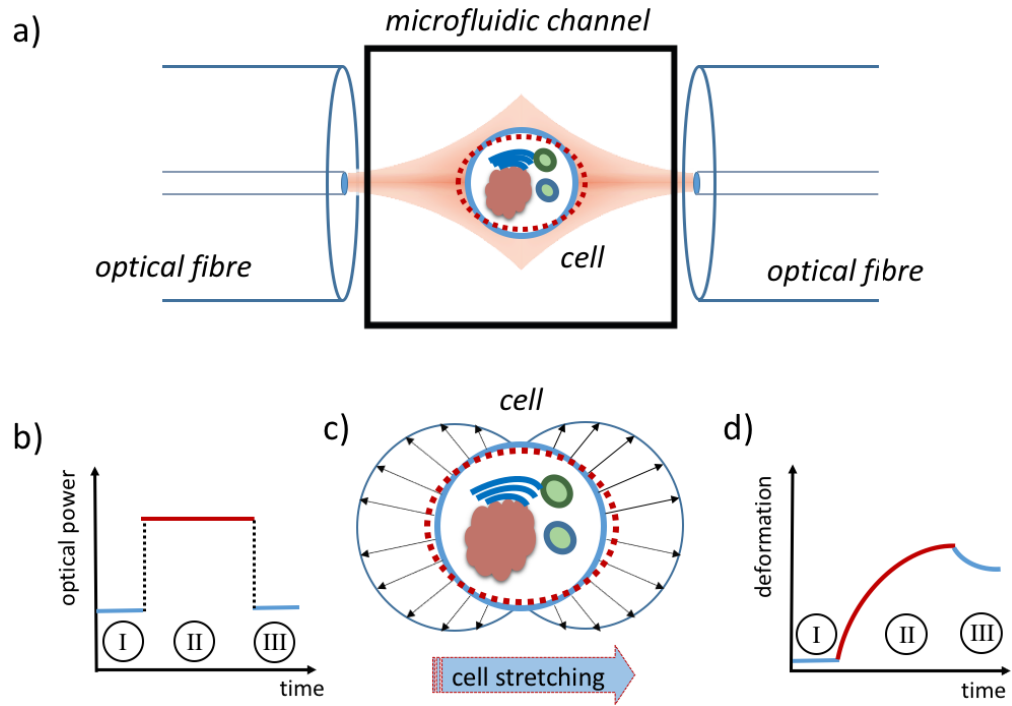


Figure 3-1: The concept of the Optical Stretcher (OS). a) A cell is trapped inside a DBLT. High enough optical power can deform the cell in form of stretching, as shown by the red dashed outline. b) The protocol of the OS consists of three phases: I) Trapping phase: The optical power is high enough to hold the cell in place yet not deforming the cell, II) Stretching phase: The optical power is increased in one step to a higher power that deforms the cell. III) Second trapping phase or relaxing phase: The cell slowly relaxes back into its initial state. c) As the schematic of the trapped cell shows, the surplus of optical power (II) results in optical forces acting on the surface of the cell that are big enough to stretch it. The length of the vectors is qualitatively proportional to the magnitude of the cell stretching forces, which are related to the gradient of the refractive index and the angle of incidence of the light. d) A typical deformation curve of a cell undergoing this stretching protocol. In phase I) the cell is practically un-stretched by the trapping power, then the optical power is increased significantly and a viscoelastic deformation is the response. In phase III) the lack of stretching power lets the cell relax into its initial state.

In this work, the results were best fitted using the Anti-Zener model⁶⁵: $\varepsilon(t) = \frac{1}{\eta_1} t + \frac{1}{E_1} \left(1 - e^{-\frac{E_2}{\eta_2} t}\right)$. In the Anti-Zener model E_1 and E_2 give a measure for the initial deformability with η_1 & η_2 measuring the viscous deformation. The process of relaxation after decreasing the laser power can also often be described with a power-law (or Anti-Zener model) with an opposite sign in the exponent. The total deformation of the stretching phase (II), but also its deformation curve can be used to gather insight into the mechanical properties. While the total deformation provides a marker for the cells deformability⁵⁹, from the slope the cells elasticity and viscosity can be derived⁶⁶. While the slope of the relaxing phase (III) can also reveal details about cellular mechanics, its information was not used in this piece of work.

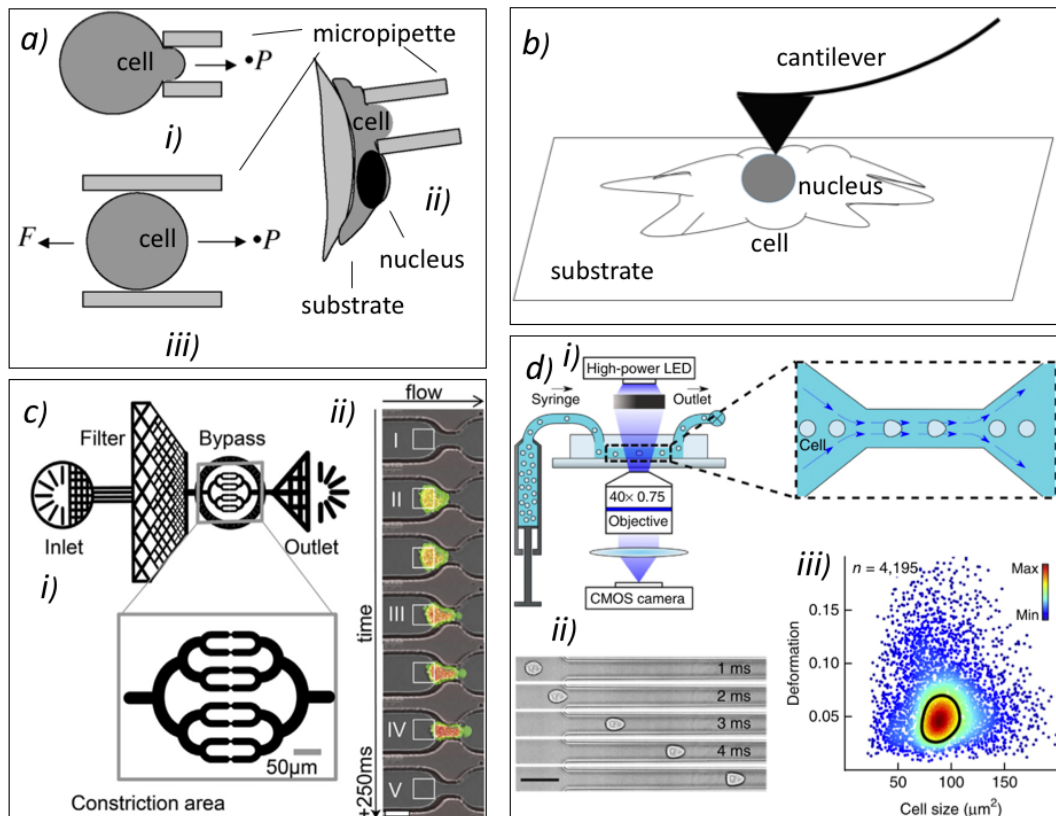


Figure 3–2: Different cell rheological measurement techniques: a) and b) show techniques of lower throughput, Micropipette Aspiration and Atomic Force Microscopy respectively. a) In Micropipette Aspiration a negative pressure is utilized to pull either a part of the cell into the pipette, as in i) & ii) or the whole cell, as in iii). Measuring the absorbed fraction of the cellular outline (for partial absorption) or the velocity of the cell moving into the pipette (for whole cell absorption) can be used as a marker for cell viscosity and deformability (schematic adapted from Hochmuth⁶⁷). b) By pressing onto a cell via a cantilever, using an Atomic Force Microscope, while measuring the cantilever's tip's position can not only reveal the height of the object but also stiffness. c) Microfluidic constrictions can be used to measure a cell's deformability. i) Cells are flushed into the device through the inlet, then filtered for debris, before they enter the microfluidic constrictions. The pressure in each of the 8 channels and thus constrictions is balanced, so 8 cells can be measured in parallel. ii) The measurement process of a cell passing through a microfluidic constriction shown in detail. Not only the whole cell but also the nucleus (orange) has to deform, before the cell can squeeze past the constriction. Adapted from Lange et al⁶⁸. d) Using a high-power LED when flushing cells through a tapered microfluidic channel, the throughput can be increased, as the necessary exposure for imaging can be decreased dramatically. ii) In the high shear flow surrounding the cell, the cellular outline becomes bullet shaped. The outline gives information about the deformability but is also dependent on the cell size as shown in iii). Relative to the channel dimensions, different cell size will lead to different deformation. Adapted from Otto et al.⁶⁹.

It should be mentioned, that for large deformations of objects, a non-reversible change in the object's structure can occur and the deformation becomes irreversible, a so called plastic deformation takes place. In a cell stretching experiment, this means that a significant part of the fibres of the cell's cytoskeleton have been stretched so far that they can not pull back all the way once the stretching forces are turned off. In other words, the fibres stay elongated further than they have been before the experiment. In alignment with the literature and their experimental findings, plastic deformation was avoided in the OS experiments presented in this Chapter.

The insight revealed by the OS into mechanical cellular properties²² will be discussed in detail in Section 3.4 after the relation of the OS to other techniques of cell rheology is explored in the following.

3.2 COMPARISON TO OTHER CELL RHEOLOGY TECHNIQUES

The mechanical properties of cells is a growing field of study, and a wide variety of techniques have been developed to investigate it. Some of the first studies carried out on the single-cell level used micro pipettes, which have been widely used for single-cell manipulation as they can enable precise manoeuvring of biological specimen, one example being in-vitro fertilisation⁷⁰, where both oocyte and sperm have to be manipulated accurately. Micropipette aspiration (review by Hochmuth⁶⁷) catches a part of the sample inside the tip of the pipette strong enough to immobilises the whole sample, so it can be manoeuvred and manipulated. Increasing the magnitude of the negative pressure inside the pipette leads to a larger fraction of the sample being aspirated into the pipette (see Figure 3–2 a). The length of sample drawn into a pipette of a given pipette diameter for a given pressure change, relates to the mechanical properties of the cell. By measuring the outline of the fraction of the sample being sucked into the pipette, the deformability of the cells can be calculated. As the applicable forces can be increased by several orders of magnitude (10pN – 10⁴nN)⁶⁷, a large range of cellular samples can be investigated. However the pipette is required to come into physical contact with the cell, which causes edge artefacts, allows adhesion between the cell and the measurement and can promote cross-contamination between samples. The nature of the experiment, hand picking individual cells, makes it a slow technique of low throughput (sample sizes of 5-30 can be found in literature^{71,72}) and it requires a highly trained person to carry out the experiment.

To get around this problem of throughput and expert users, a number of groups have developed microfluidic devices⁷³ which are capable of speeding this up as they enable fast sample handling conceptually comparable to mass manufacturing on a conveyer belt. Cells in suspension can be moved into the measurement area one after the other in laminar flow. Similar to micropipette aspiration, microfluidic constrictions^{68,74–76} can deform cells into a narrowed down geometry (see Figure 3–2 c) ii)). Cells can get pushed through tapered channels in fractions of seconds one after the other. Further, the microfluidic chip designs often allow for parallelisation. 8 channels were used simultaneously in the article “Microconstriction Arrays for High-Throughput Quantitative Measurements of Cell Mechanical Properties”⁶⁸ to increase the achievable

throughput up to 10^4 cells/h (shown in Figure 3–2 c i)). However, similarly to micropipettes, the walls of these constrictions can cause problems as they physically come into contact with the cell, potentially altering the result due to friction or adhesion, which may lead to clogging of the device. To get around this problem, hydrodynamic cytometry uses fast flowing liquids to provide a “liquid wall” which causes the cells to deform without physical contact to the device wall. One such system is shown in Figure 3–2d), the real-time deformability cytometer. With this device, Otto et al.⁶⁹ present a throughput of approx. 100 cells/s, while only using one microfluidic channel. The cells squeezing through the tapered channel adopt a bullet like shape dependent on their deformability (see Figure 3–2d ii)). The deformation is related to the geometry of the channel and the cell size, as shown in Figure 3–2d iii). The image analysis is executed on a high powered computer and can be realised fast enough to enable real-time analysis of the measurement data.

Compared to the above presented measurement techniques that all involve either pressure or flow of liquid, the surface microscopy technique of Atomic Force Microscopy (AFM) is of purely mechanical nature (see Figure 3–2 b)). It uses a flexible cantilever to indent the cells in direct physical contact⁷⁷. The cantilever is coupled into a laser system to allow the small changes in cantilever position to be measured. Tracking the deflection of the cantilever, together with the mechanical behaviour of the cantilever, allows the force acting on the tip to be calculated. In order to probe the samples topology or elasticity the cantilever is steered using piezo-electric elements and the surface is sampled by moving the tip vertically downwards. As the elasticity of the cantilever and the amount the piezo-element should have moved the tip down are known, the stiffness of the sample can be calculated. The actual position of the tip compared to the position it would have moving the tip down in air, differs only due to the resistance of the cell and the elasticity of the cantilever. Using an AFM for measuring the cell’s deformability, is generally speaking a low throughput technique (low tens of cell measurements^{78,79}). Further, the cantilever’s tip only probes a small area of the cells. This might be problematic, when for example, as indicated in Figure 3–2 b), the AFM tip might be pushing down on an area of the cell just above the nucleus, the nucleus responds stiffer than the cytoplasm and the measurement appears to display a higher stiffness as well. A different measurement, probing an area of the cell with mainly cytoplasm underneath, will provide a different response for the same cell, making cellular-level conclusions difficult.

There are also a wide range of techniques which involve attachment of foreign objects to the cell, or attaching the cell to a probing device. For a detailed review see Rodriguez et al.⁸⁰. For example, cells can be tagged with coated (commonly fibronectin) magnetic or di-electric beads. When applying a strong magnetic field, using a needle surrounded by an electro-magnet, also known as magnetic tweezer (see Kollmannsberger et al.⁸¹ for a comprehensive review), on a magnetic bead that is attached to the cellular surface, the cell will deform, following the magnetic pull. The displacement of the magnetic bead is linked to the cellular stiffness and the magnetic force applied. Similar in concept, the dielectric bead makes it possible to measure the cellular deformability using an optical tweezer^{82,83}, in order to displace either one (or two) bead(s). By attaching the cell to cantilevers, also called micro-plates⁸⁴, exerting strain directly are further options in order to deform a cell. Yet, the cell treatment with extraneous material is highly dependent on the strength and geometry of the bond of the attached material.

Non-invasive techniques like the Optical Stretcher are more elegant, as they are less invasive, probe the cell more as a whole, as the area of the cell experiencing force is bigger, provide similar measurement conditions for each cell, when compared to a bonding dependence in contact based methods, and the cell preparation is more straight forward, as compared to preparing the cells with beads/ attaching them to extraneous material.

Below the results of probing different cell types using the Optical Stretcher in the laboratory of Heriot-Watt University are presented, after laying out the experimental methods.

3.3 METHODS

3.3.1 Optical Stretcher fabrication and operation

The OS used in the experiments above has been constructed similar to Lincoln³⁷. In order to create a DBLT, a microfluidic chip in form of a square capillary (ID = 80 μ m, OD = 160 μ m; CM Scientific) was placed perpendicular between two coaxially aligned single mode laser fibres (HI-1060, Thorlabs). Fibre grooves and a guide for the microfluidic channel, casted in SU8 (SU8-2025, MicroChem Inc) using photolithography, provided a convenient geometry for the alignment,. The laser in use connected via a 50:50 splitter (Gould Photonics) to the two single mode fibres, was a 1070nm diode laser (YLM-1070-5LP, IPG Photonics). For a tight seal between the

microfluidic channel and the tubing on each side, necessary for sample loading and flow induction, the capillaries ends were attached to PEEK tubing and microfluidic unions (Upchurch Scientific). The tubing was then connected to centrifuge vials containing medium for hydrostatic pressure adjustment. Flow in the microfluidic channel can thus be induced by elevating one of the vials. Sample loading was provided via a syringe connected to a t-valve. As the suspended cells are loaded via a syringe it is important that no air bubbles are inserted into the device. Air bubbles can store pressure and the level of flow control suffers. The stretching process was controlled using a labview program driving the laser power via a data acquisition device (DAQ) (National Instruments). The details of the stretching sequence can be found in Section 3.1. The cell stretching is captured via an inverted microscope (Motic AE31) equipped with a 40x/0.75NA objective (Olympus), recorded using phase contrast imaging and a charged-couple device camera (CCD)(AVT Mako) and saved as video (30fps) in the AVI format. The nuclear stretching was performed in epi-fluorescence using a mercury lamp for illumination and a DAPI filter cube (Motic). The analysis of the videos takes place under the assistance of a labview program that tracks the outline of the cell via an edge detection algorithm.

3.3.2 Cell culture and treatment

The stem cell derived red blood cells were kindly provided on each experimental day by Dr Melanie Jiminez, while the brain tumour U87-MG cells were kindly provided by Dr Helen Wise and Dr Miguel Hermida. All other cells were cultivated after shipment at a CO_2 level of 5%, 95% relative humidity and a temperature of 37°C in house. Both the adherent cell lines HEK-293 (immortalised human embryonic kidney) and MAF (mouse adult fibroblasts) cells were cultured as follows: The culture medium consisted of Dulbecco's Modified Eagle Medium (DMEM), containing an added content of 10% foetal bovine serum (FBS), 4mM L-glutamine and 1% Pen-Strep, passaging the cells at around 75% confluency, in the exponential growth phase, Phosphate-Buffered Saline (PBS) was used to wash the cells before using Trypsin to detach the cells from the culture flask (2ml for 75cm² falcon flasks). After 2min of incubation and detachment the Trypsin is neutralised using 5ml DMEM and washed out via centrifugation. For the Adenosine Dialdehyde (AdOx) treatment of the HEK-293 FUS WT cells, necessary in Section 3.4.3, AdOx is added to the cell medium for 24h in a working concentration of 20µM. In Section 3.4.4 the stretched nucleus of MAF cells is measured in fluorescent mode. The nuclei were stained using a concentration 16 µM of Hoechst® 33342

(Fisher Scientific) prepared by adding 1 μ l of stock solution (16.23mM) per 1ml of cell containing solution. The dye was incubated for 5 mins and washed out before the experiment started.

Adherent cells were prepared for stretching by trypsinization as described above for passaging, and then re-suspension at a concentration of 1 million cells per ml in DMEM.

3.3.3 Data analysis

In the post processing of the captured stretches for each captured video frame the cellular outline was tracked via a custom built edge detection labview program. The majority of cells are spherical in shape during trapping and then are deformed in the OS, increasing their ellipticity, thus an ellipsoid was fitted to the edge of the cell. The change of the value of the long axis of the ellipsoid was the prime measure considered in the OS based rheology. The long axis value was averaged for the duration of the trapping time, and then the axis length was normalised to this value and expressed as a percentage deformation. The data from each stretch was resampled into a regular timescale and the values for each timepoint averaged to provide the mean deformation and standard error.

Average deformation curves are fitted to a range of mechanical models by least squared fitting, and the residual used to identify the best fitting model with the least free parameters. The models used are a power law, Zener and Anti-Zener model, linear liquid model and Burger's model⁶⁵. Statistical analysis was performed using two tailed, two-sample unequal variance Student's t-test.

3.4 FINDINGS REVEALED BY THE OPTICAL STRETCHER

As discussed above the OS is a potent tool to investigate how the mechanical properties of cells can change, and gives answers to questions in cell biology with possible fruitful results. Furthermore, as the goal of this thesis is to engineer a DBLT capable of accurate cell orientation, the time spend on using the OS is invested well in order to gain expertise in the field of dual beam laser trapping in general. Therefore, the following cell stretching experiments were carried out and cell types that were investigated were the immortalised human cancer cell lines HEK-293, U87MG, erythrocytes produced from stem cells and mouse adult fibroblasts. The general

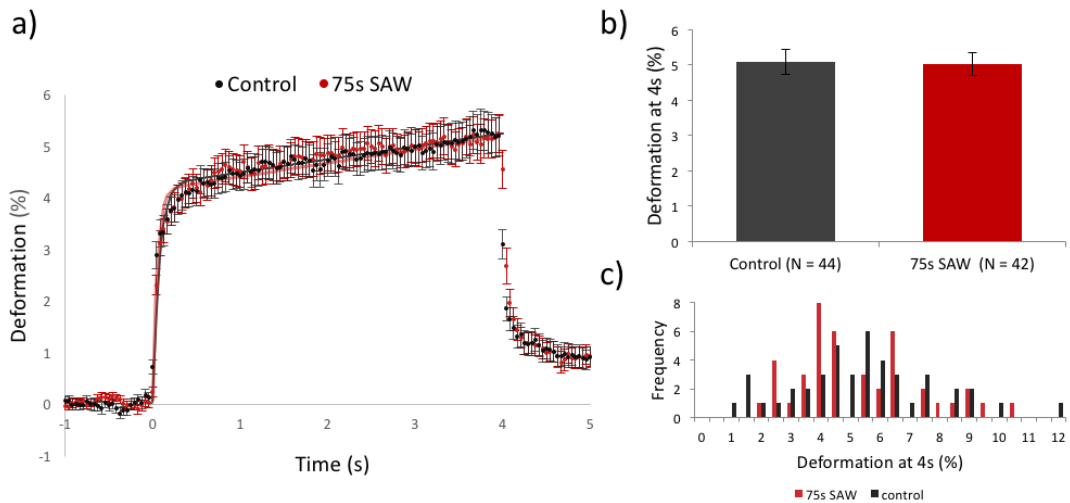


Figure 3–3: Deformability measurements on erythrocytes treated with SAW-waves vs. the control group, using the OS: The control group in black and the 75s SAW treated cells in light grey. a) The averaged stretching curves of the two populations lie clearly in between the standard error of the individual data points of the other population. b) Bar plot of the two measured groups. The standard error is displayed. A students t-test reveals a p-value of 0.89, thus no statistical significance. c) The deformation histogram for the two populations does not indicate an overall difference between the two populations.

stretching protocol was 2/4/4s; 2 seconds of cell-trapping, 4 seconds of cell-stretching and 4 seconds of cell-relaxation. As Erythrocytes are by far the most deformable the stretching laser power was set lower (1.1W compared to 2.6W for the other cell types).

3.4.1 Erythrocytes treated with surface acoustic waves are mechanically un-affected

The group around Dr Helen Bridle and Dr Melanie Jimenez worked on the production of erythrocytes from stem cells. In the process of sample sorting, a treatment with surface acoustic waves (SAW) to de-clot the blood was applied in a microfluidic setup. To answer the question whether the mechanical impact of the surface acoustic waves alters the red blood cells (RBCs) mechanically, comparative OS measurements were carried out.

RBCs historically, have been used rather frequently in initial experiments in microfluidic devices such as the OS. The cells used in this experiment were derived from stem cells in tissue culture. RBCs lack a nucleus and provide a simplified cytoskeleton compared to other mammalian cell types and are significantly more deformable. In order to probe the deformation of the cells, the total applied laser power was increased from the trapping power of 0.15W to 1.1.

Figure 3–3 reveals the findings: 57 RBCs that have been exposed to SAW for 75s were compared to a control group of 53 RBCs. Figure 3–3a), the control group in black follows closely the same deformation curve like the SAW treated cell population in

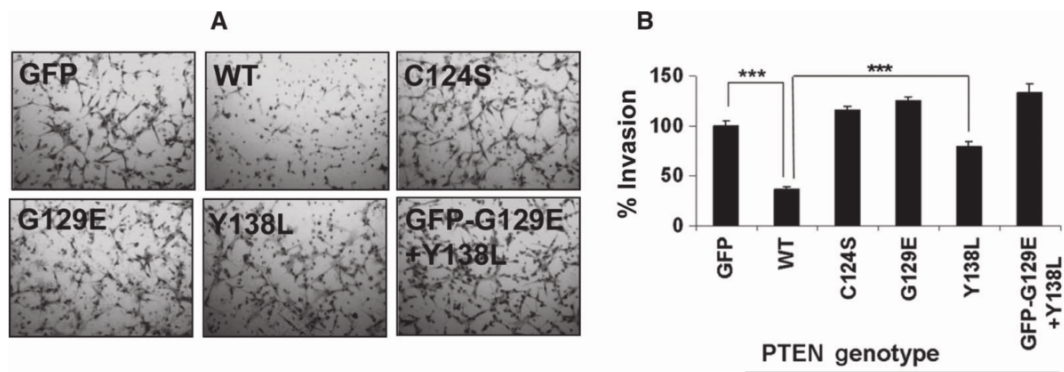


Figure 3-4: PTEN inhibits the cell invasion in surrounding tissue. But only if both lipid and protein phosphatase activity are present as demonstrated by the two PTEN mutants G129 and Y138L that are only capable of either lipid phosphatase or protein phosphatase. The significantly different invasion into a matrix gel can be inspected in (A) with the examined data presented in (B). Adapted from Tibarewal et al.⁸⁵.

grey. This can be viewed in more detail in the figures b) and c). The averages of the individual deformations of all the cells at 3.9s lied well in the same margin. The control group had an average deformation at 3.9s of $5.1\% \pm 0.36\%$ and the SAW exposed cells of $5.0\% \pm 0.33\%$. RBCs differ from most other cell types, for example their shape is biconcave shape and they do not contain a nucleus. Their stretch response is also more instantaneous compared to other cell types and can be fitted well by a Anti-Zener model⁶⁵, with R^2 of 0.96 for the SAW treated cells and 0.94 for the control group. The two groups followed roughly the same distribution of individual cell deformation as shown in the histogram c). Overall the experiments showed confidently that the exposure to 75s of surface acoustic waves had no major impact on the cells deformability, as the students t-test's p-value further indicates ($p = 0.89$).

3.4.2 U87MG glioblastoma cells containing PTEN are stiffer

Cancer physiology is one of the big riddles of modern biology to be solved and provides fundamental implications for human life. At Heriot-Watt University, Dr Nicholas Leslie gathered a vast amount of knowledge on the ties of the gene PTEN (Phosphatase and tensin homolog) to cancer^{86,87}. The PTEN gene is a tumour suppressor, when its function is lost within a cell, the cell can become cancerous. To investigate cell mechanics related to the abundance of PTEN and a mutation of PTEN, immortalised U87MG glioblastoma cells (brain tumour) with transduced PTEN, a transduced PTEN mutant Y138L and a GFP transduced null control were probed using the OS. The PTEN Y138L mutant preserves its lipid phosphatase activity, but in contrast to the WT, the mutant is missing, protein phosphatase activity⁸⁵ and activity against several model substrates⁸⁸. Tibarewal et al.⁸⁵ showed that wild-type PTEN reduced the invasiveness of the tumour cells into a 3D Matrigel matrix, but the mutant Y138L or a different

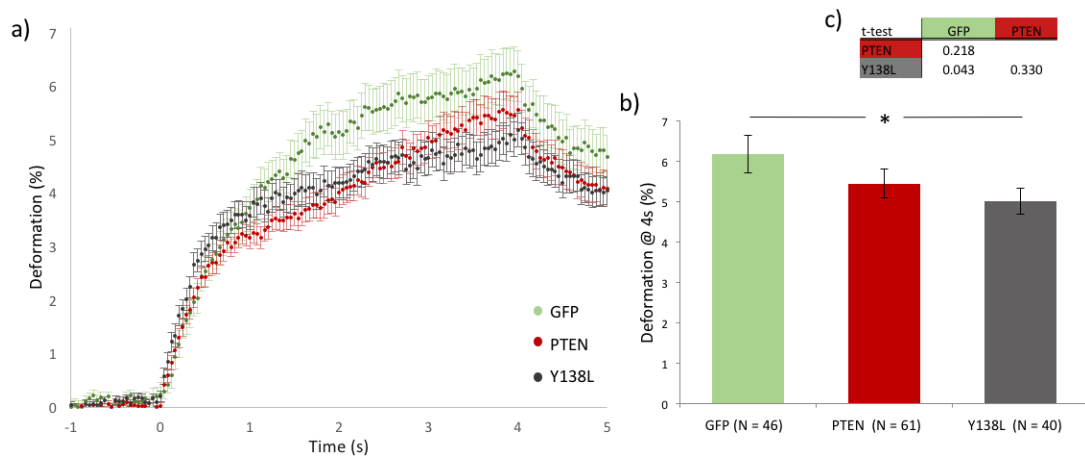


Figure 3–5: Three different types of U87 glioblastoma cells investigated in initial OS experiments: Shown in red are PTEN transduced cells, grey cells transduced with the PTEN mutant Y138L, and green marks the control group that had only GFP transduced. a) Measuring the three types of cells in the OS indicates a differing in stiffness. b) Shows the averaged deformations at 4s. The Y138L mutant cells are significantly stiffer than the GFP transduced control group ($p < 0.05$). c) Shows the related p-values of a student's t-test for the three cell populations.

PTEN mutant G129E, expressed separately or together, could not (see Figure 3–4).

Cancer cells are observed to be softer compared to healthy cells⁵⁹. Does a lack or mutation of the cancer suppressor gene PTEN already change the cellular stiffness? In order to investigate this question in the OS, the trapping power of 0.4W, was increased to 2.6W, stretching the specimen and probing mechanical differences of the different cell populations.

These cells are adherent and therefore will stick to the surface of the flask in which they are being cultured, however they must be floating freely in suspension to be measured in the optical stretcher. To achieve this, the cells were trypsinized, so they can be used in the microfluidic environment of the optical stretcher. Trypsinization is a common process in tissue culture, where in order to disassociate adherent cells from the culture flask and each other, a proteolytic enzyme is used to break down particular proteins connecting a cell to its surrounding. As this process is a normal part of adherent cell culture, it is not viewed as detrimental to the cells and after a short time period (~1 - 2h) the cells will re-adhere. The adherent nature of the cells means that they will not only adhere to the culture flask or the microfluidic channel of the OS, but they will also form clusters of cells within the culture medium. Since the OS measures one cell at a time these cell clusters can not be probed, thus the obtainable number of cells measured on a single day of experiments decreased compared to the RBC experiment of the Section above.

The initial results are presented in Figure 3–5. The GFP control marked in green displays the most deformation, followed by the PTEN transduced cells in red, and then the PTEN mutant Y138L in grey. Figure 3–5a) shows the averaged stretch curves of the three cell-populations in the OS experiments. In b) the averaged deformation at 4s of stretching is plotted for each population. The difference in deformability between the GFP control group and the Y138L mutant cells could be detected significant. This is indicated by ‘*’ denoting a p-value < 0.05 using a students t-test. The rest of the p-values comparing the cell types are given in c).

This shows that cells containing the PTEN Y138L mutant are stiffer than the non-PTEN containing control group. Yet, whether the non mutated protein PTEN is abundant in the cells or not should also show a significant impact, therefore isolated measurements between the PTEN transduced cells and the control group only containing GFP were carried out.

Pipetting the sample up and down with the nozzle firmly pressed to the bottom helped de-clustering before each sample loading and increased the throughput considerably.

The results presented in Figure 3–6 reveal the significantly different stiffness of the two cell populations. The deformation curves shown in a) can be well fitted with a power law of slightly differing viscoelasticity. In the bar plots of b) the high statistical significance of $p = 0.0016$ (students t-test) is indicated. Thus, cellular content of PTEN stiffens the whole cell against extension as revealed by the OS. Tibarewal et al.⁸⁵ showed that U87MG cells with PTEN were the least invasive into a matrix gel, while both the Y138L mutant and the GFP control showed a high level of invasion. Invasion of cancer cells into the tissue surrounding the tumour is often fatal, as metastasis can occur. Medical treatment of the consequently less localised cancer is very problematic. PTEN, besides other tumour suppressor properties, affects cellular invasiveness and the decreased cellular deformability, that was shown using the OS, plays a role in this picture.

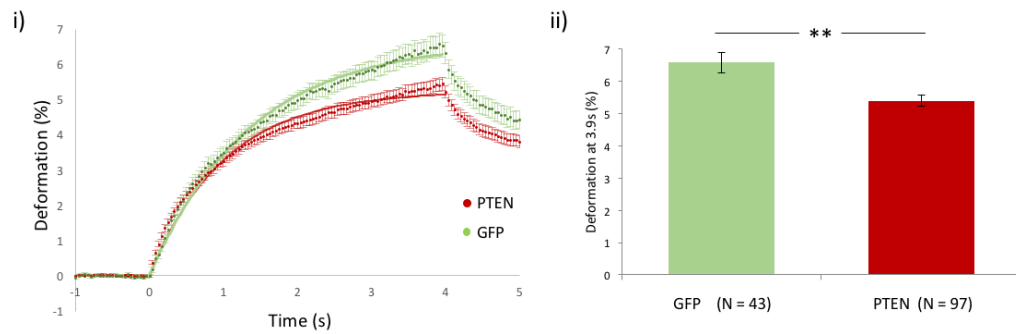


Figure 3–6: Comparing the U87MG PTEN transduced and the U87 GFP transduced control group showed statistical significance. PTEN changes the whole cell deformability and enhances the overall cell stiffness. a) the averaged deformations can be fitted using a Kevin-Voigt model. b) The average deformation of the two cell groups at 4s of stretching shows statistical significance with a p-value of 0.0016. ** denotes the significance of $p < 0.01$, t test.

Cells need to be of certain deformability to move through extracellular matrix (surrounding tissue). If a cell is unable to squeeze and pull through the pores of the surrounding matrix by elongation, the length of travel throughout the body is inhibited which should prevent metastasis^{59,60,89,90}.

The next logical step, to measure the Y138L mutant in higher detail next to the PTEN wild type, could not be carried out due to a tight project schedule. Considering deformability as a measure of invasiveness, the already visible cellular deformability difference between the GFP- and PTEN-transduced cells was logical and with a high enough number of repetitions statistical significance should be revealed.

The U87MG cells were not well suited to work with the optical stretcher. They are a highly adherent cell line which quickly adheres to surfaces to grow on. This narrows down the time window for measurements as cells and cellular debris stuck to the capillary walls quickly, and often in the trapping area. This is problematic for more than cleanliness, while dirt or debris between the stretched cell and the microscope's objective can make reliable tracking of the outline of the cell impossible, debris sticking to the capillary walls at the laser position can endanger the whole experimental device. The debris collects at this position naturally as it experiences the same gradient force as the specimen, therefore travelling into the trapping area. Debris that sticks to the capillary wall at the position where the laser light leaves the fibre, experiences a very high intensity of laser light which can cause it to burn onto the glass, creating a highly absorbing and scattering object in the trapping beam path. While small pieces of debris can often be removed by cleaning the system, for larger or burnt in debris, in order to prevent the laser light to be scattered and preserve the integrity of the optical trap, the two laser fibres of the DBLT would have to be moved. Further, a high amount of backscattered light is considered potentially harmful for the whole laser itself,

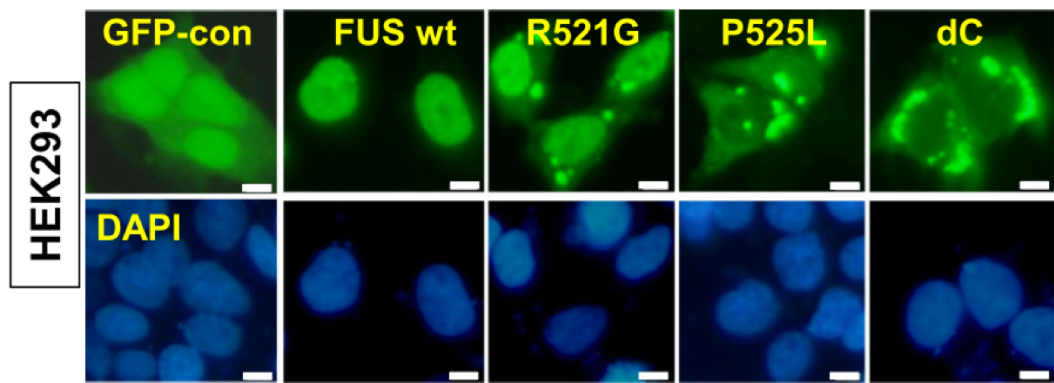


Figure 3–7: Mutations in the FUS gene can lead to cytoplasmic aggregates of FUS protein. HEK293 cells with different FUS- mutations and a GFP control are presented above. FUS wt, R521G, P525L and dC were GFP tagged to visualize the location of the FUS protein inside the cells, while the GFP control was transfected with GFP solely. Nuclear DNA was stained with DAPI (blue) to visualize the nuclei compared to the location of the FUS. From left to right: The GFP-control shows a monotone GFP distribution compared to the FUS wt where the GFP is only located inside the nuclei, while the other cell types show a clear accumulation of FUS outside of the nucleus. Scale bars are 5 μ m. Adapted from Fujii et al.⁹¹.

backscattered light can travel back into the laser’s cavity, causing it to overheat. Time consuming cleaning had to be performed and less experiments, compared to other cell types were carried out, when working with the glioblastoma cells. Often sodium dodecyl sulphate (SDS) showed to be the most effective surfactant to clean severe contaminations, solvent alone was not sufficient. In the following, experiments with the also adherent cell line HEK-293 are discussed. Despite their adherence they were less problematic and a higher cell count was achieved.

3.4.3 HEK-293 FUS mutant cells differ in their deformability from WT FUS

In another experiment with the optical stretcher, collaborators from the University of Cambridge were interested in how the expression of the fused in sarcoma protein (FUS) may alter cellular mechanics. Mutations in the fused sarcoma gene are related with the severe neurodegenerative diseases Amyotrophic Lateral Sclerosis (ALS) and Front Temporal Dementia (FTD)⁹². Malfunction of the gene in brain cells can lead to the death of motor neurons as in ALS.

In the FUS linked types of ALS, through mutation, accumulations of liquids and gels in the nucleus or cytoplasm are thought to lead to the loss in motor nerve function, which leads to a progressive weakening of the patient’s overall muscles and muscle control. As the deposition of liquids and gels through gene mutation leads to more accumulation of proteins in the cytoplasm (shown in Figure 3–7), it was expected that a change in the cell’s mechanical properties would be observed. To test this presumption, the immortalised human embryonic kidney cell line HEK-293 was shipped from the University of Cambridge in order to be tested on the OS setup at the Heriot-Watt

University. The following FUS-types⁹³ were then further cultured in-house for the examination: Wild-type full-length FUS, mutations FUS(P525L), FUS(R495X) and the FUS Null control group. The FUS protein in the FUS WT cells is predominantly located in the nucleus, both mutations R495X and P525L showed enhanced FUS aggregation in the cytosol^{93,94}. This differing allocation of the FUS protein between the diverse cell types possibly interferes with the mechanical properties of the cells, this will be explored in the following. The cells were stretched using the same protocol as for the U87MG cells, as explained in the previous Section and laser powers of 0.4W for cell-trapping and 2.6W for stretching, to probe the mechanical differences of the cell populations, were employed.

When inspecting the results, presented in Figure 3–8, the averaged stretch curve of the FUS WT cells, red in Figure 3–8 a), were the stiffest by a high margin compared to all other measured cell types. This is further shown in the sub-figures b) & d), where the averaged deformation at 4s of the FUS WT cells was significantly different. The rest of the measured cell types, the two mutants P525L, R495X, and the FUS Null GFP control showed no significant difference, concerning their deformability at 4s. The high number of measurements showed the significance of differing stiffness of the FUS WT compared to the other measured populations, but not in any other two cell types. Thus, it is questionable what the cytoplasmic aggregations, caused by the FUS mutation, actually do under stretching.

This is surprising as mostly the cytoskeleton is affected by the mutant's FUS accumulations and as the cytoskeleton is attached to the membrane, it is expected to be the predominant cellular component, stretched in OS experiments²². Yet, the FUS WT protein, located mainly in the nucleus, seemed to have the largest impact on cellular stiffness.

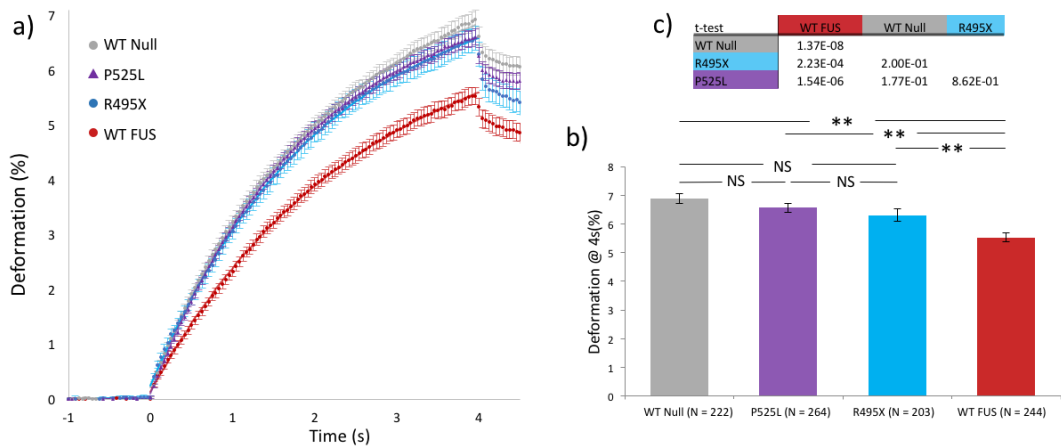


Figure 3–8: Four HEK-293 cell types with different contents of the FUS gene and FUS gene mutations measured in the OS. a) The averaged deformation curves of three rounds of same days of measurements on the different cell types. The in grey market WT FUS null cells are the most deformable, while the two FUS mutations P525L (purple triangles) and R495X (blue) are displaying approximately the same deformability. WT FUS in stark contrast shows to be far more resilient to the optical forces. b) As shown in the box plots of the various averaged deformations at 4s of stretching, the mechanical differences of the WT FUS cells are significant compared to the other cell types. ** signifies $p < 0.001$, in a students t-test. The individual p-values can be inspected up in c). The differences between the FUS mutations and cells without FUS were not significant.

The closely similar stiffness of the mutant cells compared to the Null control, suggests that the FUS accumulations of the two mutations is not connected to the cytoskeleton in a way affecting the cells ability to stretch crucially. On the other hand, intact WT FUS located in the nucleus increases the cellular stiffness. To test if the nuclei of the different cell types stretch in different manner, compared to each other and how it relates to the stretch of the whole cell, would be an interesting future experiment as clearly the nuclear stretch plays an important role, being the location in the WT cells with the abundance of the FUS protein.

Besides the bespoke FUS variations, Adenosine Dialdehyde (AdOx) treated HEK-293 FUS WT cells were investigated concerning their deformability. The AdOx treatment can lessen the FUS aggregation in the cytoplasm. As the accumulations are linked to loss in function of motor neurons causing ALS, to control the build-up is a promising approach in discovering treatment for FUS-linked ALS⁹¹. Therefore, testing the effects of AdOx on the cells stiffness is of interest.

When measuring 168 AdOx treated HEK-293 FUS WT cells compared with 169 cells of the untreated control group, the deformability is significantly increased. As shown in Figure 3–9 the average AdOx treated HEK-293 FUS WT cell at 4s of stretch is 13.4% more deformable with a statistical significance of $p = 0.011$ (students t-test). As the AdOx treatment reduces the accumulation of FUS in the nucleus and cytosol in FUS WT cells⁹⁵, a change in the overall stiffness of the AdOx treated cells was not unlikely.

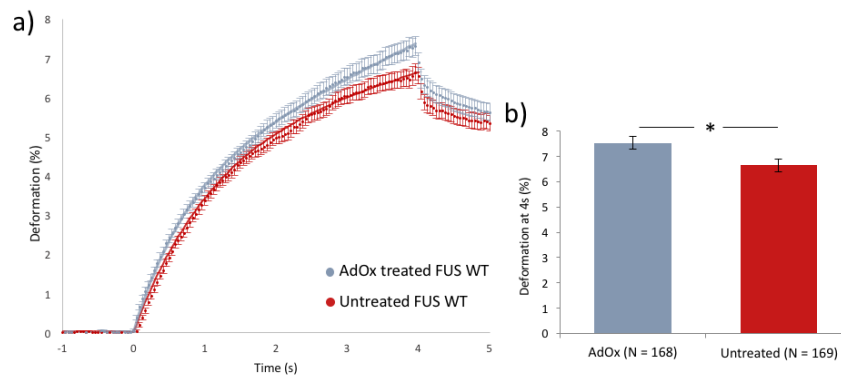


Figure 3-9: AdOx treated HEK293-FUS WT cells are investigated in an OS. AdOx treated cells (blue-grey) are significantly more deformable than the untreated counterpart (red). a) shows the averaged deformation curves while b) shows a bar plot of the average deformations at 4s of stretch. The p-value of 0.011 is statistically significant. '*' denotes $p < 0.05$ in a students t-test.

Yet, the cell mechanical changes induced by the AdOx treatment can have a different origin and need further investigation in future work.

3.4.4 Stiffening effect of *Lmna* on nuclear deformability

As could be seen in the previous Section, there is much more to cellular mechanics than the cytoskeleton. To probe this further, another protein of interest was investigated using the optical stretcher, namely Lamin A. Lamins are predominant components of the nuclear lamina, a structure surrounding and protecting the nucleus in form of a protein meshwork connected to the nuclear envelope. The nuclear lamina in mammals consists of mainly three types of lamins A, B, and C. The gene *Lmna* plays an important role as its isoforms generate Lamin A and C. Both are identified to be involved in nuclear mechanics⁹⁶. As Lamin A is involved in many severe diseases⁹⁷ it is investigated in the following via the OS.

More specific, *Lmna* deficient Mouse adult fibroblasts, denoted MAF *Lmna* $-/-$, were compared to *Lmna* WT cells which were inherent with the wild type *Lmna* gene. As the Lamins make up the majority of the nuclear lamina, the stiffness of the nucleus is suggested to differ the most in deformability related to different levels of Lamin A. Previous studies within the lab carried out by Thorsten Kolb, Julia Kraxner and Michael Haug, had shown the increased levels of Lamin A protein caused the cells to become less deformable, however to further probe this in more detail, the nuclear deformation within intact cells was measured. To carry this out, the nuclei were stained with Hoechst 33342, a fluorescent, live-cell DNA stain, and the experiment performed using fluorescence microscopy to capture the nuclear deformation. The cells were at first visualised using wide-field illumination, similar to previous experiments, in order to locate and trap the cells. Once the cell was stably trapped, the bright-field illumination

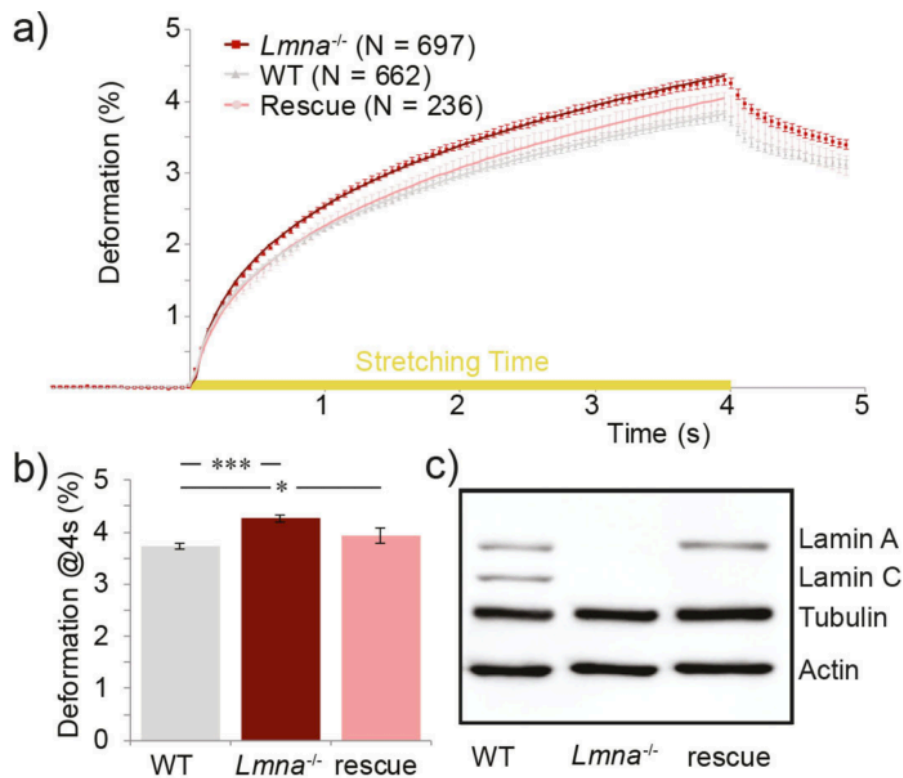


Figure 3–10: To investigate the effect of *Lmna* on cellular deformability three MAF cell types were compared: 1) a *Lmna* $-/-$ knockout cell line, lacking the gene, 2) a cell line that was lacking *Lmna* but got Lamin A transfected (rescue), 3) MAF wild type cells. a) shows the averaged stretch curves for the individual cell lines. The deformation at 4s of stretched is further plotted in b). As expected the WT cells are the stiffest followed by the rescue cells while the knockout cells were the most deformable. The differences in deformation compared to the WT cells were significant, indicated by ‘*’ and ‘***’ signifying $p < 0.05$ and $p < 0.001$ in a student’s t-test. For completion, the expression levels revealed by western plotting are shown in c). Figure adapted from Kolb et al.⁹⁸.

was turned off and the UV fluorescence light was turned on to excite the fluorescent stain, allowing the nucleus to be illuminated during the stretch. Under the total laser power of 2.6W the averaged nuclear stretch of the two cell groups revealed an evident difference in deformability.

As may be expected, the MAF *Lmna* $-/-$ nuclei were significantly softer as displayed in Figure 3–11. The stretch curves shown in a) follow a different trend. While the knockout cells follow a similar trend as in the previous OS experiments performed on whole cells, the MAF WT nuclei seem to plateau in their deformation once they reach a maximum. This points towards the nuclear envelope contributing highly to the firmness of the nucleus and therefore the stretch displays less of a viscous component, thus the stretch is rather elastic in deformation. Underlining this behaviour, the best fit of the *Lmna* $-/-$ and the WT nuclei were fundamentally different as shown in Figure 3–11a). The deformation of the MAF *Lmna* $-/-$ nuclei can be fitted using a power law similar to the whole cell deformation, while the WT stretch curve is better mapped using a Zener-model⁹⁹ (details about the fitting models can be found in the methods Section). Further in Fig. a) an example stretch of a WT nuclei at 4s is presented below the stretch curves.

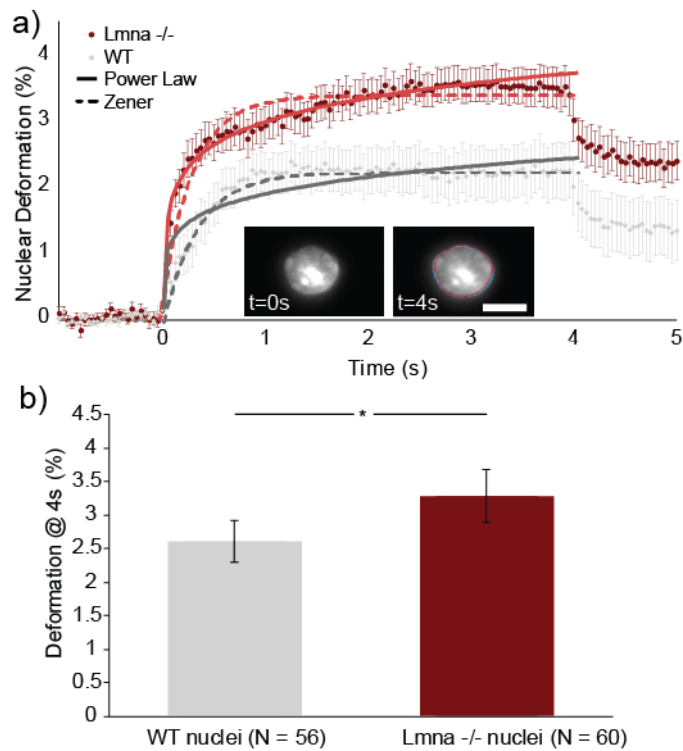


Figure 3–11: MAF *Lmna* knockout cells are compared to wild type cells in the OS. The deformation of the nucleus is measured via EPI fluorescence. Figure a) shows the mean deformation curves and an example nucleus being stretched. Different fit models match the two populations best. While the deformation curve of the knockout cells is best fitted using a power law, the deformation curve of the WT cells rather follows a Zener-model. b) the average deformation at 4s differs significantly for the two populations with the loss of the *lmna* gene, resulting in significantly more deformable nuclei. “*” indicates the statistical significance of $p < 0.05$ (students *t*-test). Adapted from Kolb et al.⁹⁸.

As the total stretch is around 2% the change is not easy to observe and therefore highlighted in blue comparing to the prior nuclear outline in red.

The averages of the nuclear stretches at 4s give a good measure of the absolute deformation. Comparing the knockout and wild-type mouse adult fibroblasts, a difference of deformability of statistical significance with a p -value < 0.05 (students *t*-test) was observed (shown in Figure 3–11b)). This data contributed to the publication “Optomechanical measurement of the role of lamins in whole cell deformability” by Kolb et al.⁹⁸. The publication showed the dependence of the whole cell deformability on the expression levels of *Lmna*. But as *Lmna* is mostly abundant around the nucleus, the measurements presented above, investigating the nuclear deformation in relation to *Lmna*, were providing important evidence.

3.5 DISCUSSION

Utilising the OS experimental challenges arise. It is absolutely crucial to not be biased to the outcome of the data when analysing the stretches of different cell populations. Some cell stretches will get filtered out of the average output, because of various

reasons such as the turning of the cell whilst stretching, too noisy data, cellular blebbing etc.. Thus, the filtering process needs to be equal for all data in order to stay absolutely neutral and scientific at all times not to shape the data subjectively. Blind experiments can be very helpful for this reason. Moreover, as cells are sensitive living objects, similar conditions have to be matched for all comparative measurements. A different buffer might change the electrolyte concentration, a delay in the cell harvesting could shift the measurements too far behind timewise to be objectively comparable to the previous data set.

Nonetheless, the different cell types investigated in the Sections above show the versatility of the Optical Stretcher. From enucleated erythrocytes in Section 3.4.1, the brain cancer cell line U87MG in Section 3.4.2, HEK-293 (kidney) in Section 3.4.3, towards the above discussed mouse adult fibroblasts in Section 3.4.4. While RBCs are easy to trap and stretch, the leukaemia cell line U87MG provided most of the problems in the experimental workflow as their severe adherence led to early cell re-clustering and clogging of the microfluidic device. Further, cellular debris stuck to the microfluidic channel walls. Deep cleaning was necessary after each use of the OS, leading to achieving high numbers of measurements becoming problematic.

The experiments of the FUS containing HEK-293 cells showed the power of the optical rheological device, the OS well. When the measurement-count reaches numbers significantly above one hundred, the averaged data becomes very meaningful. The number of measurements necessarily for a statistically significant scientific conclusion is also related to the variety in the cell population. Connecting back to other techniques, statistical significance is also where the OS out-performs the slow techniques of AFM and micropipette aspiration as achieving a high number of measurements can take several days. While providing a high level of accuracy the OS is fast enough to acquire statistically meaningful results. Compared to the latest developments in deformability cytometry with a throughput of the magnitude of 100cells/s⁶⁹, the numbers acquirable with the OS of roughly 100cells/h seem modest. However, the experimental character of the OS and the resulting time resolution can make up for it in a lot of use cases. An increase of the throughput of the OS by an order of magnitude would be ground breaking. After all, achieving both the statistical impact and high measurement detail, would result in the most powerful cell rheological measurement device overall. Approaches with automated pump systems have been tried in the past. Yet, they were often failing and manual control was often the method of choice. Nonetheless advances

in microfluidic technology could enhance the productivity of the OS. One prosperous technique for example is using surface acoustic waves¹⁰⁰ to position the cells inside the microfluidic channel. Standing waves in a microfluidic device hold specimen at the nodes of the wave. If possible to collect only one cell at each node, while later moving the standing wave through the microfluidic device to load cells quickly and reliably into the trapping area(s) of possibly multiple optical traps simultaneously, experimental throughput could be ramped up.

Section 3.4.4 revealed more capabilities of the OS. While in the previous Sections only whole cell mechanics were investigated, the OS can also be used to shine light on nuclear mechanics. In the case of the MAF cells this was realised by employing epifluorescence and analysing the nuclear stretch inside intact cells. Isolated nuclei, not only the nuclei inside whole cells, were also stretched previously¹⁰¹. Yet, imaging the deformation of nuclei inside the whole cell is closer to the setting nature provides, as the cell and nucleus are interconnected in life sample. Previous measurements in the lab of Dr Graeme Whyte showed the softening of the whole cells lacking *Lmna*, when probed with the OS, the fact that the protein surrounds the nucleus, suggested differing stiffness arising from the nucleus. Modifying the OS setup, in order to image the nucleus in fluorescence, this could be proven in Section 3.4.4. Taking this approach further, to correlate nuclear deformation directly to the deformation of the whole cell, by imaging both at the same time, could point out the findings in even better detail. How does the whole cell deformation correlate to the relative size, shape or orientation of the nucleus inside the cell? Inspired by the experiments on MAF nuclei this potential was explored in initial steps by first creating a stretcher setup imaging both the nucleus and the whole cell on different cameras and later engineering the setup, using an aperture to capture both the fluorescent and bright field image on the same CCD chip. Using this setup in future OS experiments, more insight in the role of the nucleus in whole cell mechanics will be gathered.

3.6 CONCLUSION

The big strength of the DBLT based rheological measurement device, named Optical Stretcher, lies in revealing differences in deformability of two, or more cell populations. The experiments probing the SAW treated red blood cells confirmed no difference between the examined groups, as expected. The experiments with the other cell types led to results of statistical significance. This underlies the relevance of the OS in single-cell rheology. In Section 3.4.2, it could be shown that the protein PTEN stiffens a cell

significantly compared to the control group of cells not containing any of the tumour suppressor gene. The PTEN presence in the cancerous glioblastoma cells increased cell stiffness, which can be a direct argument confirming one of the PTEN tumour suppressor qualities, as the increased cell stiffness of the tumour cells increases hindrance in migrating into surrounding tissue and potentially cast metastasis elsewhere in the body. Often in Cell-Biology, genetic mutation is linked to disease, thus testing what effect these mutations have on the overall cell properties is of high interest as this could lead to cell stiffness dependent diagnostic screening in a clinical environment, dependent on cellular properties and in this particular example, cellular stiffness.

Section 3.4.3 revealed that FUS WT cells compared to the FUS mutations R495X and P525L and the FUS Null control group are significantly less deformable. In the FUS WT cells, the FUS protein stays located in the nucleus, not forming accumulations in the cytoplasm. The likelihood of a provided higher nuclear integrity compared to the other groups is high. Utilising the drug AdOx in order to prevent FUS accumulations outside of the nucleus is a prosperous approach in drug development, testing treated cells, using the OS, an increased softness of the AdOx treated HEK-293 FUS WT cells was shown.

When tracking the nuclear outline instead of the cellular one, in Section 3.4.4, the OS was able to measure the nuclear deformation. Following the nuclear deformation revealed the relation of the abundance of the *Lmna* gene to whole cell and furthermore, nuclear stiffness. The *Lmna* gene, that is a major part of the nuclear envelope provides stability, as shown in the measurements of nuclei of cells lacking the gene they were significantly softer.

Besides the scientific findings and gathering of interesting data, the extended period of working with the OS was a valuable introduction to Dual Beam Laser Trapping. In the experiments it could already be observed how slight misalignment can cause gyration of trapped cells. Realignment of the trap was necessary at times. As building a DBLT is an integral part of this thesis the experience is well transferable and will be used in Chapter 5. But before the trapping of biological specimen is carried out, the machinery for controlled rotation of cellular samples in a DBLT has to be explored, understood and used reliably. The next Chapter focusses on the beam manipulation, using polarisation controlling techniques, building the core of a device to cast a beam shape that is capable of aligning the sample and rotating it stepwise.

4 HIGHER-ORDER MODE MANIPULATION FOR CELL ROTATION

The previous Chapter highlighted Dual Beam Laser Traps (DBLTs), operated as a cell stretching devices, in order to gather mechanical properties of the cellular specimen. DBLTs can also be modified to exert a torque on the sample which can overcome drag forces and cause the sample to rotate. As in the previous Chapter, biological samples are the samples of interest in this work. Rotating a biological sample can reveal a greater level of detail, as motivated in the introduction Chapter 1. Measuring the full 3D information of a biological sample faces the hindrance of the light having to pass through the whole object, which, for multicellular samples can drastically reduce the resolution. When the object is rotated tomographically, meaning perpendicular to the microscope's optical axis, the maximum distance is reduced to half the object and thus increases image quality and resolution. Interest in the topic of cell rotation is growing and different methods have been developed. Their usability and area of use differ from one another, which are reviewed in Section 5.1.1.

Cells provide a slight anisotropy in shape and refractive index profile. This is necessary in order to align the specimen under the use of a laser signal that is of non rotational symmetry which will be used in this thesis. A perfect sphere would not feel any restoring force to keep it in alignment with the trapping beam profile.

One approach to align and orientate cells is higher order mode sample rotation within a DBLT^{20,47} which has been shown to be capable of rotating individual cells, however pitfalls of the existing methods include the precise alignment requirements of using a Spatial Light Manipulator⁴⁷ and coupling the laser light from free space back into the fibre to achieve mode rotation, or the requirement to create a liquid-tight seal in the microfluidic trap as one of the laser beam arms had to be rotated macroscopically²⁰ (see Section 2.1.3). A method which can manipulate the higher order modes in-fibre, without macroscopic moving parts, would be preferred, henceforth this is the topic of this Chapter. To understand how the same higher order mode of a two lobe pattern can be utilised for an all-in-fibre mode rotation based cell rotation, in the following possible methods of manipulation of the LP_{11} mode are discussed.

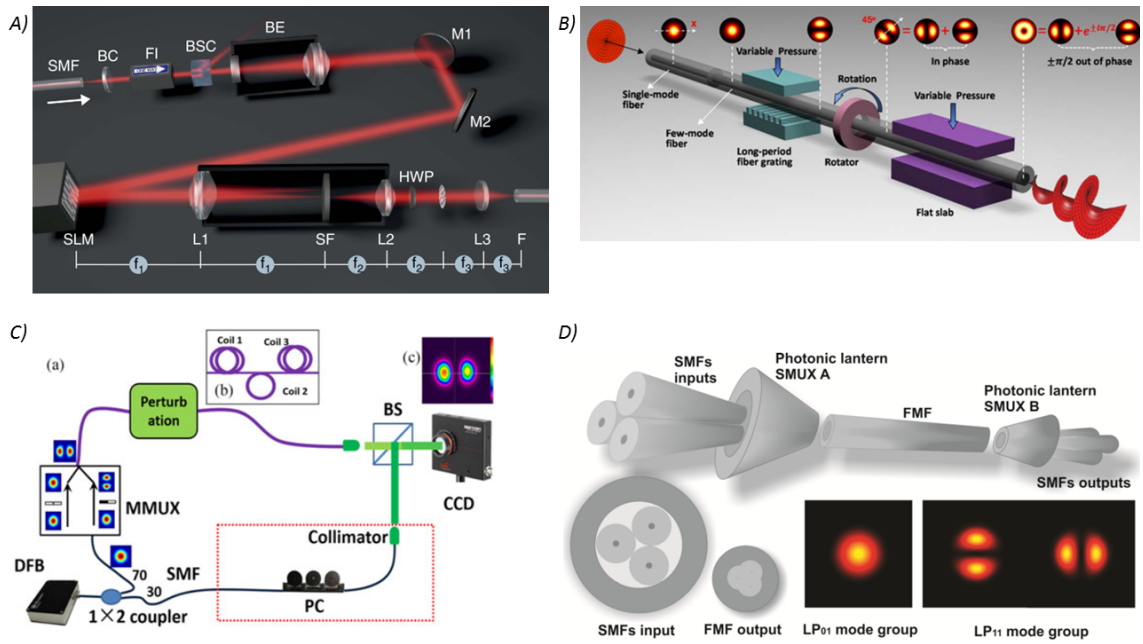


Figure 4–1: Different LP_{11} mode manipulating techniques. A) By reflecting the laser-light from a spatial light modulator (SLM) the beam profile can be shaped to a LP_{11} mode at different orientations. Figure taken from Kreysing *et al.*²¹. B) A mechanical long period fibre grating can cast LP_{11} modes in a DMF. Figure taken from Li *et al.*⁵⁷. C) Coiled DMF can act as a phase plate three fibre paddles are able to rotate an LP_{11} mode. Taken from Hong *et al.*¹⁰⁴. D) Mode coupling in a photonic lantern can create a LP_{11} mode. Taken from Leon-Saval *et al.*¹⁰⁵

4.1 OVERVIEW OF DIFFERENT LP_{11} MODE MANIPULATION TECHNIQUES

Most concepts of LP_{11} mode conversion and manipulation presented in the following rely on changing the refractive index profile of a part of the fibre by mechanical deformation. Ways to deform the fibre in order to create and manipulate LP_{11} modes, include the application of uniaxial stress perpendicular to the cylindrical fibre, leading to elliptical deformation¹⁰², bending the fibre¹⁰³ or periodic micro-bending⁵⁷. Exceptions where no mechanical modulation was used are the usage of a spatial light modulator (Section 4.1.3) and the photonic lantern (Section 4.1.4). A selection of LP_{11} mode manipulation techniques are discussed in the following Sections.

4.1.1 By fibre grating

As discussed in the background Section 2.3.1 periodic differing refractive index in fibre can create LP_{11} modes in a DMF. Li *et al.*⁵⁷ showed how to create rotated ring modes from LP_{11} modes by utilising a mechanical long period fibre Bragg (LPG) grating (blue in Figure 4–1 B)), a rotator and two pressure slabs (in purple). The LPG consisted of teeth of a certain period and a plate that can exert variable pressure from the top, causing elliptical core deformation to achieve the generation of LP_{11} modes out of the fundamental mode. Adding a rotator can orient the LP_{11} modes, while the two pressure slabs convert the LP_{11} mode back to ring modes. Li *et al.*⁵⁷ were able to create ring

shaped Eigen-modes out of two orthogonal, $\frac{\pi}{2}$ out of phase, LP_{11} modes. Not only a pressure based LPG can be used for the mode generation, for example Kim *et al.*¹⁰⁶ realised a LP_{01} to LP_{11} mode converter based on microbending, using standing acoustic waves along a part of the fibre, also Zhao *et al.*¹⁰⁷ showed how using an external CO_2 laser can be used instead of the mechanical LPG to create a long-period fibre Bragg Grating inside the fibre core. The CO_2 laser was spread through a grating to periodically heat the fibre. The induced heating caused the fibre to expand, altering the local refractive index and creating an LPG.

4.1.2 By fibre loop paddles

Three fibre coils mounted in line to each other while the individual mounts can be angled are commonly used as polarisation controllers for single mode fibres¹⁰⁸. After launching a fundamental mode into a liquid crystal on silicon-mode converter to create a LP_{11} mode, Hong *et al.*¹⁰⁴ showed that such a device can be made use of to orient LP_{11} modes over a range of 360° (setup shown in Figure 4–1 C). More specifically, by changing the orientation of the three 32mm wide fibre loop paddles relative to each other, the output orientation can be changed. The simplicity of using fibre loop paddles for the orientation of an LP_{11} mode is promising and is compared to all other presented methods the cheapest. However, it is not stated that the change in mode angle is monotonic nor if LP_{11} signal was present between the different LP_{11} orientations, thus a reliable capability of rotating cells is doubted, as the alignment of the cells in non LP_{11} modes can change the direction of the overall rotation. Further, it is to note that this work was published while the bespoke project of the higher order mode cell rotator based on piezo fibre squeezing was already advanced in cost, time and progress.

4.1.3 By Spatial Light Modulator

Kreysing *et al.*⁴⁷ spread an emanating laser beam from a SMF, using free space optics, to fill out the full range of a spatial light modulator (SLM) (shown in Figure 4–1-A)). By changing the phase profile of the Gaussian beam, reflecting from the SLM, higher order modes at different orientations could be created. The higher order modes were then coupled into a dual mode fibre (DMF), allowing for higher order mode propagation. Knowing the length of the DMF and the beat length of the mode, the beam profile present at the facet at the end of the DMF, could be calculated. While the beat length describes the periodic physical distance after a mode has the very same beam profile, as one period of the beat length before that. The SLM based cell rotator was

very alignment intensive and cost expensive, while a high level of accuracy of cell orientation was not shown in the publication.

4.1.4 By photonic lantern

The creation of a photonic lantern (for a comprehensive review Birks *et al.*¹⁰⁹) brings fibre cores of desired number close together, by heating and pulling a fibre bundle. Leon-Saval *et al.*¹⁰⁵ used a photonic lantern, consisting of three fibre cores close in proximity to couple their evanescent field into each other and achieving coupling into an effective LP_{11} mode, as shown in Figure 4–1 D). While the device was displaying high mode selectivity and low loss the concept of the photonic lantern bears a finite number of fibres feeding into it, in this case three, the achievable mode angles are hence limited. Nonetheless, Velázquez-Benítez *et al.*¹¹⁰ managed to orient polystyrene microparticles using this technique.

4.2 BY PIEZO FIBRE SQUEEZER BASED POLARISATION CONTROLLER (PCD)

The LP_{11} mode manipulation by a piezo fibre squeezer is researched in this thesis, yet there are fundamental elements in the literature that lead towards it. Schlosser⁵² motivates the effect of an elliptic deformation on the fibre core as altering the phase difference between the two possible linear polarisations of the fundamental mode (horizontal and perpendicular). Changing the phase between the two linear polarisations results inevitably in elliptical polarisation, possibly circular polarisation. This can be done by changing the fibre geometry since the refractive index profile is directly linked to it. Using stress in form of squeezing on a SMF can therefore control polarisation^{111,112} and has been implemented in the past using electromagnetic relays that control the state of polarisation through deforming the fibre elliptically, thus exert linear birefringence¹¹³. This method has been later replaced by piezoelectric ceramics¹¹⁴. The device used in this piece of work uses 4 piezoelectric ceramics in series acting as fibre squeezers. The first and the third are parallel, as are the second and forth, with the second pair of piezo-elements oriented at 45° to the first (see Figure 4–2). This ensures that no linearly polarised light will be an Eigen state of all four fibre squeezers, leading to at least one pair of the piezoelectric elements can alter the polarisation. The capability of achieving endless polarisation control¹¹³ in single mode operation in SMFs has been demonstrated and suggests a high level of capabilities, possibly also DMF operation, hence this motivates to investigate the device on modes

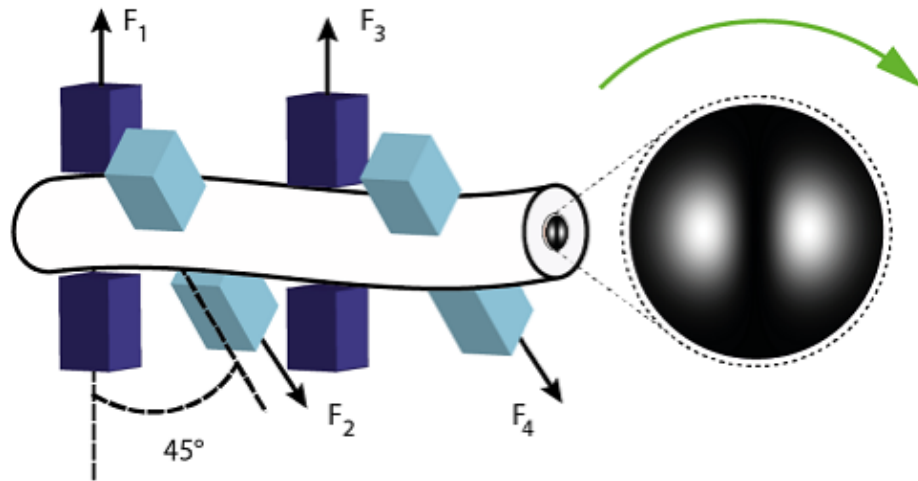


Figure 4–2: Working principle of the piezo fibre squeezer based mode manipulation. The 4 fibre squeezers are orientated 45° to each other to ensure endless polarisation control. Squeezing on the fibre changes the mode mixing of the Transverse Electrical/Magnetic- with the hybrid-eigenmodes that occurs in the DMF. The right stresses exerted by the PCD result in LP_{11} -modes at different orientations.

of more complex polarisation than linear and elliptical, like the three different ring modes TE_{01} , TM_{01} and HE_{21} , whilst operating the polarisation controller below the single mode cut-off wavelength. As motivated in Section 2.3.1 the dual lobe mode is dependent on the polarisation present in the ring shaped eigenmodes and their interference. Snyder⁴⁸ *et al.* even suggest that elliptical core deformation transforms ring modes directly into dual lobe modes as shown in Figure 2–12. If that would hold true it would be just necessary to squeeze a fibre hard enough and obtain a dual lobe mode out of a ring mode. Especially findings in Section 4.4.3, where for increased piezo fibre squeezing a periodicity in the received mode signal can be observed, are contradictory. Although the state of polarisation or the intensity pattern at position of the piezo-elements stays unknown, as the signal is collected after more fibre, so perturbation will have occurred. It is to note that for multimode fibre the concept of piezo fibre squeezing is used for mode scrambling¹¹⁵, a process used to improve beam quality by altering the mode content for uniform output, so the ability to affect more complex polarisation profiles has been tested before. Figure 4–2 shows the core idea of how piezo fibre squeezing is intended to be used for LP_{11} mode manipulation and in the Sections 4.4 the results of researching this idea will be discussed thoroughly.

4.3 METHODS

To give the reader the opportunity to familiarise with the experimental setup and methods before inspecting the results, the following Sections are placed here.

4.3.1 Experimental setup

As for the laser source, an IR 1070nm laser (YLM-1070-5LP, IPG Photonics) was employed. It was directly spliced onto a HI1060 SMF (Thorlabs) followed by a 75/25 fibre coupler (TW1064R3A2A, Thorlabs). This created the two beam arms to form a DBLT. The second beam arm, that kept trapping with the fundamental laser mode, was safely stored in a beam dump. In the other beam arm the fibre was spliced offset, similar to Kreysing *et al.*²⁰, from a single mode fibre (SMF) onto a dual mode fibre (DMF) (SMF28-J9, Thorlabs). The vertical offset measured approximately 4 μ m, a similar distance as the core radius of the DMF. This method increased the coupling of LP_{11} mode into the DMF whilst decreasing the propagation of the fundamental mode and meanwhile sacrificing around 60% of the optical power. This was the reason why a non 50/50 coupler was used to form two beam arms, as the high loss inducing splice needed to be compensated, enabling similar trapping power in both beam arms.

The DMF was then connected to the commercially available polarisation controller based on piezo fibre squeezing¹⁴ (PCD-M02; Polarite III - General Photonics, USA). The PCD was implemented in the experimental setup as shown in Figure 4–3. The fibres were coiled and fixed in place to ensure the stability of the input polarisation. Bending and twisting the fibre alters the state of polarisation in a DMF due to induced birefringence. For the first rounds of characterizations the polarization controller was connected using FC/APC connectors (upper right hand corner of the blackout box Figure 4–3) later these connectors were replaced by direct splices, so operation in high power for the trapping could be assured. For alignment purposes the fibre is collimated and reflected by 3 mirrors. After passing a focusing lens and an IR-filter the signal was imaged by a CCD camera (Basler, Germany). Some parts of the setup were kept outside of the blackout box: The laser and laser controller, the coiled fibres, the PCD power supply and the Arduino microcontroller, which drives the polarisation controller (see Figure 4–4). To drive the Arduino output and thus the PCD input, while collecting the data of the CCD-camera, a Labview program (National Instruments) was written, which was executed manually to start an experiment.

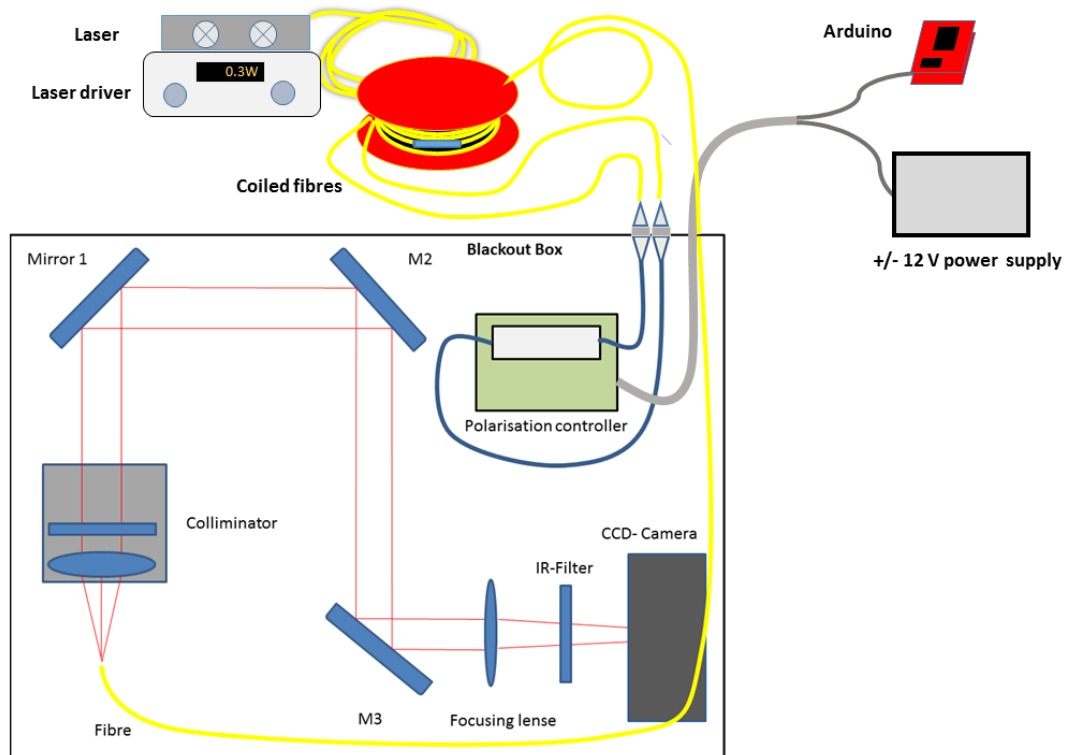


Figure 4–3: Schematic of the setup for mode calibration. In the top left corner of the schematic the laser and laser driver are drawn. The laser output was spliced directly onto a HI-1060 optical fibre which is then split using a 50/50 splitter. The beam arm used for the mode manipulation was further spliced on the SMF 28 J9 optical fibre (red cylinder fibre reel) and the higher order mode guiding fibre was coupled in and out the polarisation controller over two connectors. The output-fibre was coiled around the reel and inserted through a small slit into the blackout box (top right corner of the box). The signal was first collimated (bottom right corner) so that the beam could be aligned precisely by three mirrors, after that it was down-focused and weakened by an IR-Filter to be characterized with a CCD- Camera. On the top right corner are schematics of the Arduino providing the input voltages driving the PCD and the power-supply.

In order to find dual lobe mode examples at various angles, the four output voltages of the Arduino, operating the four piezo fibre squeezers, were increased in linear ramps (see Figure 4–9). As the PCDs’ analogue input can range from 0 to 5V and is amplified 28 times, this results in 0 to 140V. This voltage was applied on the piezo elements, extending them by the piezo electric effect and thus squeezing the fibre in between them. Obtained imaging data was stored in the AVI format and characterisation data as .xls-files. In the following Sections different methods are described to quantify and qualify the characteristics of the modes present during manipulation with the PCD.

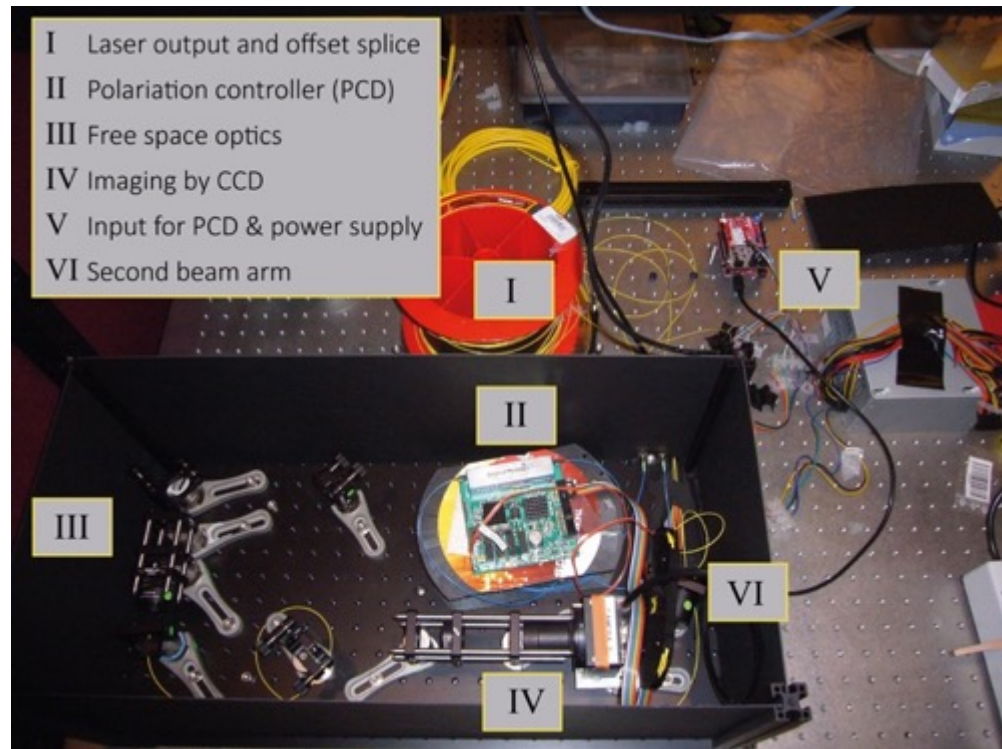


Figure 4-4: Experimental setup for mode manipulation and characterization. The SMF fibre was split via a fibre optic coupler, to form two beam arms for dual beam optical trapping. The excess fibre was coiled [I] and one of the beam arms was spliced offset onto the DMF. [II] For laser safety, the fibre ends were kept in a blackout box that also inhibited the PCD. The higher order mode beam leaving the DMF was collimated, guided via mirrors [III] and down focussed via a lens into a CCD camera [IV]. The 12V power source of the PCD and the Arduino driving the voltage ramps, were placed outside the box [V]. [VI] the 2nd beam arm to form a dual beam laser trap was pointed at a beam dump inside the blackout box.

4.3.2 Characterising the mode signal

The trapping signal has to be close to a pure LP_{11} mode to trap and manipulate cells in the desired fashion, as otherwise the cell(s) might align uncontrollably. To evaluate the mode's quality a circular Region of Interest (ROI) was centred on the optical axis, with a radius that passes through the intensity maxima and minima of the LP_{11} mode. See Figure 4-5 for examples. The intensity values along this ring shaped ROI, together with the centre pixel value I_{centre} , were extracted for quality characterisation and mode angle calculation.

4.3.2.1 Quality value

From the ROI intensity data, a mode quality value Q could be generated in the following way:

The number of maxima and minima along the ring profile (referred to as peaks and valleys) had to each equal 2 for the LP_{11} mode. If it differed Q is set 0 by default. Peaks and valleys were thresholded against the mean of the intensity along an extended ROI (a

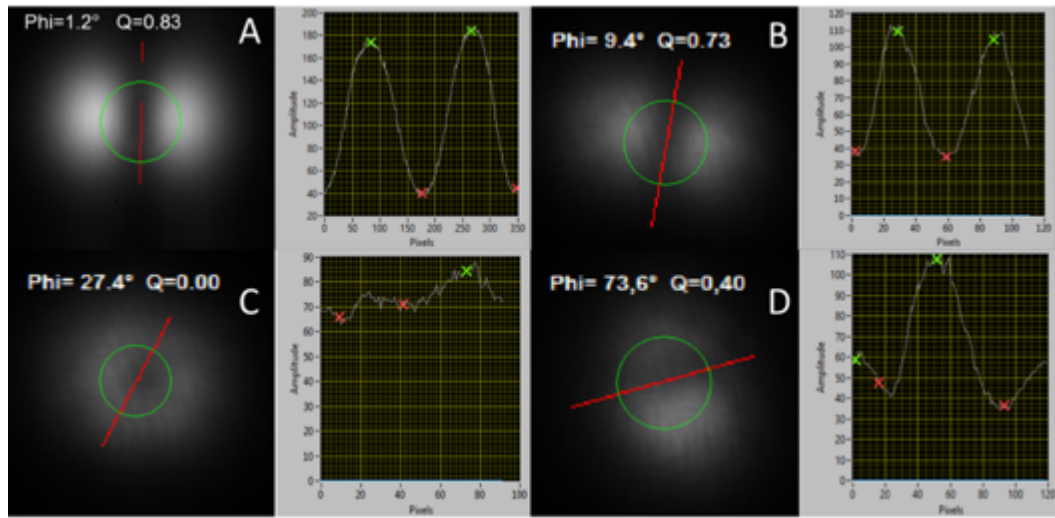


Figure 4-5: Four examples of LP_{11} modes and their characterisation. To characterize the quality and also measure the angle a circular region of interest (ROI) is inserted (green circle). The intensity profile along the ROI to calculate the signals quality Q is shown on the right. $I_{V<}, I_{P<}, I_{V>}, I_{P>}$ the intensity values of the valleys and peaks are indicated by red and green crosses right hand side. For example, in **A** the quality value measures $Q=0.83$ (range is 0 to 1) since it comes very close to an ideal mode. Example **A** was a mode captured not from the current experimental setup. Bare fibre was pointed directly into the camera. Example **B** a reasonable good quality mode ($Q=0.73$) obtained in a large scan through different combinations of applied voltages. This is the kind of mode the filter should be good for Example **C** and Example **D** are two bad modes captured in the same scan, while **C** is quite close to a fundamental doughnut mode (TE_{01}, TM_{01} or HE_{21}) the assigned quality is 0 due to lack of two peaks, **D** is just of poor symmetry and has a quality of 0.4.

third was added to the end of the ROI to not neglect an extreme value on the edge at $0^\circ/360^\circ$).

Further, the signal was ideally symmetrical and of high contrast. The line of minimum shall approximately be of constant value and the average minima shall not be far of the background. These considerations were summarised in the parameter:

$$Q = \frac{1}{5} \left(\frac{I_{V<}}{I_{V>}} + \frac{I_{P<}}{I_{P>}} + \frac{(I_{V>} + I_{V<})/2}{I_{centre}} + \frac{I_{bgrd}}{(I_{V>} + I_{V<})/2} + \frac{I_{P>} - I_{V>}}{I_{P>} - I_{bgrd}} \right)$$

The mode quality value Q ranged from **0** to **1**, while **1** indicated an ideal LP_{11} mode and **0** non dual lobe character. All the contributing ratios were in between **0** and **1** as well, therefore the whole sum was normalised by division through **5**. The first two terms considered that both peaks and valleys were symmetric for an ideal mode, when peaks or valleys were equal in intensity their ratio became **1**. To provide a number of **1** or below, the smaller peak ($I_{P<}$) was divided by the higher one ($I_{P>}$) and a similar procedure was applied for the valleys. The average intensity of the valleys further shall not differ much from the centre's and the background, as a measure of signal to noise. The fifth fraction subtracted the background of the high intensity peak and compared it to the peak minus valley. Which for ideal background and minima gave 1. Example modes can be inspected in Figure 4-5

Example A was captured by pointing bare fibre into the camera and of high quality ($Q=0.83$) therefore had the best signal to noise ratio, but also a high symmetry in minima and peaks. This mode would be ideal for specimen alignment. Example B has a reasonable quality of $Q=0.73$, the signal is fairly symmetrical, but as the signal got more distortion the minima differs more from the background than in A). Yet, it is sufficient for trapping and aligning cellular specimen, this kind of signal will be observed often in the calibration process of the PCD. C and D show poor mode quality. While in C a ring mode can be inspected (only one peak $\rightarrow Q=0$), the signal of D is of poor symmetry, leading to a low Q value of 0.4.

For the effective filtering of desired and undesired modes a quality threshold that depended on the imaging quality, the selection of the ROI and of course the mode quality. For experiments where each piezo fibre squeezer was driven 10 times, yielding in $10 \times 10 \times 10 \times 10 = 10,000$ frames, a Q threshold of 0.5 led to around 3,500 patterns to be considered a dual lobe mode.

4.3.2.2 Mode angle

Two different measures of the mode angle were of consideration, namely the two axis of symmetry of the two lobe mode. The first axis is a straight line from peak to peak, the second the mirror axis in between them, forming the line of zero intensity. In the following the latter was used. Taking the previously discussed circular ROI into account, the line of zero intensity will mark two valleys, as shown in Figure 4–5, indicated by red crosses. Using trigonometric relations and valley detection, the line-information of the ROI and the position of the valleys can be back translated into a polar angle.

4.3.3 Mode selection

The LP_{11} modes of interest are of high quality and need to be selected angles in ascending order to ensure a monotoneous sample rotation. For this selection the results had to be filtered and ordered. The results were stored in AVI format and additional .xls sheets. Each row of the .xls-sheet contained data in the following order: frame number, the four voltages, mode angle, mode quality, the line profile of the ROI. To find the best modes for each angle a labview program was built. This program sorted the rows, eliminating the line profile, first by angle and then quality. In this program, the user can then click through the mode examples for each desired angle and make a selection and save this into another .xls-file. Additionally, the piezo elements were set to 0V between

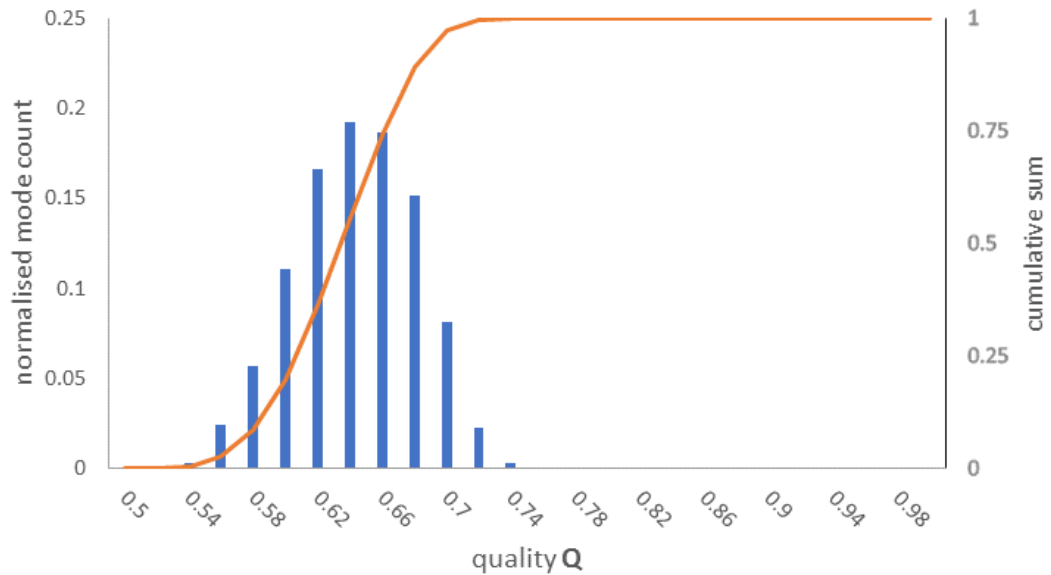


Figure 4–6: The cumulative sum of all modes above the threshold of 0.5 (orange) and the mode quality histogram give insight in the distribution of modes and help to adjust the quality threshold to obtain a higher amount of high quality modes.

each voltage change to compensate for piezoelectric hysteresis. The mode selection can be later applied to the PCD measuring the reproduction as in Section 4.4.7.

4.4 RESULTS

The idea to use a commercially available polarisation controlling device (PCD), that relies on piezoelectric fibre squeezing was discussed in the previous Section. Although the PCD is used in polarisation control, its utilisation for LP_{11} mode generation at selected angles has not yet been established. In the following this is examined, with the goal to build a rotation enabled DBLT. When the mode generation and manipulation was well enough characterized to ensure stable reproduction of wanted signal, the next step posed in building a dual beam laser trap. The detailed experimental approach can be found in the separate methods Section 4.3.2.

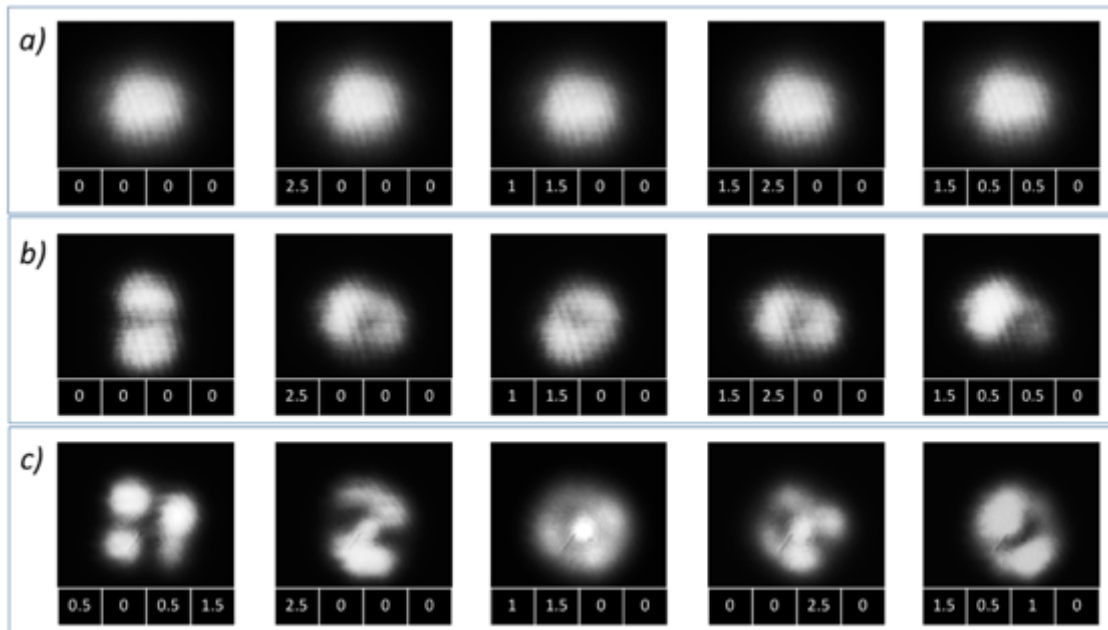


Figure 4–7: The first performance test of the polarisation controller for higher order mode manipulation. The manipulation is demonstrated in row a) for a straight splice of a SMF onto a DMF. After, for an offset splice of roughly $4\mu\text{m}$ in row b) and for a shorter wavelength of 631nm in c). The voltages applied to the four piezo-electric elements are displayed for each signal in Volts. Row a) shows that for a straight splice applying different voltages to the PCD had essentially no effect on the intensity pattern. Practically only the fundamental mode is present even after manipulation. In row b) the offset splice induced a massive increase in the coupling of the LP_{11} mode into the fibre. Although most signals are not pure modes the content of dual lobe mode was heavily improved. The same voltages as in a) were applied to b) causing a big impact on the mode mixing. The last row c) shows the capabilities for the PCD manipulating even higher order modes. By coupling light of 631nm instead of 1070nm into the system different higher order modes could be observed. Mainly a four lobed pattern (LP_{21}) and a doughnut mode with a brighter maximum in the centre (LP_{02} or HE_{02}) could be detected. The rightmost image looks like a dual mode with a ring pattern. It could be a more smeared out LP_{12} mode, a mode with a dual lobe pattern central and two sickles around.

4.4.1 First use of the PCD

To investigate the capabilities of the polarisation controlling device (PCD) for mode manipulation, dual mode fibre (DMF) was spliced onto the single mode fibre containing the laser signal. As row a) in Figure 4–7 shows, a straight splice between the two types of fibre did not couple the LP_{11} mode into the DMF as expected, with predominantly the LP_{01} mode being present. The capability of the PCD to manipulate the intensity profile is shown for different voltage combinations at the four piezo-electric fibre squeezers, as can be seen, the differences in the laser signal was negligible and the fibre squeezers were not able to couple the light into higher order modes within the DMF. To test the capabilities to manipulate higher order modes, specifically the LP_{11} mode, an offset splice was implemented, building upon the work of Kreysing *et al.*²⁰. Row b) displays the improved mode coupling, while the same voltages as in row a) were applied. The first image starting from the left displays a LP_{11} mode signal that was of quality, good enough to align cells reliable. For further reading on the topic of launching the fundamental mode off centre into a dual mode fibre the publication of Chakravarty *et al.*¹¹⁶ is recommended. As the laser in use could also deploy light at a shorter

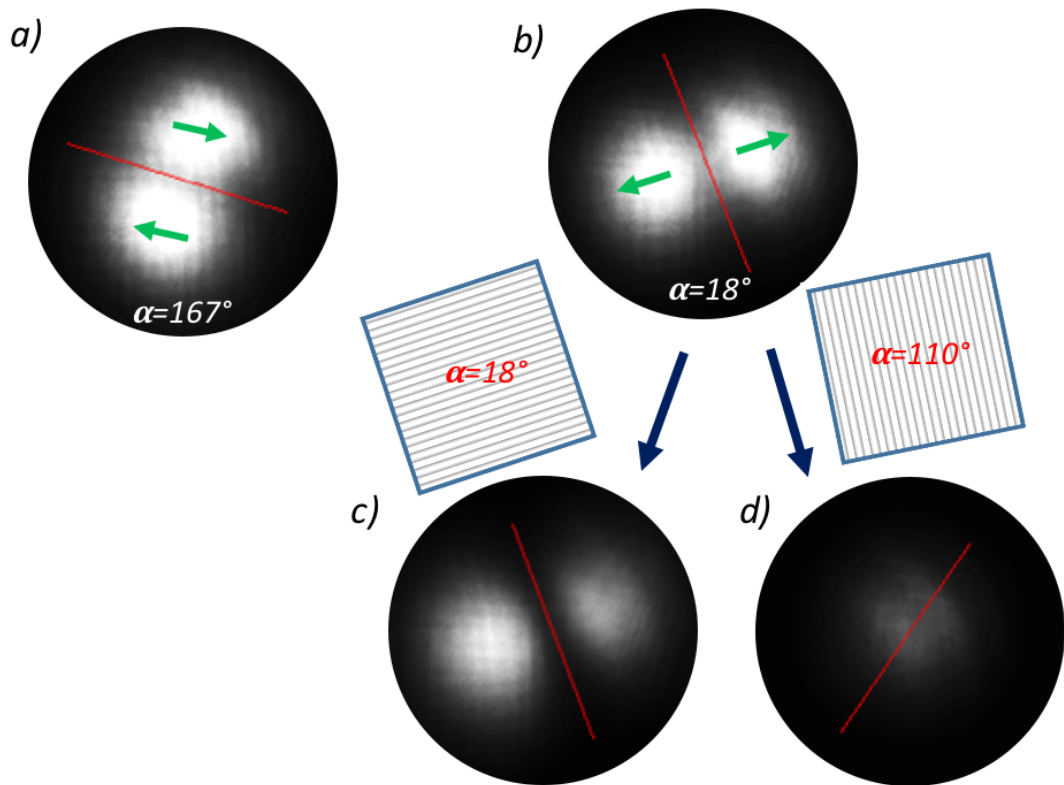


Figure 4–8: Both possible degenerate polarisations of the LP_{11} mode were observed. This is shown in **a)** and **b)**, indicated by green arrows. The polarisations were measured by checking the angle of a mounted linear polariser for maximum and minimum intensity. The mode angle is indicated in red and is either parallel or perpendicular to the polarisation. **c)** shows the signal of **b)** after the filter is inserted in the beam path with an angle of 18° . The intensity is lower than in **b)**. This was due to the presence of the fundamental mode in the unfiltered signal of **b)**. **Figure d)** shows the EH_{11} mode after adjusting the polarisation filter for the overall minimum intensity at 110° , perpendicular to the orientation of the LP_{11} mode. In order to make the fundamental mode visible, the brightness in all pictures was increased by 40%. The saturation of the detector is not present in the original data.

wavelength, namely 631nm, the operation of the PCD with a shorter wavelength was also investigated. Higher-order modes than the LP_{11} mode were a result as shown in Figure 4–7 **c)**. The first image displays a four lobe like pattern that indicates the propagation of a LP_{21} mode, while the third image displays a bright maxima in the centre surrounded by a ring mode, commonly noted as the LP_{02} mode. The fourth picture shows both the LP_{21} and LP_{02} mode patterns superimposed. The second and fifth image can not clearly be identified. From the V-parameter of the red light lying in at 5.72 many more modes are theoretically possible as it exceeds three cut-off points of 3.83, 5.14 and 5.52, but they were not observed. This initial study clearly shows the capabilities to manipulate higher order modes using a PCD and so further investigation was carried out to determine if it can be used to create a full 180° rotation of an LP_{11} mode suitable for cell trapping and rotation.

4.4.2 State of polarisation

The different possible degenerate states of polarisation of the LP_{11} mode are either parallel or perpendicular to the line of minima, as shown earlier in Section 2.3 and Figure 2–9. Measurements via a polariser (LPVIS100, Thorlabs), shown in Figure 4–8, verify that the PCD is capable of producing both degenerations, from the same initial state of polarisation launched into the device. While Figure 4–8 a) and b) show two LP_{11} modes with the different polarisation states, c) and d) resolved mode b) further. The polariser was inserted at 18° (parallel to green indicators of b)). The two lobe mode was lower in intensity, by 32% as without the filter, the mode signal was not pure and the rest of the intensity is present as fundamental mode (shown in d)). The additional fundamental mode could be solely obtained when the polariser was set roughly perpendicular to the polarisation of the LP_{11} mode at 110° ($+92^\circ$). In all images the angle of polarisation was measured by searching for the signals minimal and maximal intensity by adjusting the polariser.

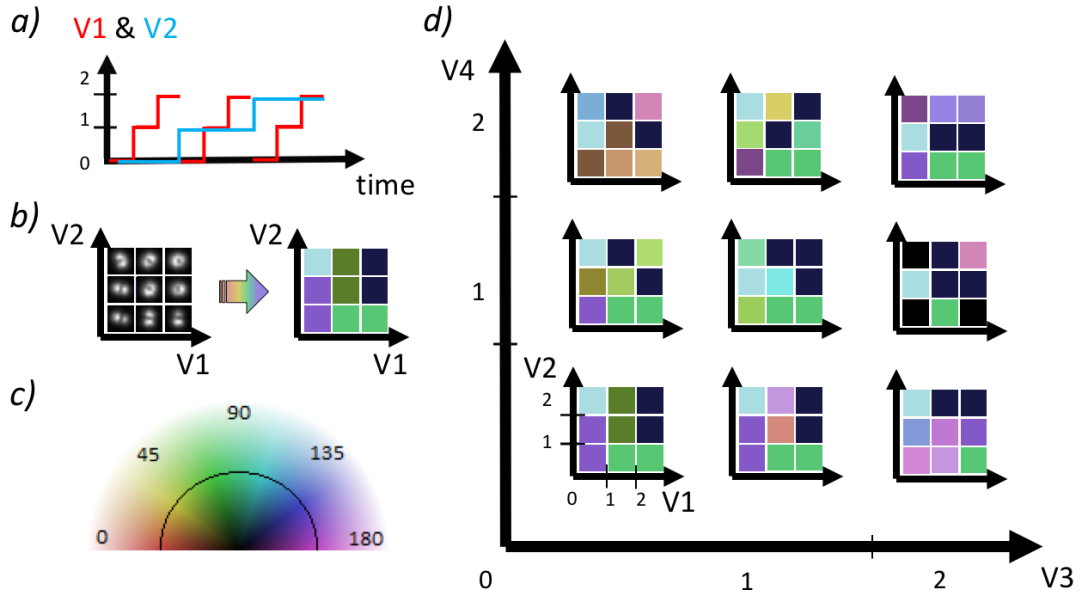


Figure 4–9: The raster scanning procedure of the PCD explained. **a)** The PCD was used for scanning through different voltage combinations. This process is explained in the following with the help of the schematics **a)-d)**. In this basic example the maximum set voltage for every piezo fibre squeezer is 2 Volts and the number of steps 3, whilst counting step 0. Thus, the voltages are 0V, 1V, and 2V. Schematic **a)** illustrates the first nine steps of this example scan. The input V1 (red) is increased in two steps. After V1 reaches the maximum value it is set back to 0V and V2 (blue) is increased one step to 1 Volts. The V1 ramp is executed again until the maximum voltage is reached and V1 is set to 0. V2 is increased to 2 Volts and the V1 ramp is executed once more. Resulting mode signals are presented in **b)**. This tile forms one 2D sub-scan as shown in **b)** and the lower left corner of **d)**. The whole range of the four piezo fibre squeezers is scanned through the possible combinations in a similar manner. As described in **a)** the voltages V1 & V2 were applied first until one 3x3 Section was completed as shown in **b)**. **d)** After the completion of this sub-scan, input V3 will be increased one step and V1/V2 will be ramped again. Once the row for increasing V3 reaches 2V, the fourth voltage V4 was increased and the procedure was repeated until all possible voltage combinations were applied. To enable a quicker overview of the whole scan, the two parameters LP_{11} mode angle and quality were transformed into a coloured representations, using the colour-wheel shown in **c)**. The mode quality is symbolised from 0 quality (black) to the maximum quality of 1 (bright colours). The black half circle indicates the used quality threshold of 0.5. Red signifies a low angle, opening up the coloured spectrum towards green for 90° and purple for 180°. **d)** shows how the information of a scan in all four voltage dimensions can be represented via the colour coding.

4.4.3 Polarisation controller voltage ramp

To investigate the full capability of the PCD to cast LP_{11} modes at different angles, a raster scan over a set working range of all four piezoelectric fibre squeezers was carried out. For simplicity the number of steps for all four piezo elements was the same number n , resulting in a total of n^4 voltage combinations applied over all piezo elements. The voltage ranged from V_{min} to V_{max} , while V_{min} was set to 0 Volts in most cases, V_{max} was kept commonly the same value for all four fibre squeezers. As V_{min} was counted as the first step the incremental voltage change of each step becomes $\frac{V_{max}}{n-1}$. In the example of Figure 4–9, V_{max} equals 2V and the number of steps per piezo is 3, so the voltage step-size becomes 1V. The whole scan builds up as described below and shown in Figure 4–9 a). First V1 (red) is increased stepwise until the maximum voltage was reached. After V1 was set back to 0, V2 (blue) is increased one step and the ramp of V1 is carried out again. This repeats until the 3x3 sub-scan was completed as shown in Figure 4–9 b). The laser signal for each voltage step is captured as a frame of an

AVI-file. The mode quality and angle are measured as discussed in Section 4.3.2.1 and 4.3.2.2. After, they are converted into a coloured representation, as shown on the right side of Figure 4–9 b), by using the colour wheel of Figure 4–9 c). In more detail, the first mode (bottom left) in Figure 4–9b) has LP_{11} character (bright in colour and not black) and has an angle of approximately 170° . Compared to the colour-wheel this translates into the purple tile closest to the origin. The next mode also has LP_{11} character and an angle of approximately 90° , leading to a representation as a green tile. To map the whole possible space of voltage combinations for all four piezo elements this V1&V2 block of 3x3 has to be executed for all selected V3 and V4 voltages. This is signified with V3 increased in the horizontal direction and V4 vertically, resulting in $3 \times 3 \times 3 \times 3$ or $3^4=81$ voltage combinations applied to the piezos. Each voltage step above 0V extended the piezo element and as such deformed the fibre a small additional amount. The first nine steps, as discussed in a) and b), refer to the left lower corner of Figure 4–9 d) and create the first block of the raster scan. This 3×3 or $n \times n$ block is repeated for increasing V3 and V4, the same manner as V1 and V2. In the sub-scan V1&V2 one tile equals one data frame. In the whole scan for increasing either V3 or V4 one $n \times n$ block is applied. Obtaining the colour-map as shown in d) gives an impression of which mode angles are present and if the scan range can be reduced to obtain a full range of 180° . When changing fibre alignment of the DMF the input SOP that enters the PCD is changed, which leads to a different distribution of colours and thus mode angles. The optimisation for a more even distribution was part of the procedure in order to use the PCD more effectively.

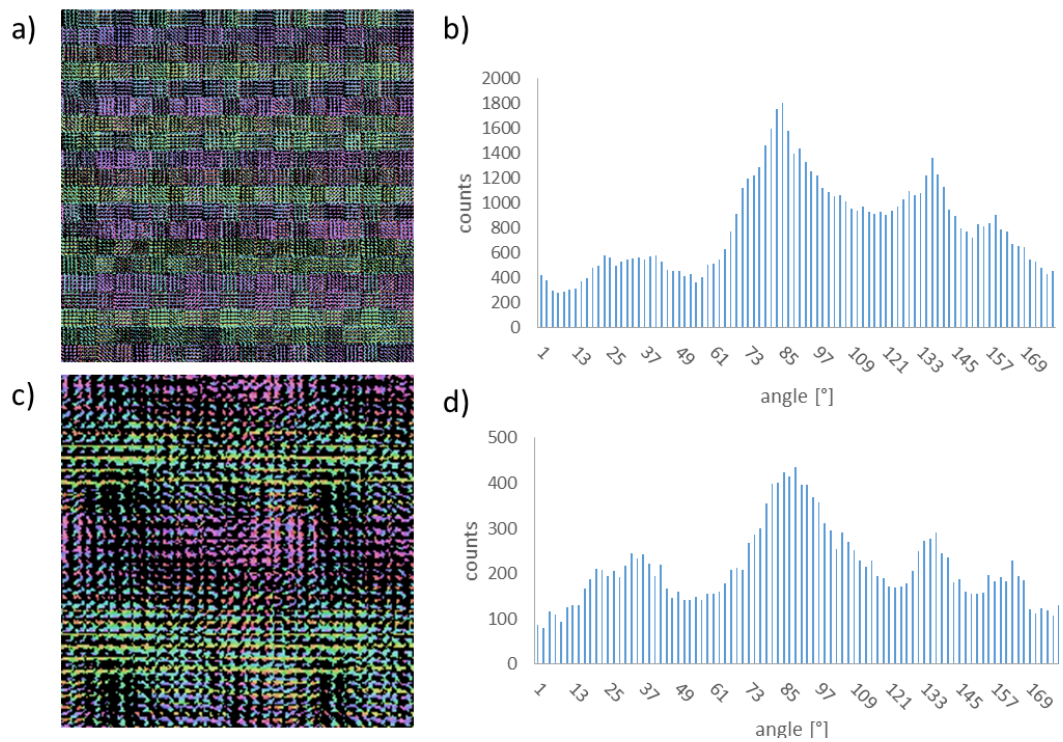


Figure 4–10: Comparison of differently sized raster scans. Choosing a smaller scan range provides a similar angle distribution of angles greater a quality >0.5 , as shown in the coloured representation and the corresponding histograms. **a)** An extensive raster scan of 0–4.75V in 20 steps with the associated histogram **b)**. Such a large, detailed scan takes approximately 2 days to acquire. While **c)** has a reduced scan range of 0–1.87V with 15 steps per piezo fibre squeezer, the associated histogram **d)** shows a similar angle distribution of the scan although the scan range was reduced by a factor of 2.5. This reveals that the full operation range of the PCD is not necessary to obtain all angles. The angle histograms were counted in bins of range 2° .

4.4.4 Full range raster scan

An extensive raster scan of 0 to 4.75V in 20 steps was completed in order to probe the capabilities of the PCD for the dual lobe mode generation. As shown in the histogram Figure 4–10 b), angles from 0 to 180° could be achieved continuously (for bins of 2°). However, it can be seen that mode angles of around 85° were preferred by this setup with 22% of the modes lying within 75° – 95° (6% of the angular range). Figure 4–10 c) shows a smaller scan range than in the first scan while the angle distribution shown in Figure 4–10 d) displays again a dominance in angles around 85° . This can be understood concerning that the experimental alignment of the fibre and thus the initial SOP coupling into the PCD did not change, only the scan range. Yet this is only a part of the explanation, the whole setup follows a periodicity which will be further interrogated in the next Section. Comparing to the scan in a)/b) the voltage scan range of c)/d) was 60% smaller. With the range of 0 to 1.87V the total number of steps was 70% reduced. Evaluating the data of the two histograms of Figure 4–10 the percentage of mode angles detected with a quality threshold greater than 0.5, in relation to the total number of steps, was slightly lower for the 0 to 1.87V scan, 38% compared to 46% in d). Yet, the smaller ranged scan displays a more even angle distribution. The peak at

85° was approximately twice as high as the count at 25°, compared to b) where it was nearly an increase of 4 times between the different counts in angles. Meaning, the higher scan range does not benefit the variety of angles. Therefore, smaller scan ranges can be chosen by inspecting the colour map or histogram. Whilst the histogram makes it easier to spot the overall angle distribution, the colour map above shows which voltage in V3 and V4 creates angles at a similar colour spectrum.

For example, in Figure 4–9 a) the mostly green horizontal lines indicate a mode angle of approximately 85°, it seemed to reoccur and the colour map helped to choose the smaller scan range of Figure 4–9 b). In b) the green horizontal break only repeated once, which lead to a less pronounced peak of the angle-histogram d) at angles around 85°. Since several voltage combinations resulted in the same mode angles, a full ranged raster scan was not of great benefit in order to calibrate the setup for the trapping and rotation of cells. Choosing a smaller voltage range, than the maximum of 5V, was applied in the following of this project and could reduce necessary scanning time. More scanning detail for the same number of steps could be obtained, since the voltage step size was smaller.

4.4.5 Repeatability in retardance

While inspecting the extensive scan further, magnified in Figure 4–10, recurring colour patterns, especially in the green/light blue and purple tones, could be identified globally. Yet zooming, in on different V1/V2 sub-matrices there was an underlying periodicity in smaller features. The inspected patches, outlined in white in Figure 4–10, were $V_3, V_4 = 1V + n * 1V$ apart; for $n=0,1,2,3$. When zoomed in on the patches great similarity could be discovered. Therefore, this occurrence was further explored in the following.

When a voltage of 1.16V is applied to the PCD, a π phase shift is generated between the degenerate linear polarisations for single mode light at 1550nm. The piezo element is acting as a half wave plate. The application of this voltage V_π was tested for the higher order mode manipulation with a similar effect for 1070nm. More necessary stress on the fibre was expected for a similar phase delay at the shorter wavelength of 1070nm compared to 1550nm, but the π phase delay was clearly visible at the same retarding voltage. So for single mode operation the full range of the PCD could achieve a retardance of each mode of several π . In fact four times, counted from 0V, as the maximum voltage divided by V_π is $\frac{5V}{1.16V} = 4.31$. Relating this to the scan in Figure 4–

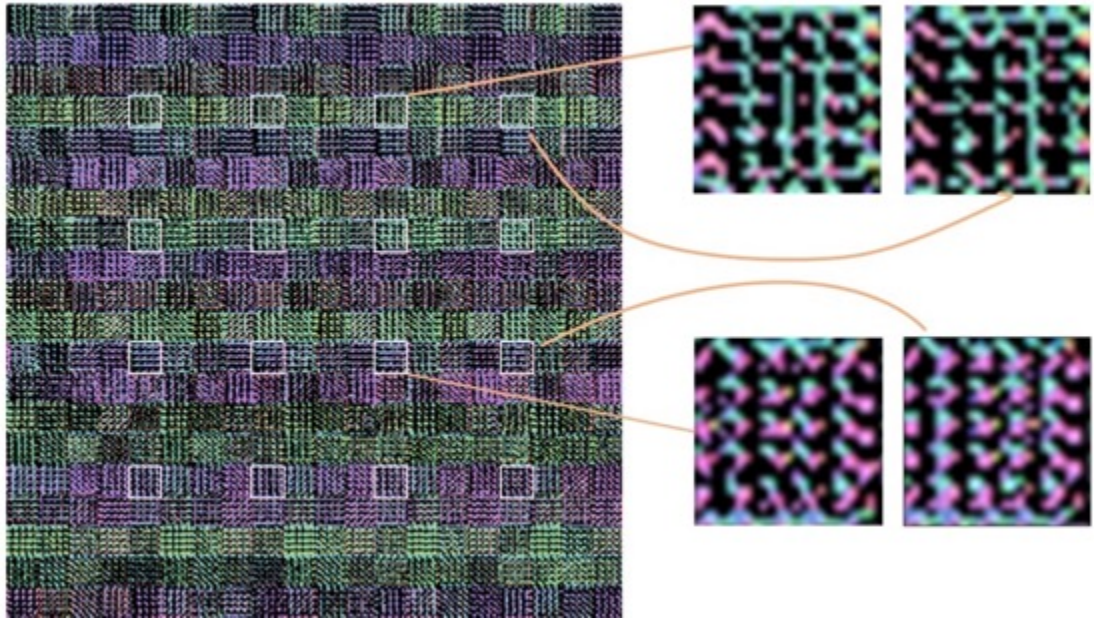


Figure 4–11: Repeated patterns in raster scan. The mode characterization matrix of the extensive raster scan discussed in the previous figure revealed further insight. Each piezo input was set from 0 to a maximum of 4.75V in 20 steps, resulting in a voltage step-size of 0.25V. Zooming in on the results and choosing examples out of the 2D sub-elements, with white rectangles highlighted, similarities could be discovered. On the right respectively two pairs of white regions are magnified and compared. The pairs each show great resemblance. This periodicity was voltage dependent. V3 was +1V higher for the right magnified sub matrix. This behaviour can be understood considering the piezo fibre squeezers adding retardance to the mode propagation. At a certain point the additional retardance causes a phase delay casting similar modes.

12 the $4V_{\pi}$ voltages were marked in white for V3 and V4. The modes with the starting voltages of $V_2=1.5V$, $V_3=0.667V$ and $V_4=3V$ (the area matching the first white double box from the left in Figure 4–12 b)) were investigated more thoroughly.

Since V_{max} was 4.83V, V_2 could be increased 2 times by V_{π} (or decreased once). V_3 3times and V_4 theoretically once (or decreased twice), as shown in Figure 4–12 b). If the PCD added the same phase delay of π for dual mode operation, mathematically this leads to 64 (63 additional to the original) possible examples of similar mode patterns per V_1 voltage change. $4 \times 4 \times 4$ times, $3+1$ (decrease) times for V_2 , 4 times for V_3 and $2+2$ (decrease) times for V_4 . Figure 4–12 a) shows the 30 data points for increasing the first piezo V_1 , while V_2 , V_3 and V_4 were varied by multiples of V_{π} , in order to find similar mode examples.

A selection of the actual signal is shown for a voltage ramp with no V_{π} offset. The various voltage combinations for 12 V_1 voltage ramps, of different V_2 and V_3 starting voltages, are displayed in the table above the graph. The graph shows the resulting angles plotted for increasing V_1 . The selection of 12 instead of 63 was made as for the other theoretically possible modes, a not negligible part of the modes was below a critical quality threshold and not resembling a dual lobe mode (four double lined white boxes in Figure 4–12 b) and $3 \times V_2$ in each box leads to 12 examples). The 12 V_1 ramps

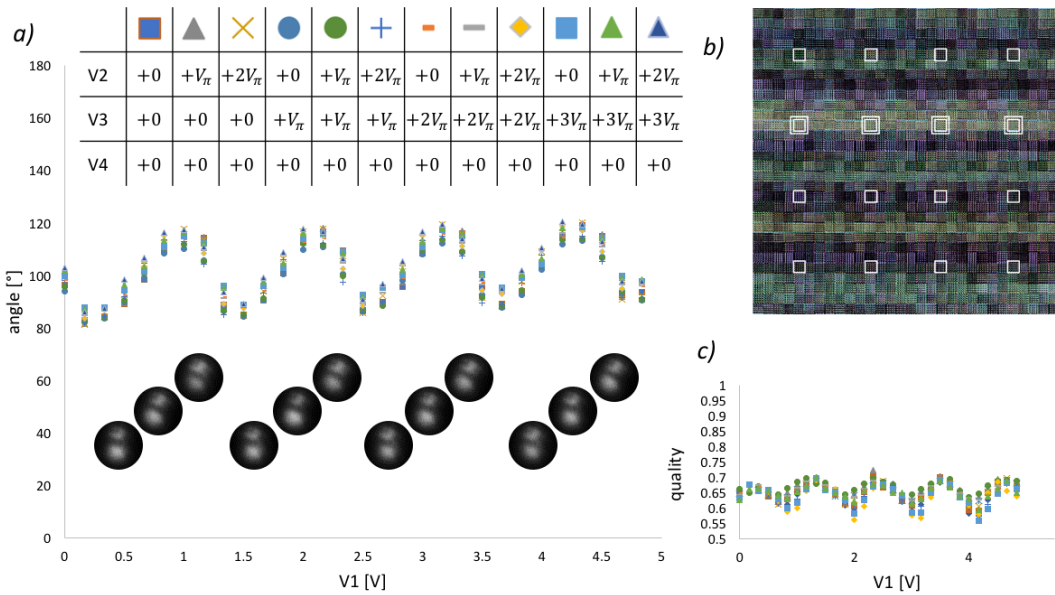


Figure 4–12: Adding a defined voltage $V_{\pi}=1.16V$ to the position in $V1$, $V2$, $V3$, $V4$ in the raster scan can result in recurring mode examples. a) The different colours and symbols in the graph represent one scan in $V1$ for different voltages of $V2$ and $V3$, following ascending multiples of V_{π} as written in the table above. An evident periodicity underlies also in the angle depending on $V1$ for the present state of polarisation. The possible examples for increasing or decreasing $V4$ by multiples of V_{π} are not displayed as they are dropping in quality and accuracy. The signal displayed below the graph in a group of three are all from the first column of the table and offset by V_{π} increasing in $V1$. b) The white boxes show the areas where theoretically recurring mode examples could be found, while the double boxes represent the areas where the in Figure a) drawn mode examples are situated in the whole scan. The individual qualities of the drawn mode examples are displayed in c) and follow a certain periodicity, as well.

displayed and their resulting signal either all had a reasonable mode quality or a high fraction such as 29 out of 30 modes. For increasing $V4$ by V_{π} the overall mode quality dropped down to as low as 15/30 of the modes being below the threshold. For the displayed 12 examples the similarity in quality is pointed out in Figure 4–12 c). Following the angle distribution over different $V1$, this in itself displays the periodicity.

The fact that a phase change in 180° or π did cast a similar mode can be understood considering that the LP_{11} mode has two degenerate states of polarisation. While a piezo element acting as a half wave plate might rotate the direction of the polarisation, the signal might still inherit the same intensity pattern. Although the actual state of polarisation in each fibre position the 4 piezo fibre squeezers act upon is unknown, following Section 2.3.1 and the retention of LP_{11} modes, it has to be assumed that the superposition of ring modes are affected in a certain pattern for increased stress resulting in another set of LP_{11} modes. This is in agreement with the discussion of Holleczeck *et al.*¹¹⁷ describing the classical and quantum properties of ring modes, a half wave plate inverts the local polarisation vectors of the ring modes. Interfering two ring modes that previously lead to the LP_{11} mode, lead to the other degenerate LP_{11} mode at the similar angle. But as increasing the individual voltages by V_{π} does not always result in a periodic recurrence of similar mode patterns, it is assumed that the whole system

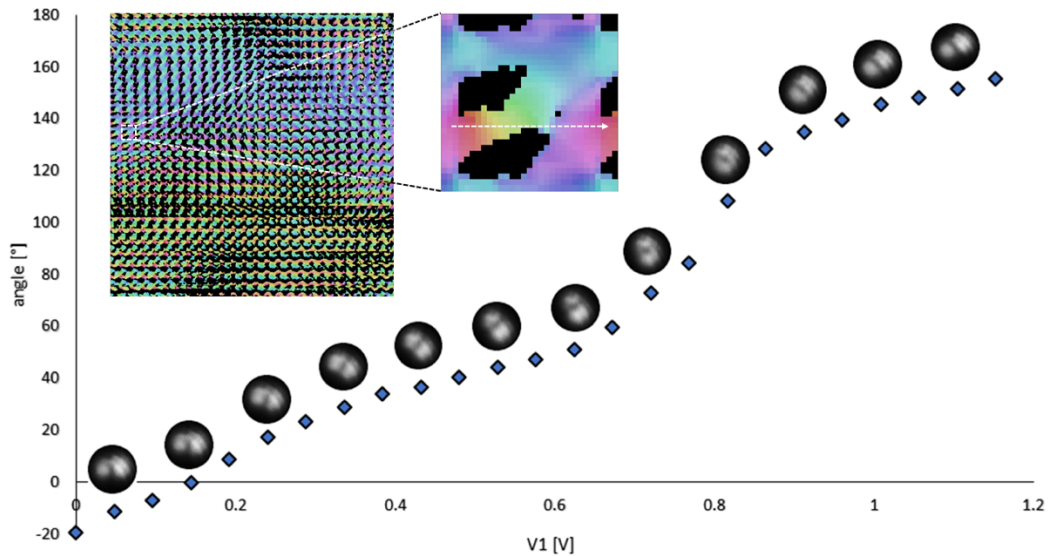


Figure 4–13: A monotonic change in mode angles over the range of 180° , whilst only operating $V1$. Top left inset, the scan of 25^4 steps over a range of $1.152V$ in all four piezo voltages. The sub Section, that was zoomed into, was located at $V3=0.048V$ and $V4=0.624V$. The white arrow at height $V2=0.288V$ in the magnified sub Section of the colour map, indicates the direction of travel and reveals the full spectrum of colours and thus angles. The received angles are plotted below. While the smallest angular change measured 2.5° , the biggest step was around 24° . For each second angle the captured signal is displayed.

drifts for bigger phase shifts and seemingly more so for changing $V4$. This might come down to individual voltage calibration which was not further explored. Further, the initial state of polarisation will play a role, especially for not fully polarised mode states and this might explain why periodicity is not always observed. In the next Section the acquirement of the full angle range in smallest retardance is explored by narrowing down the maximum range of the scanned piezo accentuations.

4.4.6 Full range of angles by actuating one piezo

As the goal is a monotonic rotation of cells, it is of interest whether such a monotonic mode rotation could be achieved by altering the voltage of only a single piezo. To investigate this, a very detailed scan of $1.152V$, just below the periodic voltage V_π , over 25 steps in each voltage, was acquired. To obtain such an extensive scan the experimental time measured around 54h, whilst each step of the ramp was allowed 50ms. Figure 4–13 shows the results of the scan in a 2D colour map. Zoomed in on a Subection of the scan for $V3, V4=\text{const.}$ a row containing the full colour spectrum could be revealed, as indicated by the white arrow. The angles found in this Section are plotted below, whilst the actual signal is displayed for every second mode. The angle did increase in a monotone fashion and continuously. The voltage step size of this scan was $0.048V$ (1% of the full range of the apparatus). As shown in the measurement this was sufficient to rotate the signal for up to 24.2° but also as little as 2.5° . When the goal is a 180° rotation of the LP_{11} mode this collapses a whole scan of 25^4 steps into 25.

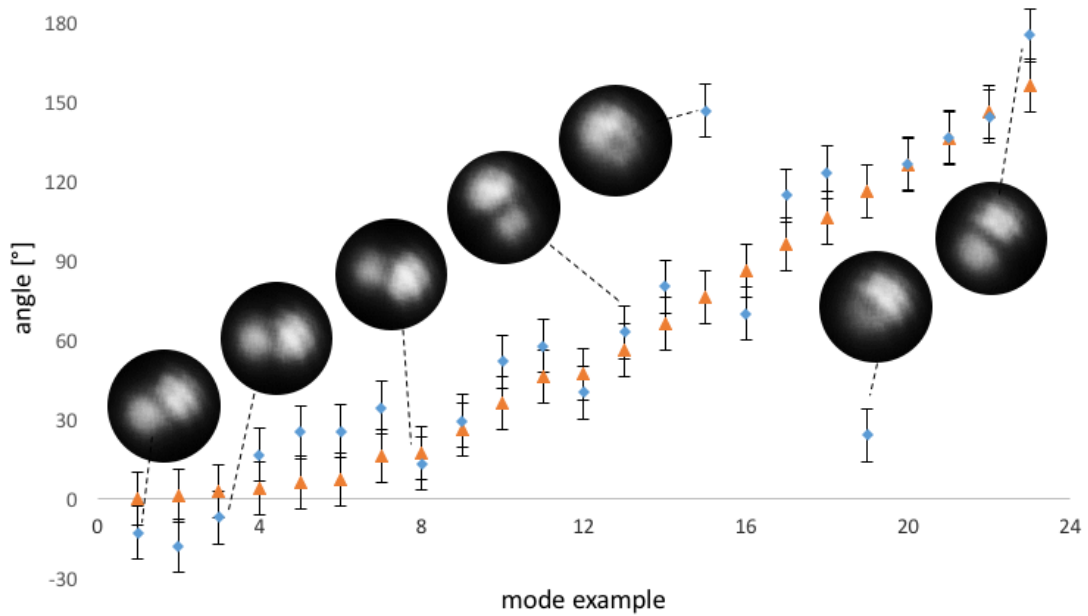


Figure 4-14: Reproduction of signals of a dual lobe shape rotated around 180° . The scan containing the dataset of the modes that were chosen to reproduce applied 0–1.5V in 20 steps. Orange are the original measured angles and in blue the reproduction. A systematic error of 10° was assumed. Examples of modes being reproduced are included, the modes of the outliers seemed to have lost their two lobe character, which explains the massive angle difference.

Although an angle change of 24° is not ideal for tomography as the non imaged sample volume wants to be as small as possible, this result was still seen as interesting and presentable. The optical fibre between this piezo element goes from un stressed to acting as a half wave plate undergoing linear birefringence. So in between those two extremes the fibre will act as a quarter wave plate, creating elliptical polarisations out of linear ones. As the input polarisation state and the perturbation of the fibre after the PCD are unknown it would require future investigation to find the underlying mode mixing concept to explain this rare behaviour of the PCD. For cell rotation the order of the applied piezo voltages does not matter and so the repeatability of modes, acquired by raster scanning is investigated in the following.

4.4.7 Repeatability of selected modes

As each raster scan provides an abundance of dual lobe modes across the range of possible orientations, a selection of modes and therefore voltage combinations was made. The selected modes were sorted in ascending order of their mode angle, to obtain a smooth rotation of the LP_{11} signal. Since the piezoelectric effect of each fibre squeezer undergoes hysteresis, the extension each fibre squeezer undergoes was not only dependent on the voltage, but the history of the voltages that were applied before. In the raster scan the voltages always follow the same ascending history, but a selection of modes by quality and angle, mostly leads to a random voltage path. Although the

monotonic increase of only V1 showed the rotation of the dual lobe mode in the Section described above, this was not used in order to reproduce selected modes for cell rotation. Since the scan required to find such behaviour was one of the most detailed and time extensive. Further, the biggest angular difference of two consecutive modes was 24° and not ideal for the cell orientation for tomographical applications.

In order to find the required voltages to produce the modes in a faster time, a less detailed scan is used to improve the workflow. For a generic raster scan and its selected modes, hysteresis could be overcome by adding a reset step in between all applied voltage combination of the selected modes. Each input was set to 0 volts before moving on to the next step of increasing V2,3 or 4. Figure 4–14 shows the reproduction of modes chosen out of a 0 – 1.5 V scan in 20 steps. In some examples the mode quality suffered and especially the outliers are modes where the mode angle was not measured reliably, since the dual lobe shape was altered (see Figure 4–14). This deviation of selected vs reproduces modes was identified to be due to driving the PCD too rapidly. When switching between the stresses so fast, that the fibre stressed under each piezo fibre squeezer was not fully in its new equilibria, the system might have drifted when the mode was imaged. To improve this, the time between changing the voltages and taking the image was increased to 100ms, allowing the fibre time to equilibrate to the new stresses. Due to the increased acquisition time, the number of steps was reduced from 160000 to 10000, to provide a reasonable duration to acquire a raster scan in 2 h 46 min (compared to 54 h and 50 mins for Figure 4–13).

Figure 4–14 shows the successful results for the scan and signal-reproduction with increased relaxation time. All selected angles and the reproduction results were laying in the range of the standard error. In order to probe the suitability for trapping the power in the various angled modes was estimated, the greyscale pixel values of the field of view of each signal were summarised and compared. The maximum deviation in the overall intensity was $\pm 6.2\%$, which would result in only a small change to the trapping stability. Compared to the power stability claimed by the laser supplier IPG Photonics that is $\pm 1\%$ and the activation loss of 0.23% for operating 1550nm in the PCD, claimed by General Photonics, the use of the PCD below the supported wavelength range of 1260-1650nm appears to induce more instability. Yet, this reproduction of selected modes is well suited for cell alignment.

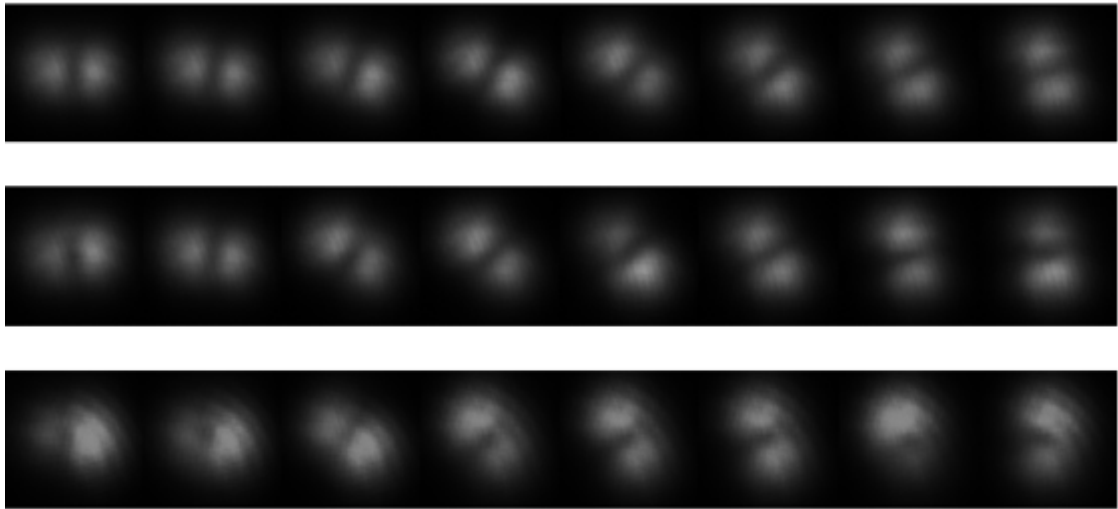
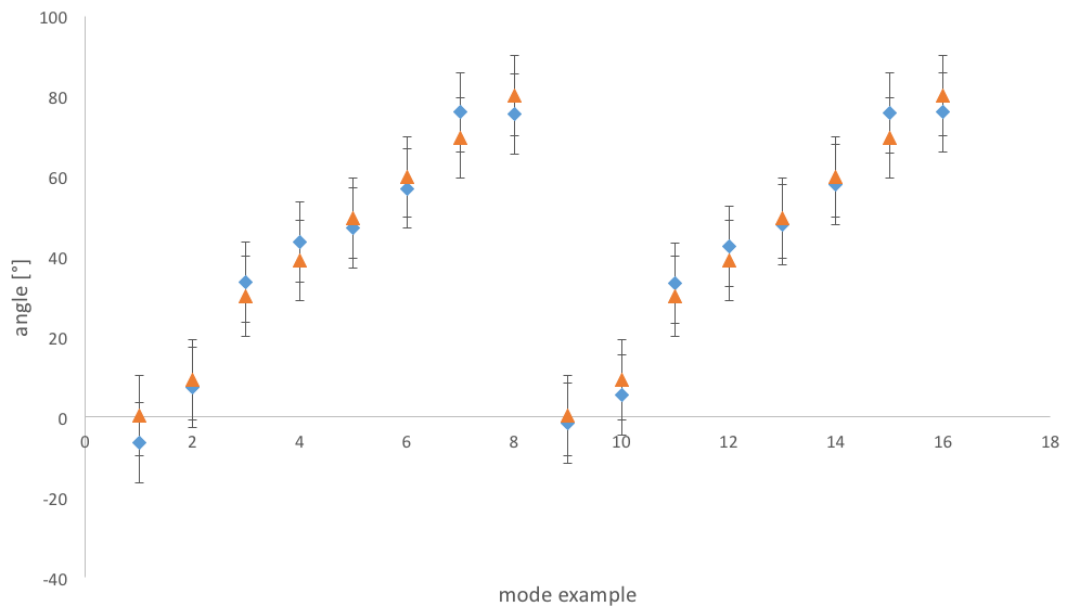


Figure 4–15: More accurate reproduction of rotated laser modes. As shown in the graph the mode angles of the reproduction in blue, fit better to the original angles in orange better than previously in Figure 4–14 and lie between the standard error. The voltage combinations were applied two times. Below, the mode signal of the reproduction is displayed. Top row: The chosen modes out of a 10 step 0-3V voltage scan. Middle row: The mode angles were well reproduced with a good quality. Lower row: Modes in the same angles of Figure 4–14 for comparison. Overall, the quality was poorer, for example the first and the last but one mode could cause a total misalignment of the cell. Measuring the light intensity of the top rows of the 90° reproduction the maximum deviation from the mean was 6% and would not affect theoretical trapping.

4.5 DISCUSSION

In this Chapter it was shown that the piezo fibre squeezer based polarisation controller is capable of producing LP_{11} modes at various orientations, when operated in a dual mode fibre regime. Both degenerate states of polarisation of the LP_{11} modes could be achieved through piezo fibre squeezing, as shown in Figure 4–8. Recalling the background Section 2.3.1 and the representation of the dual lobe mode as superposition of the ring modes, this shows that both the TM_{01} and TE_{01} modes were obtainable through piezo fibre squeezing. Otherwise only one of the two degenerate polarisations

would be possible for an LP_{11} mode. However, the sensitivity of a dual mode fibre to external stress, means that the transform function of the fibre changes when the fibre is moved or stressed. This in turn requires the system to be calibrated before each experiment by scanning over the available piezo voltages. The scan voltage range in order to cast an angle distribution over the whole range of 180° could be successfully reduced immensely, as shown in Figure 4–10. This helps to reduce necessary scanning time from 54h to 2h46min, while still finding enough modes of each orientation for the application in cell rotation. Further, periodic behaviour of the PCD was documented in Section 4.4.5, displaying similarities as has been seen for single mode operation. The half-wave voltage V_π seemingly also phase shifts the polarisation of the LP_{11} mode a similar amount as a half-wave plate would do for single mode operation. Although this was not reproducible for the full possible range of operation of the PCD as shown in Figure 4–12. This indicates drift in the system or dependency on the initial state of polarisation present in the piezo fibre squeezers. A monotonic LP_{11} mode rotation over 180° could be discovered by incrementing only one piezo fibre squeezer. This is fundamentally different from single mode operation of linear polarised light. In single mode operation for the increasing stress applied by one fibre squeezer, the polarisation changes from linear to elliptical. The stress on the fibre changes the phase and amplitude difference between the horizontal and perpendicular polarisation components of a linear polarisation and an overall linear polarisation can not be maintained. Despite this, LP_{11} modes are linearly polarised, thus the altering of the polarisation angle must be by changes in mode mixing. Likely the found mode examples are not purely linearly polarised, as this conflicts the properties of linear birefringence. To find this monotonic mode angle increase using only one piezo fibre squeezer was quite rare and time consuming. In order to prepare the setup for future cell rotation, a selection of increasing mode angles has been successfully reproduced. Comparing to the literature the piezo fibre squeezing based LP_{11} mode manipulation approach was of lower cost, higher precision and less alignment intensity than for example the use of a spatial light modulator²¹. Further, the manipulation was conceptual all in fibre. When building a laser trap, this is desirable as it is easier to use, safer and less likely to misalign itself. Hong *et al.*¹⁰⁴ in their recent publication showed a low cost approach to LP_{11} mode rotation based on fibre loop paddles. Although, this approach is promising, a monotonic rotation was not shown in their publication and no data for the correlation between mode angle and fibre loop paddle manipulation was displayed. A monotonic rotation, without intermittent laser signal changes, that differ from the LP_{11} mode, is

needed for consistent cell rotation, as a non LP_{11} mode in between cell orientations is prone to lose the cell's alignment. If the control over the cells orientation has been lost, reconstruction of the cells movement becomes hardly feasible. Another interesting concept of LP_{11} mode orientation, discussed in the background Section, was the use of photonic lanterns¹⁰⁵. But, as the number of possible orientations is limited by the geometry of the photonic lantern, the discussed piezo fibre squeezer based approach is favourable to gather more Sections and enable a smoother 3D reconstruction of the specimen. The all in fibre based approach, presented in this thesis, is one step closer to a black-box setup that is easy to use once setup and calibrated. Ideally it will be implemented in a biology lab with only a short amount of training necessary, to investigate biological questions by non-physicists.

4.6 CONCLUSION

Overall, the piezo fibre squeezer polarisation controller has proven itself to be suitable for LP_{11} mode generation and orientation in dual mode fibre operation. A broad range of LP_{11} modes at different angles and with varying quality could be cast, when all four piezoelectric elements were used. Rapidly changing between the modes of interest while maintaining a high quality was possible. This selection could be ordered in any fashion but as the main goal of this research was the rotation of biological specimen in a dual beam laser trap, the modes were selected in ascending order of angle. The successful reproduction of this selection could be achieved, after adjusting the working speed of the piezo elements while avoiding hysteresis of the piezoelectric fibre squeezers. This was the first time to present knowledge that by using a piezo fibre squeezer based polarisation controller the linearly polarised LP_{11} modes were rotated. The experimental results give an encouraging outlook to trap and rotate single cells with the given setup. This will be investigated in the next Chapter.

5 TRAPPING AND ROTATING IN A HIGHER ORDER MODE CELL ROTATOR (HOMCR)

The main goal of the research presented in this thesis was higher order mode manipulation enabled cell rotation in an all-in-fibre dual beam laser trap. In the introduction, the advantages of using optical techniques were presented and a method of orienting cells based on anisotropic fibre-mode rotation was shown. Existing techniques for performing this mode rotation are limited in their applicability and in the previous Chapter a new technique was demonstrated using a polarisation controller, based on piezo-electric fibre squeezing. It was shown that dual lobe modes could be cast at different orientations in a controllable and repeatable manner. After laser mode manipulation, the other pillar of this project that leads towards the higher order mode cell rotator was cell trapping.

The capabilities of the Dual Beam Laser Trap (DBLT), have been discussed in the introduction and further in its ability for mechanical probing of cells in Chapter 3. It has been previously shown that by exchanging one of the two laser beam arms with a higher-order mode beam, it is possible to hold and rotate a cell^{20,47}. However, these proof of concept techniques were far from ideal. The use of a novel higher order mode modulating setup consisting of a few-mode fibre and a piezo-fibre-squeezer will enable the DBLT for cell rotation without requiring fibre rotation or complex beam manipulation. This Chapter describes the progress made in two parts: (1) building DBLTs that are higher order mode modulation-enabled and (2) rotating mammalian cells successfully. Several different devices were investigated and two different types of dual beam trapping devices will be highlighted, namely a closed microfluidic chip and an “open” DBLT.

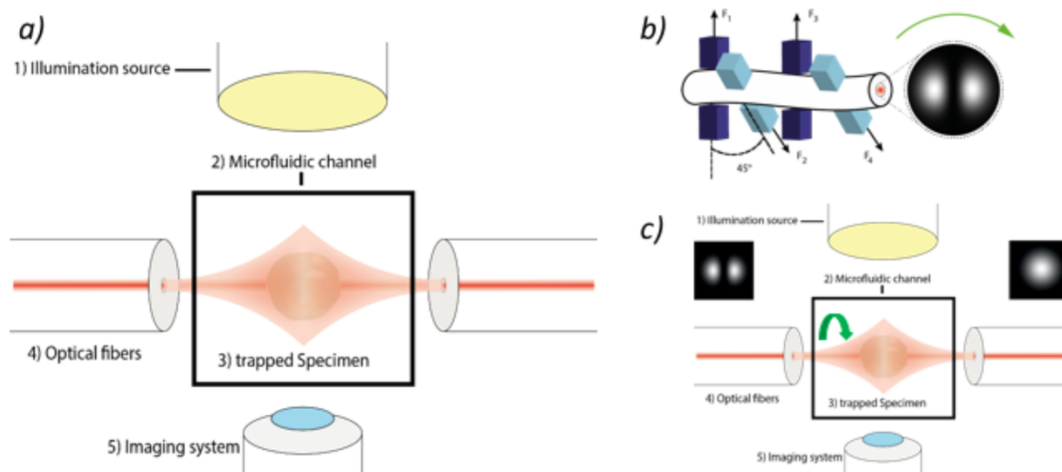


Figure 5–1: The idea of the HOMCR. a) Schematic of a microfluidic dual beam optical trap. Cells are flushed into the channel. Once an object of interest is in the trapping area the laser is turned on and the specimen is trapped. b) By modulating the laser-light using a piezo-squeezer based polarisation controller, as discussed in the previous Chapter, it is possible to set the dual beam trap for the rotation of cells. c) The conceptual outline of the higher order mode cell rotator. A DBLT consisting of a dual lobe mode on the left and a Gaussian beam on the right. By rotating the dual lobe mode the trapped specimen follows the orientation.

5.1 ORIENTING LIVING CELLS IN SUSPENSION

5.1.1 Tools for cell rotation

Rotating cells enables views from different sides to be captured, allowing its 3D structure to be visualised. However, precise control over the individual cell has been difficult, despite a long history of study. Many techniques have been developed over several decades. Early techniques involved holding the cell firmly in a micropipette which was then rotated, however this technique requires strong contact between the cell and an object, which may influence both the cell and the imaging, and in addition it is very difficult to rotate the micropipette around an axis perpendicular to the optical axis, thus reducing the 3D reconstruction. For these reasons, primarily non-contact methods for cell rotation will be considered here. One of the earliest systems described used an alternating electric field that creates torque on the living specimen which was already realised in 1982 by Holzapfel *et al.*¹¹⁸. A major limitation of this early established concept was that the rotation induced by two or four¹¹⁹ electrodes was not perpendicular to the microscope's imaging plane and thus not useful for tomographical purposes. In subsequent work on the same concept, Benhal *et al.*¹¹⁹ found a way to rotate bovine oocytes perpendicular to the imaging plane, which in theory enables tomographic imaging, although this was not shown. The schematic of this setup is shown in Figure 5–2 a). The setup involves four vertical electrodes (red) that manipulate the cell parallel to the imaging axes, separated through an insulator cover (yellow), from the indium tin oxide (ITO) electrodes below the specimen (green). Applying AC voltage to the

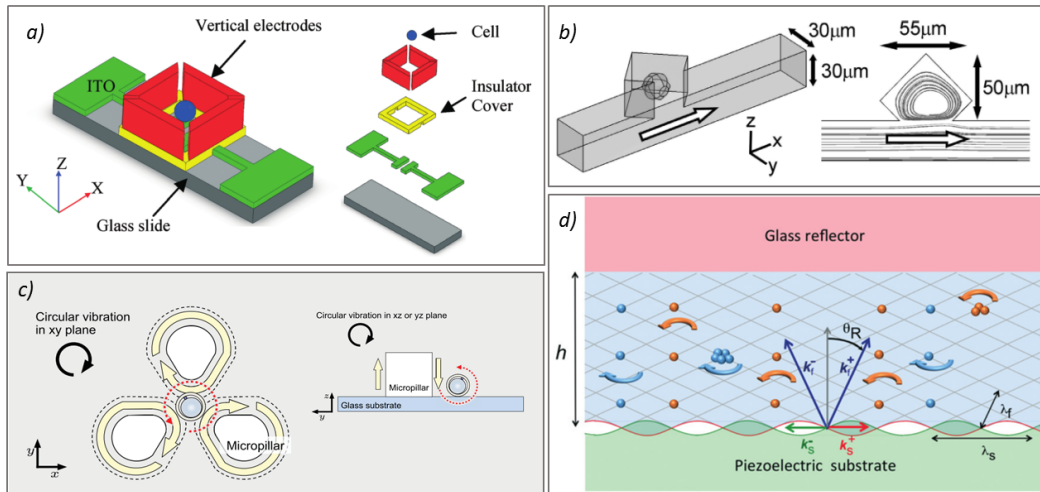


Figure 5–2: Methods for non-contact single-cell rotation. a) Two ITO electrodes (green) are capable of tomographical rotation of the in blue indicated dielectric particle. The ITO electrodes have to be insulated (yellow) to not short circuit with the vertical electrodes (red). The red electrodes are capable of rotating the specimen in plane. Figure taken from Benhal *et al.*¹¹⁹. b) The liquid flow through a micro channel creates a whirl at an added cavity. A trapped specimen will experience the flow profile indicated on the right hand side of Figure 3b). Figure by Shelby *et al.*¹²⁰. c) Using piezo-electric attenuators and a certain architecture of micro pillars can be used to rotate mouse oocytes in plane (left hand side) and out of plane (right hand side). Figure by Hayakawa *et al.*¹²¹. d) Surface acoustic waves are induced from the left and right. Inducing a lag between the emitters lets the wave fronts propagate in a manner that can rotate trapped particles, such as cells.

electrodes results in forces acting on the dielectric sample and thus stirring it.

Unfortunately, good imaging was not realized as the bottom electrodes below the sample were not fully transparent. Yet, Huang *et al.* build upon this technique. By changing the four vertical electrodes (red in Figure 5–2) into four square pillars of carbon-black-nanoparticle-PDMS (Polydimethylsiloxan), with one of each square pillars corner pointing at the trapped sample. The pointing corners are more pronounced and the electric field created by the electrodes was able to orient cellular sample in more ways than previously. While the imaging quality improved as only one ITO bottom electrode was used, the rotation of the trapped specimen was continuous and fast, inducing motion blur. The HOMCR is intended to do the opposite, holding the sample stable at desired orientations.

Instead of using the electric field Shelby *et al.*¹²⁰ employ a laminar flow field that due to a particular micro-channel geometry applies rotational forces on the probe. In Figure 5–2 b) the trapezoidal shaped micro-chamber attached to a microfluidic flow channel is displayed. On the right hand side of the figure the circulating vortex is shown in its flow profile. Trapping a sample in this cavity causes it to rotate. Although, the trapezoidal cavity and circular flow did not allow for good imaging of the sample and the system required a potentially photodamaging optical tweezer to position and hold the cell correctly in the chamber.

Hayakawa *et al.*¹²¹ engineered a lab on a chip device that combines a special geometry of micro pillars with an xyz piezoelectric actuator that induce vibrational flow and were capable to rotate mouse oocytes. The sample was placed via pipetting in the microarray so that it was situated between 3 micro pillars, as can be seen in Figure 5–2 c). The flow of a micro vortex was created by either moving the piezoelectric actuator rectilinear in xy or xz, so the sample could be rotated in different orientations. However, as with the other microfluidic techniques, a constant torque was applied to the cells, resulting in constant rotation, which would induce blur in resulting images. In the work of Bernard *et al.*¹²², as can be seen in Figure 5–2 d), the vibration of piezoelectric substrate was used to create surface acoustic waves (SAWs) that induced a flow field of standing waves inside a cavity. The standing waves created a two dimensional grid-like pattern with nodes of peaks and valleys that the cells align to. Now, when applying a phase lag between the two rectangular standing waves, the waves counter propagate and the particles trapped in the nodes of the surface acoustic waves experience a swirling motion. Although the experimental setup was very complex the quality of imaging was rather poor. Before moving the discussion from operation principles that either use an electric field or a fluid flow field to rotate cells, towards principles utilising the field of laser light, a very logical approach is briefly discussed. To get volumetric 3D data of cells one reasonable approach is to prepare the specimen in a light permeable tube (micro capillary) and rotate this tube above the microscope's objective^{123,124}. In order to do so Miao *et al.* wet-fixed the sample and suspended it in an optical gel so that the movement of the rotation stage together with the connected micro-capillary is translated directly on to the cells (shown in Figure 5–3 a)). The use of this optical gel requires that the samples are fixed, which kills the cells, and as the tube can only hold a few specimen higher throughput could not be achieved. Further, the fixing of the sample makes it impossible to re-obtain the sample alive, but when samples are precious or have special properties, that were revealed through the rotation, re-obtaining the cells and investigating further questions about the specimen would be of interest. Thus, investigating living specimen with a less invasive approach is preferred.

Light has been shown to be a useful non invasive tool for manipulating microscopic objects, and has been able to hold and rotate cells using different methods. One approach via holographic optical tweezing was realized by Habaza *et al.*¹²⁵. As a spatial light modulator is able to create various beam profiles, coupling the light into a high NA objective, the trapped cells can be manipulated in new ways than with a classical optical tweezer. Figure 5–3 b) shows the experimental setup of Habaza *et al.*, used for the 3D

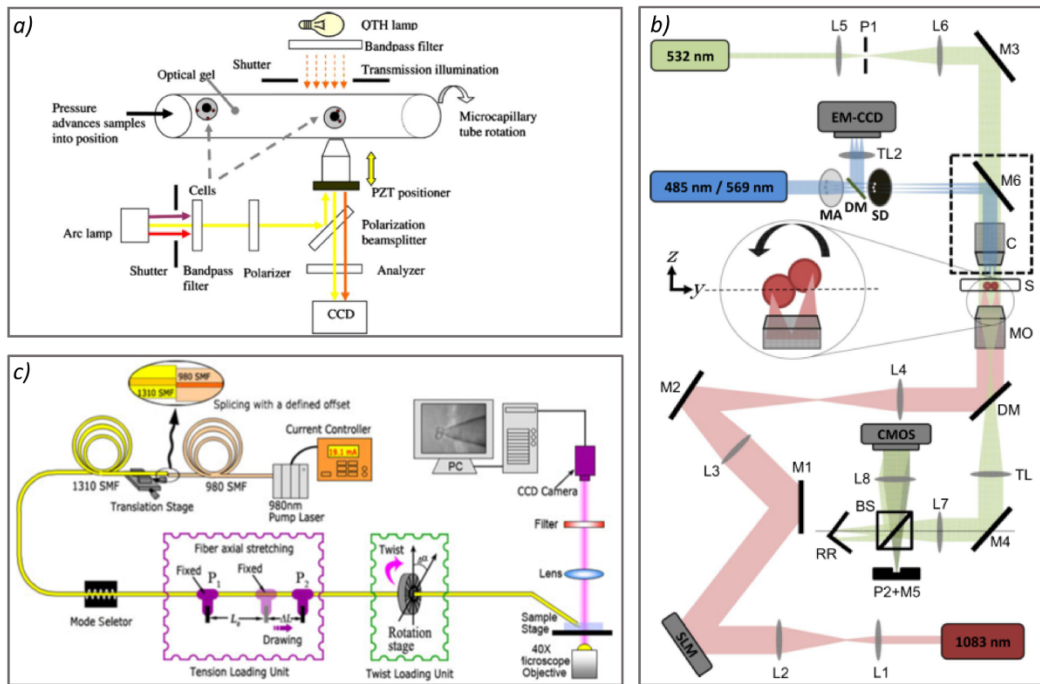


Figure 5-3: Various methods of sample rotation. a) Cells are wet fixed in an optical gel into a micro capillary. Therefore, rotating the micro capillary enables tomographical sample rotation. Schematic adapted from Miao *et al.*¹²³. b) Habaza *et al.*¹²⁶ present tomographic phase microscopy of yeast cells enabled by holographic optical tweezing. The beam path in red starting from the infrared laser on the bottom right corner becomes altered by an SLM so the optical tweezer is able to rotate the cells as shown in the close-up. Schematic adapted from Habaza *et al.* c) As previously discussed, splicing a SMF to a DMF offset can enable higher order mode propagation. This concept was used by Zhang *et al.*¹²⁷ to create a cell rotator using a tapered fibre acting as an optical tweezer, while selecting different modes using a mode selector and a rotation stage. The Tension Loading Unit calibrates the power in the two lobes of the dual lobe mode. Schematic adapted from by Zhang *et al.*

phase microscopy of yeast cells. The red beam path highlights the trapping signal which is altered by the spatial light modulator (SLM), the green beam provides interferometric phase microscopy, while the blue beam is used for spinning disk confocal microscopy. The SLM is the core piece that enables the rotation of yeast cells in Habaza's work. Magnified in the middle of Figure 5-3 b), the holographic trapping signal consists of two lobes that steer the sample by modulating the signal at the SLM. A rotation of two yeast cells could be achieved. Four orientations of the specimen are presented in the publication while a controlled stepwise orientation of 5° steps was discussed, data showing the accuracy of the steps was not shown in the document. The volumetric rendering shown, does not fully unveil this neither. In the publication of Zhang *et al.*¹²⁷ the method of cell-orientation uses two laser lobes as well but in a setup using laser fibre, therefore getting closer to the method of manipulation explored in this thesis. Figure 5-3 c) shows how Zhang *et al.* use a LP_{11} beam emanating from a tapered fibre, in order to create an optical tweezer near the end of the fibre. Together with mode selecting equipment, and an added rotation stage, twisting the fibre, Zhang *et al.* could align yeast cells in different orientations. A method that further led to sample rotation was already described in the background Section 4.1.4. To recall, photonic lanterns can

be used to create dual lobe modes, when tapered fibres are coupled into a multi mode fibre. This was used in a recent publication by Velázquez-Benítez¹¹⁰ to trap and orientate borosilicate beads. The data shows good alignment of the sample, although limited in the amount of possible orientations. Yet, a high number of orientations is needed for a detailed 3D reconstruction of the sample. After different examples of trapping and manipulating with one laser beam, the following passage will discuss the application of DBLTs and cell rotation. As the use of DBLTs for cell rotation is closely related and of particular interest to this project it is summarized in a separate Section.

5.1.2 Orienting living cells using dual beam laser traps

Dual beam laser traps consisting of two laser beams, trapping the specimen in their middle, were discussed in Section 2.1. Several techniques have been developed which use DBLTs to rotate living cells. One elegant approach without the necessity of further optics or electronics is the Optofluidic Cell Rotator (OFCR). It utilises a parabolic flow profile of liquid in microfluidics to exert a flow-rate-dependent torque on the cell. When applying a laminar flow field to the trapped sample, that is positioned in the middle of the optical trap, but lower than the microfluidic channel centre, the profile of the laminar flow that the cell experiences, bears a gradient as shown at the bottom of Figure 5–4a). The top part of the cell will be exposed to a higher flow velocity as it is closer to the centre of the capillary, where the flow is fastest, and the bottom half to a less rapid flow. This results in a torque which rotates the trapped cells. This kind of setup has already enabled 3D single cell tomography, as the rotation is perpendicular to the imaging axis (Kolb *et al.*¹²⁸). A downside of the optical flow rotator is that it constantly rotates the specimen in the laminar flow, thus for long acquisition times, motion blur may reduce the achievable resolution. Furthermore, because the liquid is required to flow over the cell, other cells or particles might pass the trapping area and interfere with the imaging or trapping. Another DBLT technique to rotate cells, known as the Fibre Optical Spanner¹²⁹, has been developed. It uses the observations of Prentiss *et al.*³⁵ that a torque is also present when the two laser fibres of a DBLT are slightly misaligned. Integrating fibres into a Polydimethylsiloxan (PDMS) chip and using pneumatic pads to manipulate the alignment of the fibres allows for controlled torques and rotation speeds as shown by Kolb *et al.*³⁶. In Figure 5–4 b) a schematic of the Optical Spanner is shown, with i) and ii) showing the red pressure pads relaxed and inflated and iii) and iv) showing the real device with its components highlighted with food dye. The rotation of the cell has also been achieved in a continuous fashion. Still,

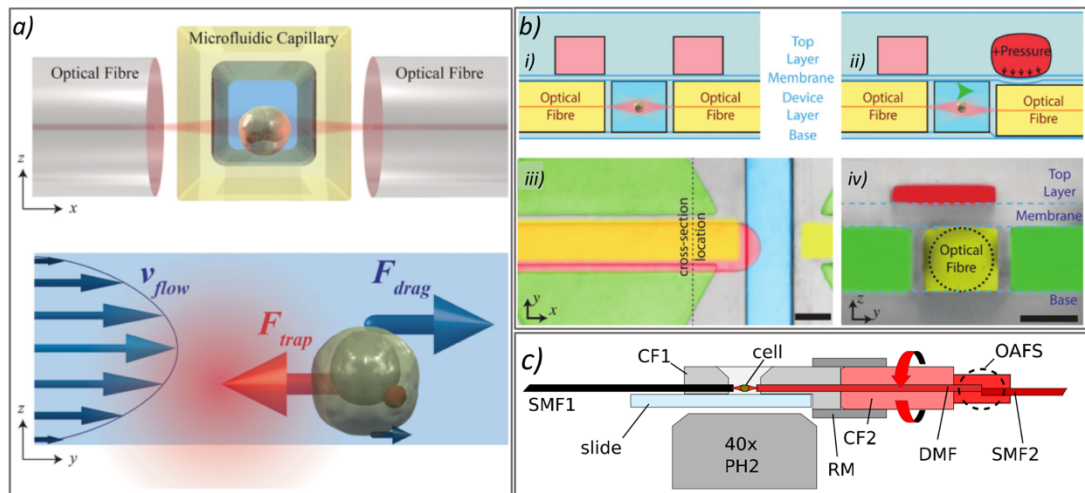


Figure 5-4: Principles of cell rotation using DBLTs. a) The principle of the optofluidic cell rotator. By trapping a cell off centre of the flow profile of a microfluidic channel forces can be induced. The drag of the liquid will push the cell away, while the trapping force pulls it back into the centre of the laser beam, this leads to rotational forces and the cell begins to rotate. Figure taken from Kolb et al.¹²⁸. b)i) By adding pressure pads (red) on top of a deformable PDMS dual beam laser trap the fibres could be vertically misaligned, as shown in ii). This misalignment caused a torque on the trapped cell and rotation. iii) shows the top view of the device with the integrated horizontal fibre pads that can be used to cause rotation in plane with the laser axis. In iv) the device is cut in half so that the perspective of a) and b) is rotated by 90° around the vertical axis. c) The cell rotator consisting of a dual beam laser trap with one of the beam arms containing a LP_{11} laser mode travelling in the dual mode fibre (DMF). The higher order mode is created by an offset splice from a single mode fibre onto a DMF. The whole right-hand beam arm of the trap can rotate. Figure by Kreysing et al.²⁰

a stepwise rotation of the cell would be preferred. As mentioned in the background Section 2.1.3, Kreysing *et al.*²⁰ realized a DBLT cell rotator by using the first higher order mode LP_{11} . The LP_{11} mode is ideal for aligning dielectric specimen that feature a slight asymmetry like cells. They broke the rotational symmetry of an ordinary Gaussian beam by splicing the single mode fibre of one trapping arm, offset to a DMF, enabling higher order mode propagation as discussed earlier in Section 4.4.1. The fibre that was used had a beat length in the scale of around 380 μm . The beat length is a measure of the distance the mode in question travels to gain an additional delay of 2π , which means that if the fibre end does not fulfil the condition of being a multiple of the beat length, another possibly undesired mode will be present at the fibre end. Thus, the dimensioning of the higher order mode bearing laser arm was picked carefully, so that the signal was kept clean. Rotating the specimen was realized by attaching the higher order mode containing beam arm to a rotation mount. The gyration of a red blood cell was successfully executed.

Yet, there are several drawbacks of this setup. Using macroscopic moveable parts in a setup dealing with few micrometre sized specimen is impractical, because the setup constantly misaligns itself, otherwise this method would have been used for 3D tomography. Furthermore, the shear movement of macroscopic parts easily induces leaks in the fluid containing trap. Coupling the LP_{11} mode signal into the trap at various

orientations via free space optics solved these problems partially. Kreysing *et al.*⁴⁷ optimised the optical cell rotator further by shaping the laser beam of one of the dual beam laser trap beam arms using a spatial light modulator. The Gaussian beam is spread across the whole area of the SLM via free space optics in order to create LP_{11} modes at different orientations to couple those back into the DMF for the cell orientation. The setup was briefly discussed in Section 4.1.3 and shown in Figure 4–1. But this setup is overly alignment extensive and the individual components, especially the SLM, very expensive. The higher order mode cell rotator (HOMCR), presented in this document, is a further step of innovation. It is all fibre based, less alignment-intensive and more reliable. In the next Section, it will be first discussed how the HOMCR is embedded in a stationary trapping setup. After this important step, the cell orientation results are presented.

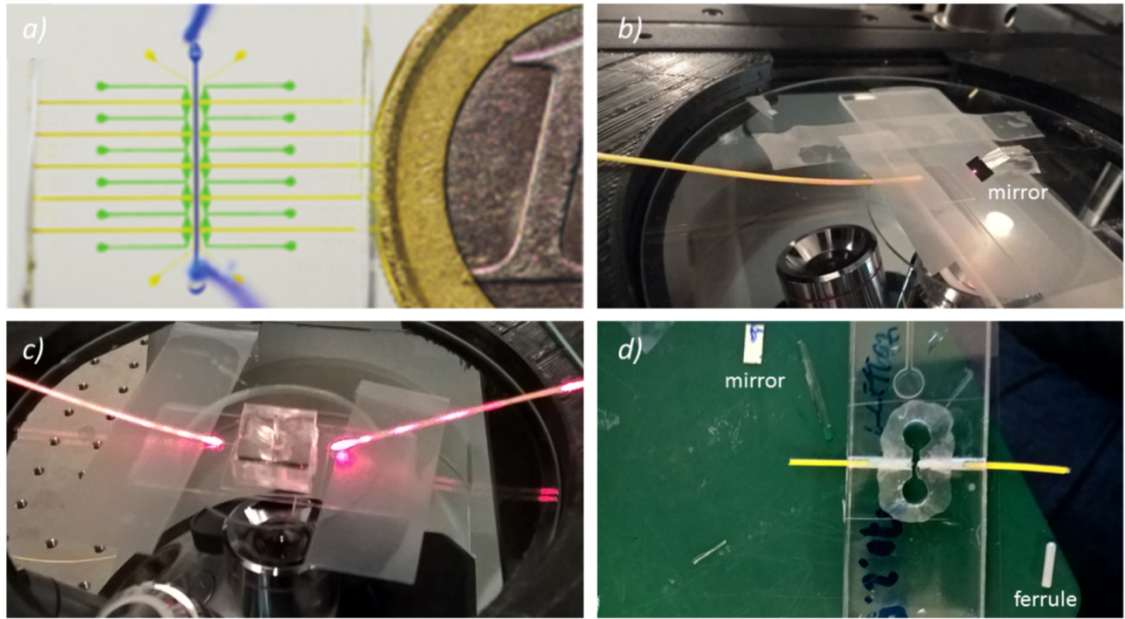


Figure 5-5: The three types of Dual Beam Laser Traps utilized in this piece of work are displayed. b) shows the concept of in-situ mode-calibration using a mirror. In more detail, a) shows a PDMS based trapping device similar to the one used in the publication “Dynamically reconfigurable fibre optical spanner”³⁶. In yellow the fibre channels for both beam arms, blue the main channel for insertion of cells in suspension and green the fibre pads to adjust the fibres if necessary. 1€ coin for scale. Picture taken with kind permission from Kolb et al.³⁶. b) shows how a manufactured mirror can deflect the light outside of the trap to calibrate the rotator in-situ. This can be used in an open trapping device. c) A open DBLT similar to a), but cut open via a scalpel to create space for open trapping and mirror calibration. d) shows an open trapping design using two ceramic ferrules and a laser cut PMMA top layer. The picture shows further the mirror in use for in-situ calibration and a ceramic ferrule.

5.2 INTEGRATION INTO A TRAPPING DEVICE

In order to be able to trap cells using the all-in-fibre higher order mode rotator, a dual-beam laser trap (DBLT) has to be constructed using two coaxially aligned fibres forming the laser trap, where one of the arms is a dual mode fibre guiding the LP_{11} modes used to align the biological specimen.

The device has a number of requirements which need to be fulfilled:

1. Accurate alignment of the fibres (R1)
2. Ease of loading of cell samples (R2)
3. No stress placed on the fibre which could alter to the mode pattern. (R3)
4. Compatible with high resolution imaging (R4)

There are also a number of features which would be beneficial, but not essential:

1. The ability to visualise the mode coming out of the fibre (B1)
2. No contact between the optical fibre and the sample (B2)
3. Option to use solvents to keep the setup clean & sterile (B3)
4. Capability to trap large multi-cellular object (B4)

5. Fast manufacturing (B5)
6. Low cost (B6)

As convenient loading of cells had to be provided, the first device of choice was a PDMS microfluidic chip that enabled the flushing of suspended mammalian cells into the device via syringes. Once a laboratory already facilitates PDMS manufacturing equipment, the creation of microfluidic devices is cheap and the benefits B2, B3, B5 and B6 are fulfilled, besides all the requirements. In the second type of devices, cell trapping devices with access from the top, in the following called open DBLTs, the sample can be pipetted in and out of the trap. This form of access bears advantages for using smaller sample sizes and further enables a very convenient in-situ mode calibration method, which we will discuss in Section 5.2.4. Benefits B1, B4, B5, B6 were fulfilled by the developed designs. Figure 5–5 displays the different DBLTs used in this piece of work. In a) the microfluidic PDMS chip is highlighted with the help of food die. In c) and d) the two open trap designs are displayed while b) indicates how in-situ mode calibration can be achieved in an open trapping device. The different concepts and their methods will be discussed in the following. As the methods were part of the development, they are not excluded from the main body of the transcript.

5.2.1 DBLT out of a PDMS microfluidic chip

Microfluidic devices have found a wide spectrum of applications¹³⁰. In Chapter 3 it was discussed how microfluidics can be embedded in a DBLT, the Optical Stretcher. But the bespoke design of a DBLT as presented for the optical stretcher is a time demanding pursuit. To combine the mode calibration and trap building seems hardly feasible, as the construction using a glass capillary is a lot more alignment intensive than inserting fibres into a PDMS chip. Faster methods to obtain a microfluidic DBLT have been developed for example in PDMS. A device fully manufactured in PDMS is presented in the following. PDMS, as it is deformable, enables the channels to be of smaller height than the fibres, this results in the two fibres being well aligned and held in place by the elastic walls. PDMS lowers the cost and allows for sophisticated construction details, such as pressure pads (see Kolb *et al.*³⁶). As seen in Figure 5–5 a), the microfluidic channel that will guide the sample is highlighted in blue. To allow easier insertion of the two coaxial fibre arms, the fibre channels are all connected and open to the outside. This ensures that inserting the fibre is not counteracted by pressure building up inside the cavity, when pushing the fibre further into the PDMS device, as the walls provide a tight closure. The fibre channels can further be filled with liquid, such as non-cured-

PDMS, to enable fibre insertion with lower friction and provide refractive index matching between the fibre and the PDMS channel wall which reduced Fresnel reflection loss, divergence of the beam and aberrations of the mode.

Following the results of Section 4.4.7 showing the repeatability of selected modes, the generation of LP_{11} modes at the desired angles has to also function after the fibre is inserted into the trapping device. As the higher order modes are sensitive to external stress, the walls of the device may negatively influence the mode pattern, and to verify this, the LP_{11} mode has been measured in the far field after insertion into a PDMS device. To remove any scattering from the channels associated with the 2nd fibre of the trap, a PDMS device was cut in half along the microfluidic channel with a DMF inserted. The optical fibre and the wall next to it are visible in Figure 5–6 a) while Figure 5–6 b) shows the cross-sectional view of the fibre within the channel. The PDMS around the fibre displays marks due to the deformation of the walls as the fibre is 20 μm higher than the fibre channel. This stress of the PDMS bulk could transfer into the core of the fibre and modify the resulting mode. Figure 5–6c) shows the successful reproduction of several chosen LP_{11} modes. The signal on the NIR Detector Card (Thorlabs, Germany) shows that the LP_{11} mode could be re-obtained, guiding towards the trapping experiments presented in Section 5.3.1.

5.2.2 PDMS chip manufacture & mode calibration

The PDMS DBLT devices used consist of a top and bottom layer (the third pressure pad layer of Kolb *et al.*³⁶ was not implemented) both manufactured from PDMS mixed in a 10:1 elastomer to curing agent ratio (Syl-Guard 185). The channel structures in the top layer were created by pouring liquid PDMS onto a SU8-2025 (Microchem Inc.) master mould, where the SU8 is photolithographically patterned on top of a silicon wafer formed the positive to create the channels. This allows many identical devices to be produced from the same mould, decreasing production time and increasing repeatability. After degassing air bubbles out of the liquid device's top layers in a desiccator, it was hardened in an oven at 65 °C for at least 3 hours. The flat, unstructured bottom layer, also consisting of PDMS, was poured into a Petri dish using the calculated PDMS volume to create thin layers of approximately 230 μm and degassed and baked in the same manner. After both layers have been hardened they were cut out and cleaned using Scotch Magic TapeTM (3M, US) removing any dirt and dust particles from the surface. To bond the two layers together, creating a closed channel structure, a plasma oxidiser (Diener) was used. The surfaces to be bonded were exposed to an air plasma

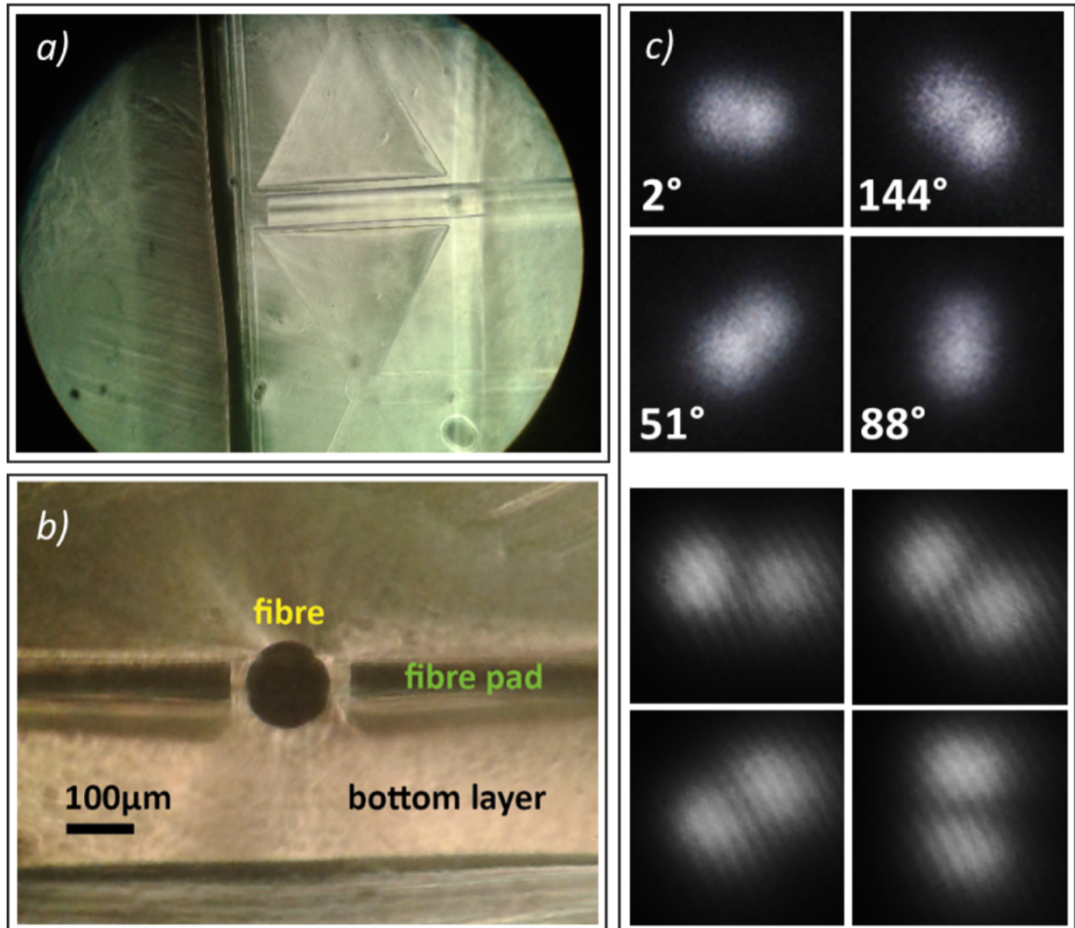


Figure 5-6: a) A PDMS based trapping device cut in half with fibre inserted. b) The device as shown in a), but imaged from the left facing the fibre end. The fibre is around $125\mu\text{m}$ wide and while the bottom layer measures $230\mu\text{m}$ the height of the fibre pad chambers was approximately $105\mu\text{m}$. c) The mode signal could be reproduced after fibre insertion compared to its initial mode calibration. Four different orientations are displayed. The selected mode signals before the reproduction are displayed below.

and then pressed into contact as soon as possible. To further aid the bonding process, the completed devices were baked again for 3h in the $65\text{ }^\circ\text{C}$ oven. To assemble a DBLT, the devices had to be bonded fully before the optical fibres were inserted. Liquid PDMS without curing agent was inserted into the fibre channels, via applying a drop of PDMS to the edge of the device where the optical fibre channel located and then placing the chip into a vacuum chamber. Because of the gas permeable nature of the solid PDMS, the liquid PDMS was drawn into the channels enabling friction-reduced fibre insertion. Furthermore, the liquid PDMS more closely matches the refractive index of the PDMS walls reducing the Fresnel reflections and increasing the light reaching the centre of the trap.

Before the trap was finished in its construction via inserting both fibres, the piezo voltages to create the set of LP_{11} modes for cell alignment had to be calibrated with the fibre in a position very similar to its final one. If the calibration was carried out in a very different position, the changes in stresses when the fibre is inserted into the device may

change the resulting mode patterns. For this, a rack was constructed using optomechanics (Thorlabs, UK) guiding the DMF, as the fibre signal could not be imaged directly at the microscope's stage due to the large dimensions of the camera. The rack enabled moving the whole microscope and calibrating the laser mode, while the fibre was kept in the same alignment. After calibration, the microscope was moved back in place and the dual beam light trap was carefully assembled.

5.2.3 Two ways to open dual beam laser trap devices

Three main motivations were underlying the construction of the open DBLTs:

- 1) The ability to trap large multicellular objects was restricted dependent on the microfluidic channel size in the PDMS chips. The dimensions of the microfluidic channel hardly provide a one-size-fits-all samples channel, while an open DBLT faces no constraints.
- 2) Moreover, a microfluidic design generally facilitates a large dead volume of liquid inside the tubings and channel, this leads to a necessity of larger quantities of sample. Due to the open access from the top in an open DBLT, singular sample could be placed directly inside the trapping area, for example via micropipette aspiration.
- 3) The option to calibrate the aligning mode signal *in-situ* inside a fully built trap. Calibrating the HOMCR without moving any major parts of the setup (as previously the microscope) could be achieved by reflecting the laser signal out of the trap by placing a small mirror into the beam path to reflect the trapping signal into the camera.

However, the microfluidic devices described before had an enclosed microfluidic channel, limiting access to the beam path. To place the mirror in the beam path, open trap designs had to be considered. Secondly, the goal to trap bigger biological specimen such as cell clusters was set as an emerging exciting application. An open trapping design has less size limitations compared to trapping devices using microfluidic channels. On the other hand, the downsides of an open setup are collecting dust and dirt in the trap especially on the laser fibres, and as the sample loading differs, a significantly lower sample throughput. Such a setup is also more likely to trap random particles in the laser beam as turbulent flow can be present, while in a microfluidic device the flow is laminar.

Two distinct designs were used to obtain a dual beam laser trap. The first type of trapping device was directly derived from the PDMS designs described in Section 5.2.1. With the main difference that the devices were cut open via scalpel (see Figure 5–7).

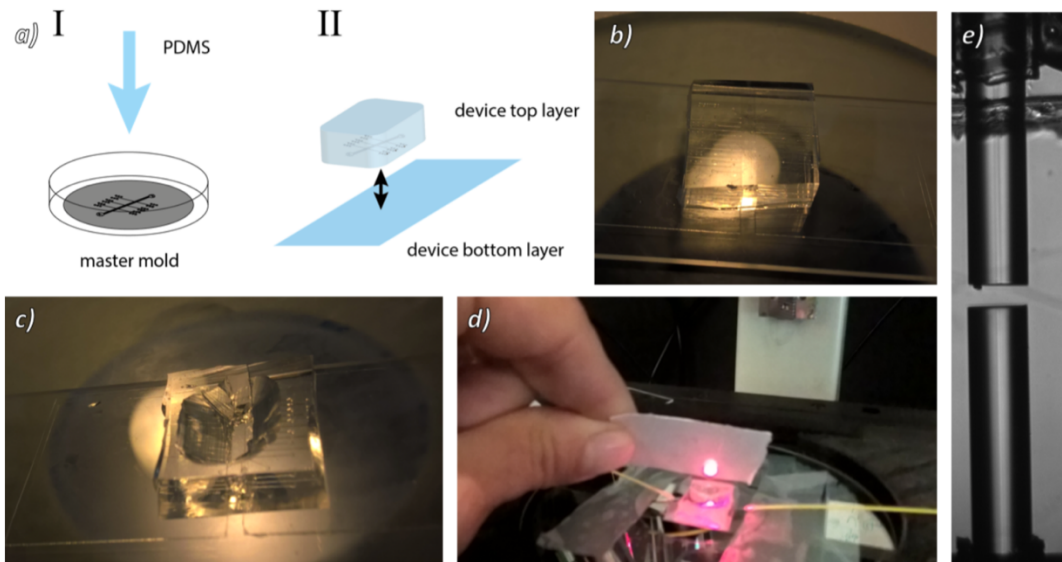


Figure 5–7: From manufacturing a PDMS based DBLT to an in-situ mode calibration enabled HOMCR. a) A master mould is obtained using photo lithography. Liquid PDMS is poured into the Petri dish to get the top layer of the PDMS device (Step I). By plasma bonding the PDMS top layer to the devices bottom layer a complete PDMS chip is acquired. The potential bottom layers are either a thin PDMS layer or directly a glass slide/coverslip. b) shows a PDMS chip bonded onto two square coverslips with a groove in between them. c) cutting out the microfluidic channel using a scalpel enables open access to the trap and further in-situ mode calibration. The cut-out part is angled to help the thin Aluminium mirror (see also Figure 5–10) to sit in the device approximately angled 45° for optimum mode calibration. d) The in-situ mode calibration is ready to be used. For alignment of the mirror and later the CCD camera, the red laser pointer is employed. The CCD camera will be placed above and the scan through the set PCD voltages can occur before the selecting the modes to manipulate the cells. e) The cut out area is 950 μm in width while the fibres are 45 μm apart their centre was 1 μm misaligned.

The second trapping setup contained two ceramic ferrules aligned by an inserted laser fibre that were mounted on a coverslip and combined with a PMMA top layer to form a DBLT (see Figure 5–8).

5.2.3.1 Open PDMS DBLT manufacturing

In a direct approach, an open DBLT could be created from PDMS fibre pad devices, via removing a Section out of the chip with a scalpel, see Figure 5–7 for illustration. While the PDMS top layer and bottom layer were manufactured as described in Section 5.2.2, the microfluidic channel was cut out using a scalpel. The cut-out was approximately 5mm in length and 1mm in width. To accommodate and align a thin mirror for the mode calibration, the scalpel was then adjusted to cut around that rectangle in a 45° angle creating a slope, where the mirror will lean against similar to Figure 5–7 c). Cutting had to be carefully executed, as shearing the bulk of PDMS plastically will lead to misalignment of the fibres. Both fibres were inserted using ethanol in 70% concentration serving as a lubricant to lower the fibre insertion-related friction. Ethanol is absorbed into the PDMS and expanded the overall structure which helped with the insertion. Whilst acting as a lubricant Ethanol evaporates quickly (evaporation could be

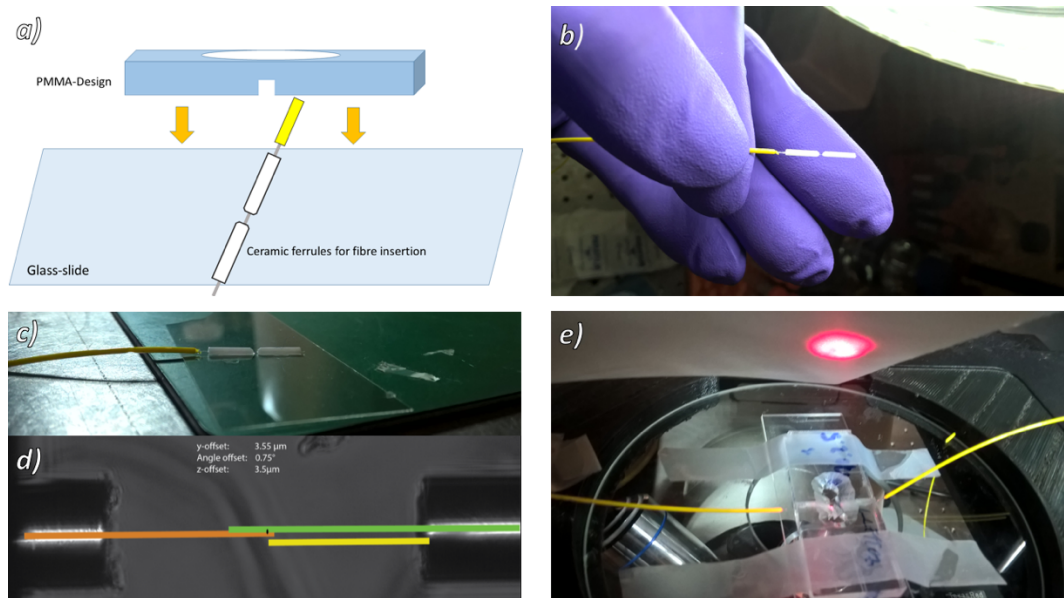


Figure 5–8: The process of building an open ferrule trap. **a)** Using two via fibre insertion aligned ferrules secured on a coverslip and a PMMA laser cut top part can form a DBLT. **b)** First a long piece of stripped fibre (~2cm) was inserted in the two ceramic ferrules. After, the two ferrules were glued down to a coverslip or glass slide using Covergrip (Biotium, USA), keeping the aligning fibre inserted. This aligned the two ferrules coaxially. **d).** **e)** The laser cut PMMA top part was secured using PDMS to form a basin for the open DBLT. The whole setup could facilitate the custom built mirror for *in-situ* characterisation.

further sped up using compressed air to blow dry the device). Additionally, the ethanol cleaned device and fibres. It is of high importance to recall that ethanol, even when diluted, is highly flammable, therefore, it has to be completely evaporated before the laser was used to not cause burning of the device. When both fibres are inserted, the newly formed DBLT has to be checked for alignment. Misalignment of the two trapping fibres induces additional sample movement or, in heavy misalignment, no trapping at all. This was discussed in the introductory Section 2.1.2, relating to the pioneering work by Constable³⁵. In Figure 5–7 e) an open PDMS DBLT is shown. To make the alignment better visible, the fibres have been moved close together, the normal trapping distance is more than twice this width. The misalignment of the two fibres measured in the middle of the trap is 1 μm, over a fibre distance of 45 μm. Extrapolated over 4 different traps the accuracy of alignment was $3 \pm 0.4\%$ per width of 100 μm. If the trap is sufficiently aligned, the right hand fibre will be pulled back, to allow placing the Al-mirror for *in-situ* mode calibration. The placement and arrangement of the *in-situ* mirror into a PDMS based trap can be tedious, as the design does not allow for much space outside the trapping area, to keep the dead volume as low as possible. The available room for adjustment is therefore small. The mirror should be angled at approximately 45° for optimum performance. PDMS to glass has a high friction coefficient, which can work against fine adjusting the mirror relative to the DMF, as small movements are suppressed by the high friction.

5.2.3.2 *Open-ferrule DBLT manufacturing*

To overcome the shortcomings of the PDMS based open DBLT, a more rigid setup was explored. Ceramic ferrules are cylindrical tubes designed and manufactured to hold and align the two optical fibres within a connector, with minimal loss. Therefore, they were investigated for other alignment tasks such as the trap building. As the inside of such a ferrule is 126 μm in diameter and the outer dimensions of the laser fibres in use is 125 μm , it thought to be possible to align two ferrules accurately by inserting the highly rigid fibre through them both, facing each other coaxially. The aligned pair of ferrules was later glued down on a coverslip. Figure 5–8 shows this process from the aligning two ferrules to realisation of a working DBLT, that provided the option to calibrate the mode signal *in-situ*. **a)** gives an overview of the whole process. **b)** shows the first step in the manufacturing process, the insertion of a glass fibre via tweezer for the alignment of two ceramic ferrules. **c)** the fibre with the two ferrules was gently placed on the coverslip, without creating any shearing forces or allowing the ferrules slide closer towards each other. This maintained a suitable gap for the trapping area. The ceramic ferrules were secured using a coverslip sealant (Covergrip, Biotium, USA) as it provides strong bonding for glass to glass surfaces. In the last steps towards the DBLT, firstly a laser-cut PMMA design containing grooves for the ferrules and a pool for the loading of cells was manufactured using a laser cutter (Epilog Laser mini, USA). Secondly, the PMMA designs were polished with a grinder, to house mirrors for *in-situ* calibration at a slope of 45°. Thirdly, the prepared PMMA design was attached on the top of the coverslip, with the two grooves aligned on top of the ferrules and secured using half-cured PDMS that was later solidified on a hot plate (**e**). It is advisable to leave two fibres inserted from both sides into the fixed ferrules to stop the creeping of liquid PDMS inside the ferrules, as this can create blockage against fibre insertion and making the device unusable. When 4 different traps, built with this concept, were measured for alignment, the average deviation of fibre alignment perpendicular to the fibres and compared to the distance between both fibres was $1.8 \pm 0.67\%$. Compared to the distance between the ferrules this resulted in $0.9 \pm 0.31\%$. One of the traps was an outlier being 4.1% off, pulling the average up, regarding the fibre alignment. While the PDMS-based traps could be flushed using ethanol, which is very convenient in order to keep the traps clean and sterile, the glue used to attach the ferrules to the coverslip prevented this in the open-ferrule DBLTs. In the present configuration ethanol dissolved the sealant. The surfactant sodium dodecyl sulphate (SDS) (concentration of

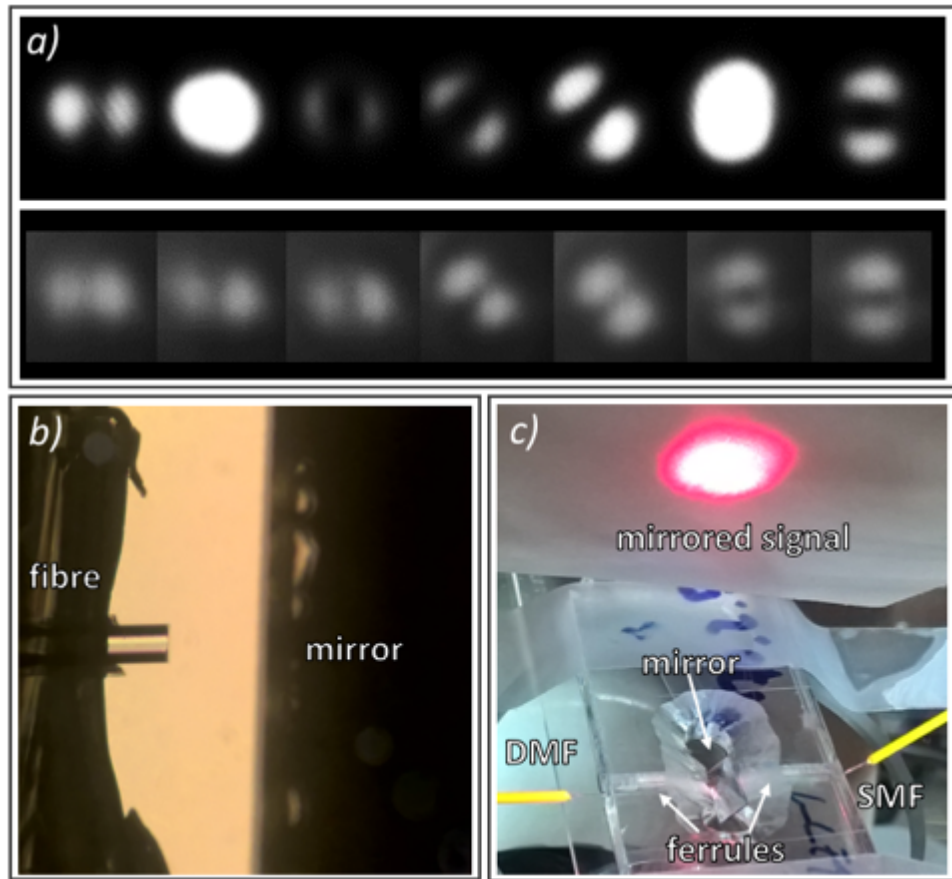


Figure 5–9: In-situ mode calibration using a custom built mirror. a) Top row: Various examples of LP_{11} modes acquired through reflecting the laser light of the dual mode fibre from a coverslip into the microscope. Inspecting the intensity, the differences in intensity caused by polarisation dependent optics are obvious. Bottom row: For comparison LP_{11} modes acquired with direct imaging using a custom built mirror reflecting into a CCD camera. b) shows the mirror inserted in the trap for in-situ mode calibration inside an open-PDMS DBLT. c) In an open-ferrule DBLT an inserted mirror reflected the signal upwards. Shown for the red laser instead of the infrared that is used for trapping. In normal operation the CCD camera was placed centrally over the trap to capture the reflected signal.

crystalline SDS solved in distilled water 5g/100ml) was used instead of a solvent to keep the devices clean.

5.2.4 In-situ mode calibration

The LP_{11} signal is sensitive to phase changes due to bends in the fibre and stress. It was shown in Section 5.2.2 that sufficient caution, when building the trap can lead to an unchanged mode signal and thus successful use of the all-in-fibre HOMCR. Yet, the calibration alignment used, described previously in Section 5.2.2, involved the moving of the whole microscope. This was difficult as it had to mimic the fibre position later in the trap very precisely. When calibrating laser modes for the HOMCR, the microscope stage and the size of the CCD camera did not allow for keeping the microscope in the same position as in the cell trapping experiment. Thus, because the CCD camera did not fit on the stage, the whole microscope had to be moved out of way while keeping

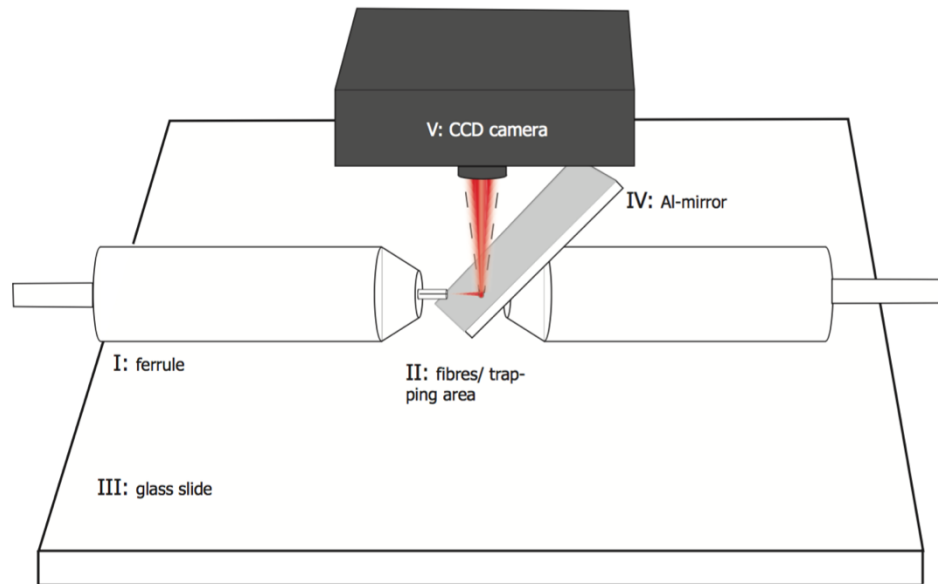


Figure 5–10: Schematic showing the in-situ mode calibration using an E-beam coated Aluminium mirror in an open-ferrule DBLT. The approximately 4x6mm big mirror is placed into the trap via tweezers. The CCD-camera is placed above the trap to capture the signal alternated by the PCD.

the fibre position approximately stationary. Over time in the laboratory, parts of the setup can be moved either on purpose or accidentally. Once a trapping device is built, it is rather unwanted to disassemble it for recalibration of the mode signal, as often under the reinsertion of fibres into the trapping device they keep braking, or dirt finds its way into the fibre channels. A method of measuring the signal in-situ, inside an assembled DBLT is hence presented. The most direct way to reflect the mode signal from the fibre facet into a camera was by using a coverslip in front of the fibre angled approximately 45° . Considering the refractive index difference of air and borosilicate glass¹³¹ and solving the Fresnel equations, the glass reflects approximately 9% of S-polarised light downwards into the microscope itself, 1% P-polarised.

From Figure 5–9 a) a clear mode signal is revealed, however the measured intensity varies strongly with the mode angle. This is consistent with the polarisation of the mode rotating with the mode angle, and the polarisation dependent reflection coefficient of a Fresnel reflection due to the changing refractive index. Therefore, the information of the actual signal that was present, when the signal was leaving the fibre was modulated by the glass mirror.

The lower row of Figure 5–9 a) shows the signal acquired with a custom-built mirror that overcomes those deficiencies. Here, the mirror was angled to reflect the beam upwards, instead of downwards into the microscope, to guide the light into a CCD camera (Basler, Germany). While the reflectance of the Borosilicate was below 9%, the custom built Aluminium mirrors provide a reflectance of 95% for the infrared light. It

deviates in the order of a few percent (around an incident angle of $\sim 45^\circ$) for S and P polarised light and was seen as negligible. This is a significant improvement over the glass mirror.

The workflow compared to the PDMS chip was improved as the *in-situ* calibration took place after the trap was built, in contrast to the microfluidic traps where building the trap often made the re-calibration and thus also the re-construction of the trap necessary. A schematic of the *in-situ* mode characterisation for an open-ferrule DBLT can be seen in Figure 5–10. As the mirror is $130\ \mu\text{m}$ thick and angled 45° , this added a necessary height of $\frac{1}{\sqrt{2}} \times 130\ \mu\text{m}$ to the centre of the trap being built. This results in a necessary trap height greater than $92\ \mu\text{m}$, which is $31\ \mu\text{m}$ on top of the ordinary trap height of half the fibre ($62.5\ \mu\text{m}$). Elevating the trap height was only necessary for the open PDMS devices as the trap height in the open ferrule DBLTs measured $625\ \mu\text{m}$, half a ferrule diameter. In the open PDMS DBLTs the trap height was adjusted by adding a thin (approximately $150\ \mu\text{m}$) PDMS bottom layer. The manufacturing details of the E-beam coated Aluminium mirrors can be read in the below, in the next Section. Overall the mirrors performed better with less aberrations and interference fringes as the calibrations using free space optics presented in Section 4.3 (page 55). Yet, there might have been a slow occurring oxidation and therefore degradation of the mirrors over time, despite a protective Silicon-Dioxide film was deposited on the mirrors. In the following, the open DBLT devices are presented that are necessary to enable *in-situ* mode calibration.

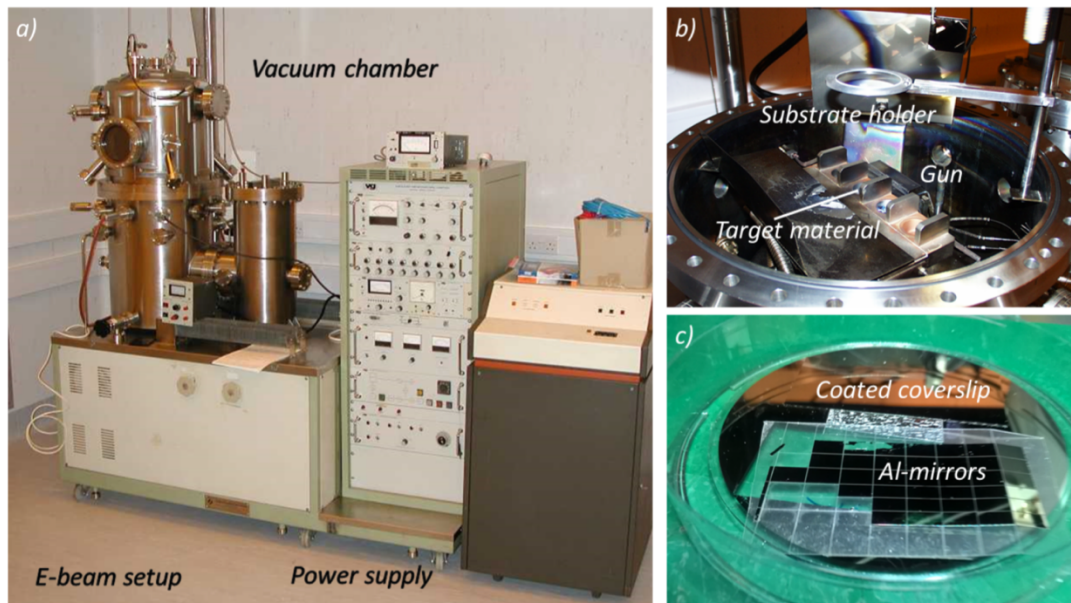


Figure 5–11: Mirror manufacturing via e-beam evaporation. a) The complete e-beam evaporation setup. The chamber has to be completely evacuated as air would react with the electron beam or vapour of the target material. b) The inside of the vacuum chamber is shown with the substrate holder on top. The electron gun is not visible. While the electron beam gets deflected by magnets in a circular path to hit the target material, in this specific case Aluminium. c) Two coverslips were initially attached to a silicon wafer to then be mounted upside down at the substrate holder. The e-beam gun evaporates the Aluminium underneath and the wafer along with the coverslips are coated. Further one of the coverslips is presented cut into small mirrors.

5.2.5 Thin mirror deposition

Investigating materials that are not particularly polarisation selective under reflection like gold, silver or aluminium lead to the choice of Aluminium that provides ideal properties of 90% reflectivity in the infrared wavelength. For optimum reflection properties thin mirrors of 130 μm thickness were custom manufactured in house. Substrate coverslips were used and e-beam coated with a layer of approximately 100 nm Aluminium plus an additional layer of silicon-dioxide (up to 10nm) to protect against corrosion. As the protective coating is essentially glass, the reader will get reminded of the previously discussed reflection properties of it but as the coating is significantly smaller than a wavelength (1064 nm) of the signal the polarising effects can be neglected. Later the coated coverslips were cut into smaller pieces of roughly 4x6 mm, using an Automated Dicing Saw (Disco, Japan), that fit into the open DBLT devices constructed.

5.2.6 Cell culture

The used K562 cells were cultivated at a CO_2 level of 5%, 95% relative humidity and a temperature of 37°C in house. The culture medium consisted of Advanced RPMI 1640 Medium (Thermo Fisher), containing an added content of 10% foetal bovine serum (FBS), 4mM L-glutamine and 1% Pen-Strep. The cells were split at a concentration of

around 10^6 /ml. In order to obtain easy to use test-specimen K562 cells were fixed in 10% Formaldehyde, washed and kept refrigerated.

5.2.7 Data acquisition

The trapping and rotation of cellular sample was acquired using an inverted microscope (Motic AE31) equipped with a 40x/0.6NA objective (Motic). The imaging data was captured via a charged-couple device camera (CCD) (AVT Mako) and saved at 20fps in the AVI format. By building a Labview program (National Instruments), the full description of applied voltage at the PCD leading to mode and sample orientation could be saved as string in each AVI frame. The videos were stabilised post imaging via tracking the centre of mass of each frame, using a custom built Labview program.

5.2.8 Object tracking

After stabilising the frames of the AVI file the rotation can be mapped if trackable objects like cellular organelles are found. In Section 5.4 three bright organelles were found. By applying a linear region of interest (ROI) across the cellular specimen the projection of these bright spots was followed during the rotation. As the spots were the brightest objects the peak in the intensity profile of the pixels along the ROI measures their position accurately. By measuring the maximum and minimum displacement along the ROI the angular excursion can be calibrated. Using euclidic trigonometry the sample's orientation is mapped leading to the data of a 540° stepwise rotated K562 cell presented in Figure 5–15.

5.3 RESULTS

After the engineering of the several designs they were tested for trapping and rotation of cellular sample. First the PDMS chip was employed, as the designs were ready to find the way into manufacturing. Subsequently the two open DBLTs were established.

5.3.1 Rotating in a PDMS chip

The sample consisting of K562 human immortalised leukaemia cells was loaded via a syringe. The microfluidic channel width measured $100\mu\text{m}$, while the PDMS walls were each $30\mu\text{m}$ wide, resulting in a beam diameter of approx. $24.7\mu\text{m}$ at the centre of the trap. With this setup it was possible to trap a two cell cluster (see Figure 5–12). Before the trap was assembled, the laser modes were selected and reproduced stepwise in the range from 0° to 180° . Then, the trap was completed via fibre insertion. The selected modes corresponding to the displayed cell rotation are shown in the centre of the Figure

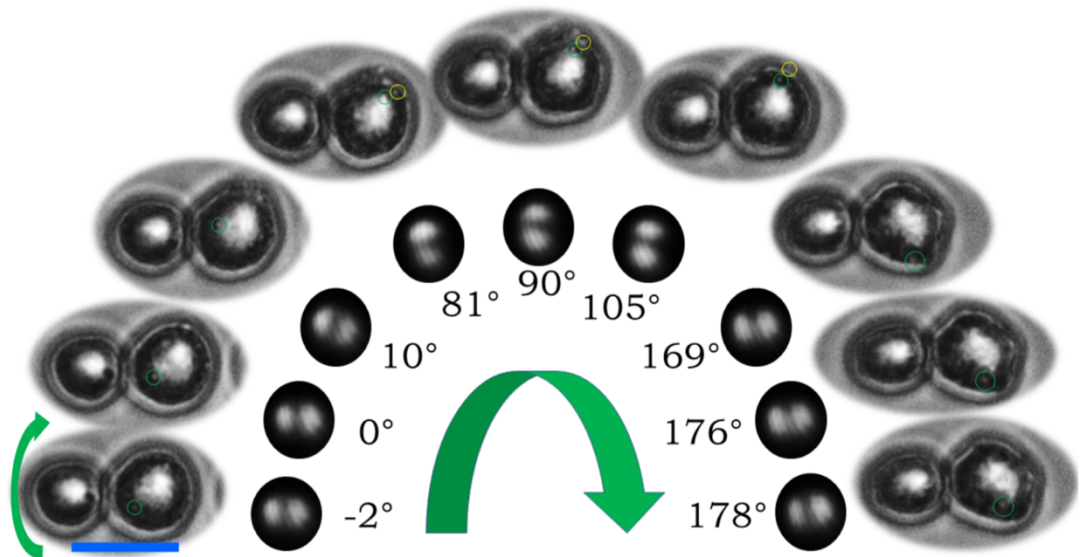


Figure 5–12: A cell cluster of two cells trapped in a rotating DBLT, the HOMCR. The rotation of the mode signal was clockwise indicated by the big green arrow in the middle. The calibrated mode signal is displayed. The rotational direction of the two cells is shown by the green arrow on the left. Tracked spots further indicate the cells movement, highlighted in green and yellow. For each the horizontal, vertical and 180° rotated orientation of the signal and the cells three examples are displayed. Scale bar 10 μ m.

5–12, while the direction of rotation captured by the CCD camera was clockwise as indicated by the green arrow. Meaning the cell, regarding the facet of the DMF left of it, turned anti-clockwise. As the images were acquired by an inverted microscope, the cell was imaged from underneath, so this sense of rotation can be understood.

Figure 5–12 shows excerpts of the rotation with spots highlighted in green and yellow, to aid following the rotation. While the different visible trackable objects could not be followed for the entire rotation, the general outline of the larger cell on the right does show a definite change. Converting the imaging into data of more descriptive depth was not achieved as the visible features could not be tracked over enough distance to make valid assumptions about the maximum displacement and thus radius of rotation of the respective spot. Yet, this was achieved in Section 5.4 where three bright spots could be imaged around the whole rotation leading to interesting data classifying the HOMCR presented in Figure 5–15.

5.3.1.1 Discussion & Conclusion

Forming a DBLT using a PDMS chip was a direct approach to transfer the HOMCR into a microfluidic environment. While first data of a trapped and by the HOMCR oriented two cell cluster was shown in Figure 5–12, the rotation of the specimen could not be sufficiently characterised. It was shown in Section 5.2.2, Figure 5–6 respectively, that LP_{11} modes for sample alignment have to be calibrated before trap building. This is problematic as the assembly of the trap via fibre insertion can either

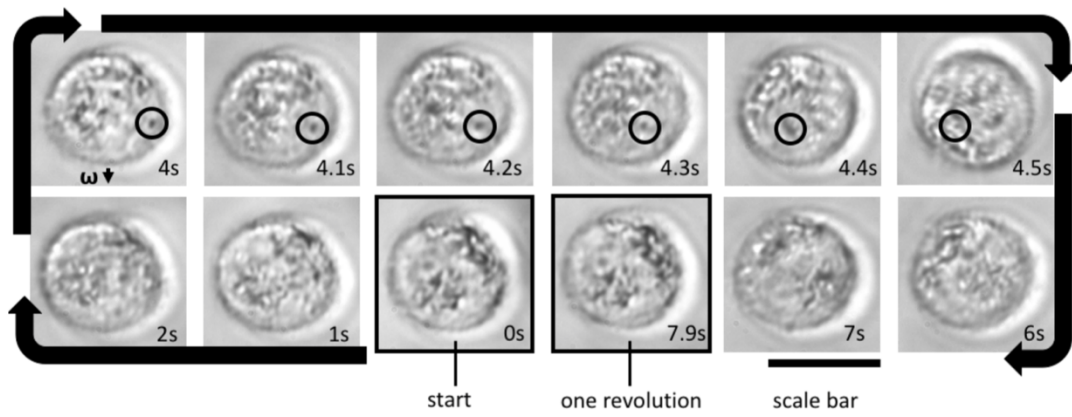


Figure 5–13: Misaligned fibres lead to an Optical Spanner. The two fibres in the open-PDMS DBLT are misaligned and the resulting inequality of optical forces leads to the spinning of the trapped K562 cell with a 20 μm diameter. Starting at 0s and following the pictures clockwise one revolution can be observed. The top row shows frames that are shorter apart from the next one in time to enable tracking a dark spot inside the cell as it moves across from 4s to 4.5s. A full revolution takes nearly 8s. The scale bar measures 10 μm .

lead to differing fibre bends or fibre breaks and a cut back and reinsertion is required, which thus also demands entire recalibration of the system. This shortcoming led to the development of open trapping designs, capable of in-place mode calibration via a small mirror. The fabrication of two capable open trapping devices and of the small calibration mirror were discussed above in the methods Sections 5.2.3 and 5.2.5 respectively. The in-place calibration, further referred to as *in-situ* mode calibration was discussed in the next Section (Section 5.2.4). Therefore, the trapping capabilities of the newly developed open dual beam laser traps (open DBLTs), that can facilitate the *in-situ* mode calibration mirrors, will be discussed in the following Section 5.3.2.

5.3.2 Trapping in open dual beam laser traps

The DBLTs under investigation providing *in-situ* mode calibration were briefly shown in the overview Figure 5–5. The simplest approach to an open trapping device was to cut the top part of the previously discussed PDMS fibre trap open and shape it to the new needs of facilitating a thin mirror and the ability of trapping larger objects. The second trap design employed a newly developed low cost method of building a DBLT consisting of two ceramic ferrules, a coverslip and a PMMA top layer. Both types of devices allow open access via pipettes or tweezers from above. Not only was the open access useful to dispense samples, but it gave rise to the concept of *in-situ* mode characterisation using a small mirror. This is more convenient than calibrating before trap building while moving large pieces of equipment, like the microscope. The alignment of the fibres could be tested after calibrating and before the actual trapping experiment.

Both open DBLT devices were tested and verified in their applicability for cell trapping. Before loading sample via pipetting, the trap was filled with phosphoric buffered saline (PBS). The approximate cell concentration after pipetting was $10^4 \frac{\text{cells}}{\text{ml}}$. Different cell types could be trapped in the devices, such as the immortalised myelogenous leukaemia cell line K562, the human primary glioblastoma cell line U87 and an immortalized commercially available cholangiocarcinoma liver cell line HepaRGTM. As the structural composition of the former PDMS chip is heavily altered by cutting out the open trap, alignment of the trap is not guaranteed and even slightest misalignment can cause the sample to not trap stably. The trapped specimen does not necessary drop out of the trap, but an imbalance of forces can cause the sample to rotate or move in unwanted manner. Figure 5–13 shows how slight misalignment of the two fibres inside an open PDMS DBLT can cause gyration of a trapped K562 cell, a concept that was previously used to advantage for cell rotation, under the term Fibre-Optic-Spanner¹²⁹(discussed in 5.1.2). Yet, in order to prove the working principle of the HOMCR no additional rotational forces, besides the change of orientation of the higher order mode signal, are wanted.

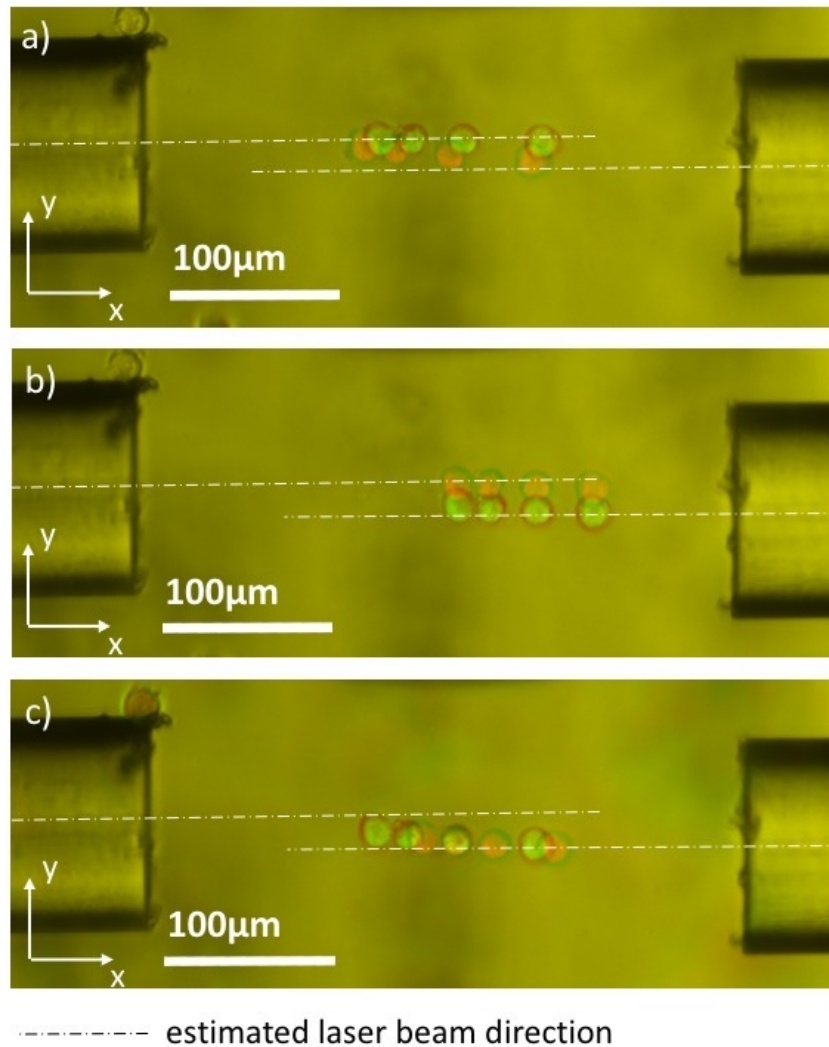


Figure 5–14: Fibre misalignment can cause trapped sample to alternate between semi-stable trapping positions. Four U87 glioblastoma cells were trapped inside an open PDMS DBLT. The fibre misalignment is indicated by dashed lines. The three images show a red/green overlay of two different time frames, with red signifying the prior frame. In a) the frames (red/green) were 0.7s, in b) 0.6s and in c) 7.4s apart. Further, the images a) and b) were separated in time by 2.9s, b) and c) 2.4s. Starting from the red image in a) the cells were trapped by both beams nearly evenly, with slight bias to the right hand beam. The green overlay shows how 0.7s later they got pulled into the left-hand beam (L). As they align predominantly in the L beam, more scattering force arrives from the left than right, therefore 2.9s later in image b) the cells have travelled to the right. They travelled close enough to the right-hand fibre R that the optical forces of R start to dominate and the gradient force of R pulls the cells (red) 0.6s later into the beam axis of R (green). 2.4s later in c) it is observable how the four cells found their way into the middle between the two fibres. The optical forces of the two fibres were more equal in the centre of the trap, so movement is slower. It took the cells 7.4s to travel from the positions marked in red to the ones in green. Comparing this to the starting positions (red) in a) the four cells arrived approximately at the same spots again. The measured offset causing this behaviour was $23\mu\text{m}$ over a trap width of $361\mu\text{m}$. The angle between the fibres was 2° off from being co-linear.

Optical spanner movement can be inspected, the K562 cell shown in Figure 5–13 completes one revolution in approximately 8s. The direction of movement can be observed in the top row by tracking a single spot inside the cell from 4s to 4.5s. The spot moved from right to left, so the rotational direction of the cell was perpendicular to the trapping axis, indicated by a small arrow, alongside with the oscillatory frequency ω

(frame at 4s). Such rotational axis indicates a fibre misalignment in the z-direction, perpendicular to the imaging plane. A more complex movement pattern, resulting of fibre misalignment, can be further observed in Figure 5–14 (above). Four U87 cells were trapped inside an open-ferrule DBLT. This time the fibres were even more misaligned and visibly in the y-direction. The estimated beam direction is overlaid and the offset was measured to be $23\mu\text{m}$ while the angle of the two fibres differed by 2° from co-linearity. To highlight the movement of the four trapped cells, three overlays of two time-steps each are presented. Overlay a) and b) are 2.9s, b) and c) 2.4s apart. The red colour channel marks a previous time step and the green colour channel marks a later frame accordingly. In a) the time difference of the red and green channel is 0.7s, for b) 0.6s and c) 7.4s. It can be observed in a) how the cells moved from being trapped in both beams equally, towards the centre of the left-hand laser beam. The left most cell aligned well with the left-hand beam (L), the right most cell with the right-hand beam (R). After, the cells circulate between different instable positions inside the trapping area.

Moving on from the characterisation of cell movement caused by fibre misalignment, overall both types of trapping devices were able to achieve stable trapping, as will be discussed in the Sections below. The constructed ferrule based open DBLTs had generally a higher probability of good fibre alignment, yet the PDMS based open DBLTs had advantages. One being the ability to vary the trap height by choosing the bottom layer thickness of the devices and cutting it out, while bonding the whole device on a coverslip. This enhances the time to actually trap specimen immensely as less specimen pass through below the fibres. Further, the possibility of cleaning the devices with solvents (PDMS devices) after usage turned out superior over surfactants (ferrule devices), to keep both the device and fibres free from dirt and thus increase the devices' lifetime. In the next Section the experimental results showing the proof of concept of the HOMCR are presented.

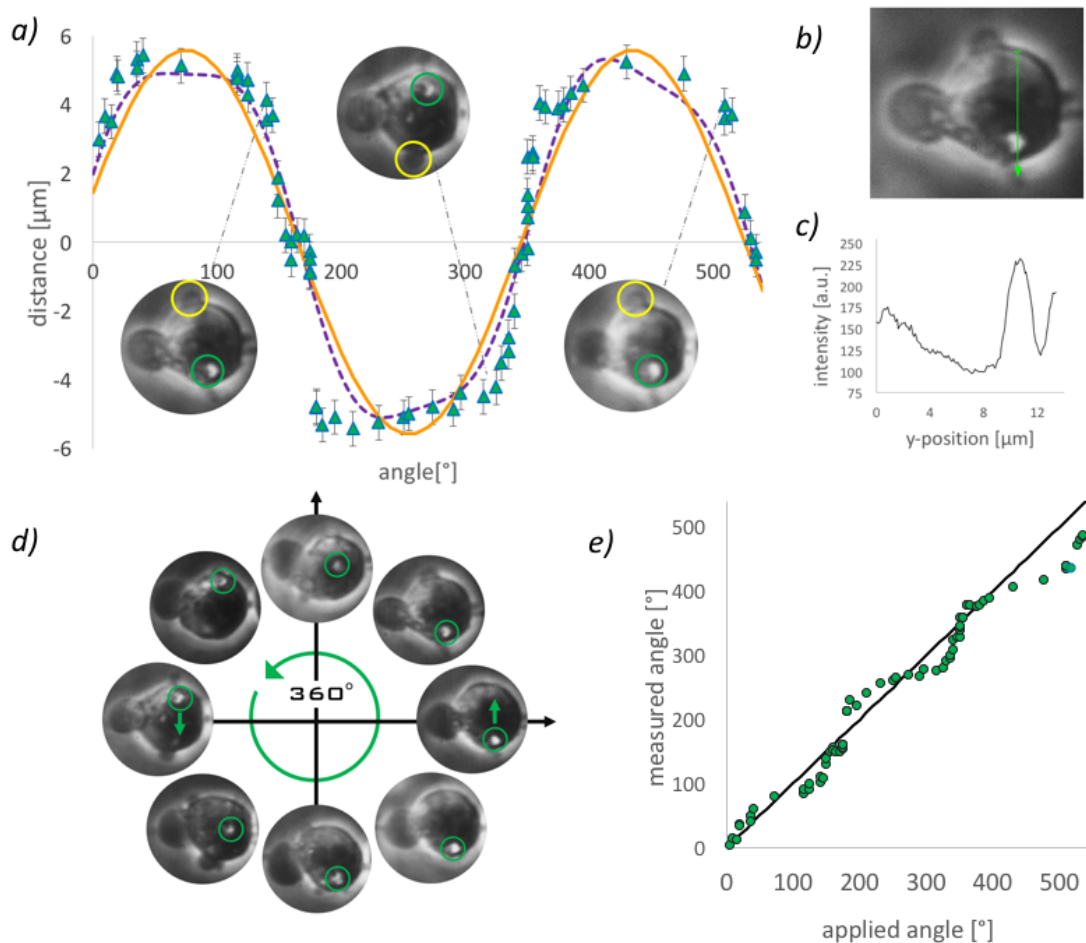


Figure 5–15: The successful rotation of a K562 cell by 540° degrees is displayed. a) Looking at the circular excerpts from left to right the reader is encouraged to follow the rotation of two highlighted cellular features (green and yellow circle). The orientations shown are 140°, 324° and 515°. So consecutively approximately 180° apart. The data (green triangles) was acquired tracking the bright spot(s) highlighted in green, while the cosine in orange shows the ideal rotation a spot on a sphere with the same radius would undergo. In dashed and purple, a fit considering a precession of the rotational axis is drawn. b) The region of interest (ROI) in green used to determine the orientation of the cell. The image is taken at 140°, this is the same as the first image in a). c) The actual intensity profile of the ROI. Peak detection reveals the cells orientation by tracking a bright spot. d) To make the rotation more visible to the reader consecutive orientations between 80° and 440° (360°) are displayed. e) Applied angle vs measured angle plotted concerning the projection of the tracked spot. The deviation from identity is partially understood as the cell is tilting left and right, undergoing precession. The cell measured 12.1µm vertically.

5.4 SUCCESSFUL ROTATION OF K562 CELL IN AN OPEN-PDMS DBLT

After initial trapping was tested in both types of open trapping devices, the focus was shifted towards cell rotation induced by the HOMCR. The proof of concept could be given in Section 5.3.1, yet the data was not showing improvement of specimen rotation in a DBLT compared to the literature. Hence, this is presented in the following.

An open PDMS DBLT was constructed as described in 5.2.3.1. The single mode fibre was pulled back to free up necessary space to insert the custom-built mirror for in-situ mode calibration. Once in place, the mirror sat still inside the device and mode calibration similar to 4.3 (page 55) was performed. Selecting and reproducing

LP_{11} modes in a 180° range was tested and verified. The fibre width was carefully set to $110\mu\text{m}$, resulting in a beam diameter in the middle of the trap of approximately $18\mu\text{m}$, while the total trapping power was set to a total of 170 mW. Specimen were flushed into the device via a pipette and flow was induced in order to locate cells in the trapping area.

Once trapping of a K562 cell could be established, effective stepwise orientation of the sample around 540° in 69 steps was achieved. The resulting data is presented in Figure 5–15. Bright organelles, situated near the membrane, $5.4\mu\text{m}$ off-centre, could be tracked around the full revolution of the cell (marked with a green ring in Figure 5–15 d)). The tracking enabled accurate recording of the HOMCR-induced cell rotation. The organelles were traced using peak detection along a linear region of interest (ROI), perpendicular to the rotational and therefore laser axis. Figure b) shows an example of the ROI and the resulting data in c). For each orientation of the HOM signal, the position of the organelles was followed and plotted as Figure 5–15 a) shows. The excursion of a point with a constant distance to its rotational axis (the centre of the three organelles and the centre of the cell respectively), follows a sine with regard to its projection on plane parallel to the rotation axis. When considering the phase and amplitude of the rotation the expected projected trajectory can be drawn, orange in Figure 5–15 a). The amplitude of the curve equals the rotation radius of the tracked objects, whilst the period of the rotation equals 360° and the phase is the offset from centre the tracked objects faced at a 0° mode angle. The projection of the tracked bright spots was in approximate agreement with the expected one, although it seems to have deviated periodically from the prediction. This indicates that the cellular object was not only rotating around an axis parallel to the laser axis. Adding precession three times the frequency of the main rotation, results in an enhanced matching of the data (purple curve).

The deviation from a simple projection of the spots can be understood by acknowledging that the trapped specimen was not entirely spherical and even features two blebs. Being non-symmetrical, the position of equilibrium of trapping forces does not equal the major axis, yet that does not necessarily cause precession. A further possibility of the two lobe signal was imbalanced as to its intensity of the two lobes. Imbalance of different dual lobe modes could add an additional rotational force, tilting the object perpendicular to the trapping axis, similar to the gravitational pull the moon and planets of the solar system exert on the earth.

Figure 5–15 e) shows the measured angle of cell rotation compared to the applied mode angle. The periodic deviation can be well followed. Seemingly, after a full rotation of 360° the alignment decreased further. While this does not seem crucial for the tomographic application of the HOMCR, as the object was scanned at all orientations, it indicates margin for improvement.

Yet, overall the stepwise rotational alignment of the cell was performed in great detail. Comparing to the literature presented in Section 5.1 this is the most detailed non-continuous rotation of a cellular object in suspension. This is a very promising result and shows the capabilities of the HOMCR. In the next Section the work towards the upscaling of accommodating larger biological samples in the HOMCR is presented.

5.5 DISCUSSION

With the goal of an all-fibre Dual Beam Laser Trap enabled cell rotator, the development of a novel mode manipulator of Chapter 4 was built upon into a trapping device. The availability of ready-to-use designs of PDMS chip-based DBLTs, within the lab, facilitated the rapid manufacturing and testing of the new devices. The results of K562 two-cell cluster experiments demonstrated the ability to orient the specimen in the trapping area. The proof that the concept of the HOMCR works was given and similar results can be found in the literature, using concepts as described in the background Section. However, trapping and the manipulation of larger objects is desired as it promises the most novelty. Another shortcoming is that through the nature of a microfluidic chip a reasonably large volume of liquid will be flushed into the channel and tubing, dealing with small sample amount and small volumes is problematic. The bespoke reasons and the inability to calibrate the piezo voltages, required for producing each oriented mode, led to moving away from the enclosed PDMS devices towards a more open architecture, which could allow for the very practical *in-situ* mode calibration.

Utilising a custom-built mirror, the mode signal of the DMF could be reflected upwards into a CCD camera placed above the trap. The *in-situ* method opened up a more direct approach to setup the HOMCR, while being ready to trap specimen without moving any parts besides the mirror and the second beam arm. This is a fundamental improvement to the more blind experiment of a closed microfluidic chip. In the open configuration, the signal can always be imaged without disassembling the trap in its entirety.

Two different open DBLTs were presented, both capable of trapping biological specimen. The first type of device was a logical transition building upon the already used PDMS microfluidic chips. Cutting out the microfluidic channel while elevating the whole trap provided an enlarged trapping device with open access from the top. Shaping the basin helped aligning the mirror for *in-situ* mode calibration. The second approach used commercially available ceramic fibre ferrules. While a single ferrule has been used before to form a DBLT via drilling a hole in the middle of the ferrule by Kresying *et al.*²⁰, however two ceramic ferrules have not been employed before to form a DBLT. Aligning two ferrules via a single fibre that was inserted into both of the ferrules proved to result in sufficient coaxial alignment of a DBLT. This is a very low cost and direct method to create a DBLT.

Furthermore, the open ferrule DBLTs had better fibre alignment compared to the open-PDMS DBLTs, although the trapping height of half the ferrule diameter caused problems in trapping efficiency, as a large number of samples simply passed below the two fibres. Clearly, the ferrule trap underperformed for small samples but offers a useful and elegant device for bigger samples as will be shown in Chapter 0. DBLTs of the size presented in this work could not be found in published research.

Compared to the rotation of a two cell cluster in the microfluidic chip (Section 5.4), showing the proof of concept of the HOMCR, the results of a detailed, stepwise rotation of a K562 cell around 540° could be obtained in Section 5.4. Thus it was shown that using the HOMCR in an open-PDMS DBLT for tomographic sample orientation succeeded. Tracked organelles inside the cell unveiled the gyration caused by the HOMCR in detail. Imaging in 2D represents a projection of the imaged object onto the camera. Therefore, the trajectory for the tracked organelles projected onto the imaging plane followed a sine like function. This is expected for a spot on a spheroid, rotating perpendicular to the imaging plane. However, the sample was not entirely rotationally symmetric and displayed additional precessional movement. The precession could be caused by partially non-symmetric dual lobe mode signal, as sample would get more radiation pressure from only one of the lobes and then tilts away from it. This would explain the deviation in measured angle from the expected angle. Yet, compared to the literature discussed in the background Section 5.1, this is the most accurate and detailed stepwise orientation of a biological specimen via a contactless trapping method. This exciting result led to exploring further applications of the HOMCR to orient samples larger than the single cell level, highlighted in the next Chapter.

5.6 CONCLUSION

When embedding the HOMCR into different DBLTs, the HOMCR proved itself to be a useful and powerful tool for specimen orientation in a DBLT environment. Several devices were developed, a closed microfluidic chip and two different types of open trapping devices were all successfully employed for trapping. Accurate stepwise sample orientation of a K562 cell was shown around 540° . Correctly rotating the specimen around a tomographic axis gives rise to a fruitful outlook of applications in the field of biology for the HOMCR.

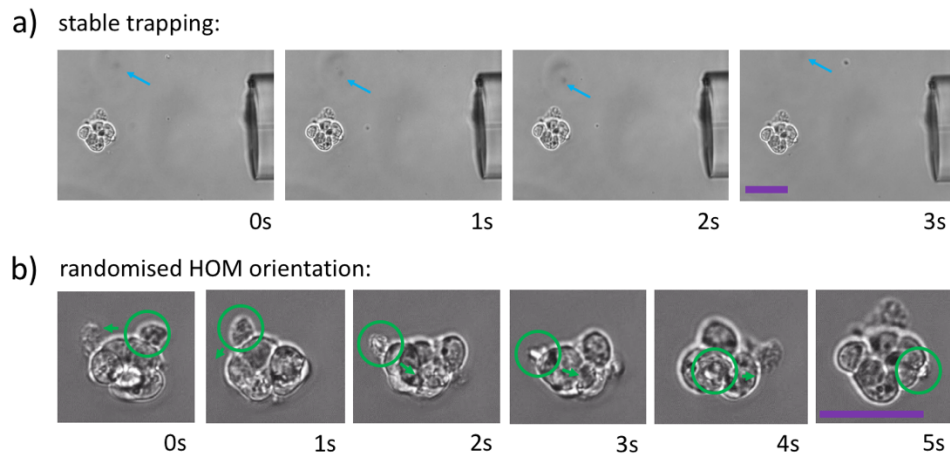


Figure 6–1: Trapping of a cell cluster in an open-ferrule trap. a) Comparing to the fibre position, the cell cluster of approximately $45\mu\text{m}$ in diameter was stably trapped. The cells were obtained from a commercially available immortalised human hepatocyte cell line HepaRGTM. b) By manually twisting and squeezing of the dual mode fibre, the cluster was reoriented as the higher order mode was manipulated due to the stress. The scale bars measure $50\mu\text{m}$.

6 TRAPPING OF MULTICELLULAR OBJECTS

Optical trapping and DBLTs are not limited in terms of the biological samples to working only with single cells, it has been shown that they can trap and manipulate multi-cellular samples. Tomographic cell rotation can provide even more benefits for multicellular samples due to the scattering nature of cells. While a single cell is quite transparent, the presence of internal organelles results in light being scattered heavily. For a single layer of cells, this effect is small and high-resolution images can be obtained, however for thicker samples, multiple scattering events causes a dramatic loss in image quality and ability to successfully image into and through the sample.

As the sample thickness increases, so does the perturbation of the signal representing the sample that is collected in the microscope's objective. In order to image the whole object in 3D without sample rotation, the image plane has to be moved through the entire height of the object, commonly done by z-stacking, a technique moving the objective stepwise closer to the object, changing the focus and imaging one plane above the last each time. Instead, by tomographic sample rotation, the necessary effective distance of matter the light has to travel through to image the whole specimen can be reduced by a factor of two. Together with the 3D reconstruction tomography based on rotation generally enables, sample rotation by mode rotation is an elegant way to further improve imaging quality thoroughly for multicellular samples.

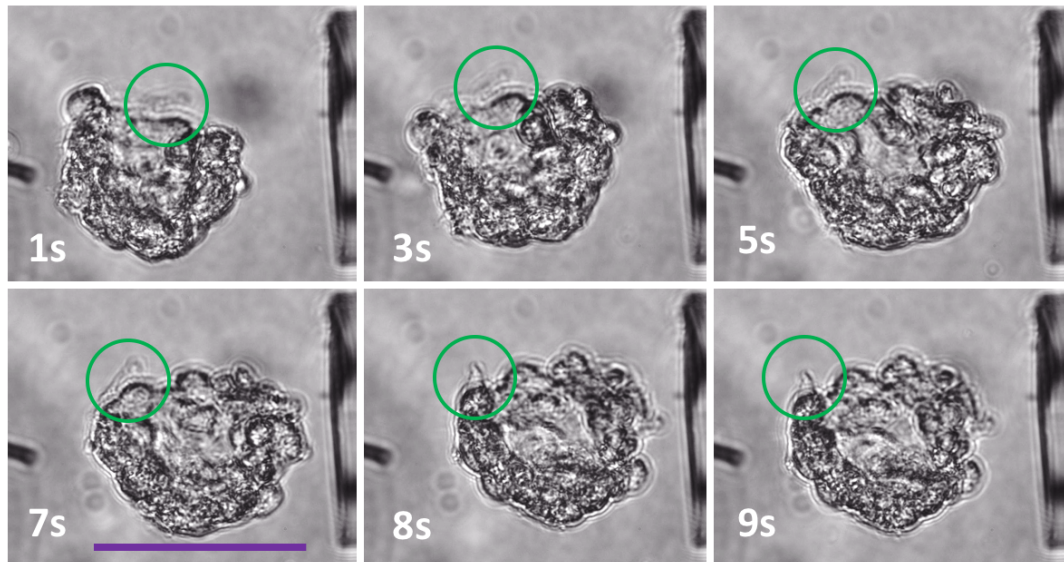


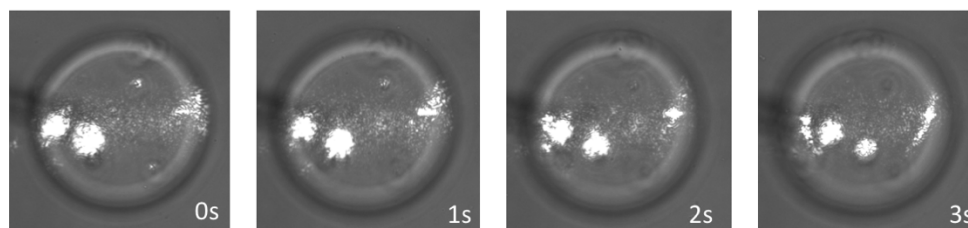
Figure 6–2: The trapping and manipulating of a $100\mu\text{m}$ wide HepaRGTM cell cluster in an open-ferrule trap. The dual mode fibre was manually manipulated to produce random mode patterns. This results in the orientation of the cluster from 0 to 8 seconds, after the fibre manipulation stopped and the cluster was held stationary. The scale bar measures $100\mu\text{m}$.

6.1 TRAPPING AND MANIPULATING OF CELL CLUSTERS IN AN OPEN FERRULE TRAP

To test that the trapping and manipulation of cell clusters of different size and shape can be achieved by the methodology presented in this project, an open ferrule trap was constructed. The trap height was half the diameter of the ceramic ferrules, i.e. $625\mu\text{m}$. The fibre distance was first set to $450\mu\text{m}$ resulting in a beam diameter of around $54\mu\text{m}$ in the middle of the trap, the laser power was set to 560mW . With the support of Dirk-Jan Cornelissen in terms of sample preparation, multicellular specimen could be obtained. The samples tested consisted of: Cell clusters of HepaRGTM, an immortalized commercially available Cholangiocarcinoma liver cell line, the same HepaRGTM cells but encapsulated via printing into alginate beads in random distribution and cell clusters located in double emulsion in an alginate bead.

Exploring the manipulation of the sample, Figure 6–1 shows how a cluster of around $50\mu\text{m}$ in diameter could be trapped successfully (purple scale bar equals $50\mu\text{m}$). As can be seen in a), there was no observable rotation of the cluster and by comparison to the blue indicated particle, the cluster was stably trapped against a background flow. To verify that the higher order beam was able to orientate this cluster, the dual mode fibre was twisted in different orientations manually during the frames of 5 seconds in b). In the examples shown, it is clearly visible that the cluster has been rotated around two arbitrary axes. This can be seen by following the cell, highlighted via the green circle, it underwent rotation around two axes, first in parallel to the surface normal of the

a) IR trapping laser scatter:



b) Rotation of alginate bead (2 frames overlay):

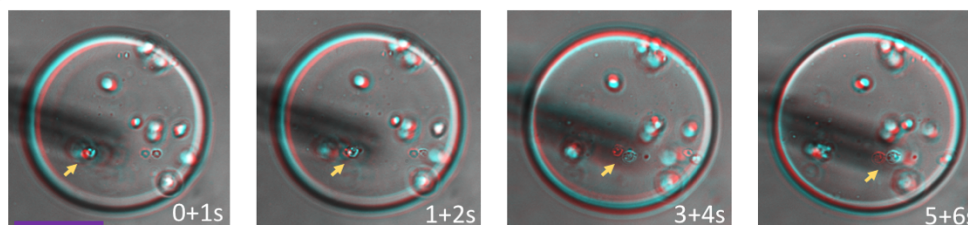


Figure 6–3: Trapping of printed Alginate beads with HepaRGTM cells enclosed. a) As the refractive index distribution across the whole bead was inhomogeneous the bead starts to rotate. The scatter of the laser-light highlights the refractive index distribution. b) The, to the laser axis perpendicular, rotation of the bead displayed, using overlays of two frames. The first frame in red occurred 1s before the second one in cyan. One cell in particular is highlighted by the yellow arrow to underline the movement pattern of the whole bead. The bead was roughly 180 μ m in diameter. Purple scale bar 100 μ m.

imaging plane for under 90° (0 to 2 seconds), then perpendicular to it (rotation of less than 180°).

The same experiment with a slightly different timescale of 1-7s of manipulation and 8-9s relaxation for a cluster of twice the diameter is presented in Figure 6–2. The trap was adjusted for the larger sample by gently pulling back the right hand fibre. The resulting fibre distance was 620 μ m (beam diameter \sim 72 μ m) with a total laser power of 840mW. The 100 μ m wide cluster could be manipulated as in Figure 6–1, although responding with latency.

6.2 TRAPPING AND MANIPULATING OF ALGINATE BEADS IN AN OPEN FERRULE TRAP

To further explore the range of objects which could be trapped, printed alginate beads were tested. Such beads are gaining interest in the bio-engineering community as alginate is non-toxic and its structure enables cells to be enclosed in a hydrogel, yet maintaining an exchange of ions and nutrition from the culture medium. The beads of up to 300 μ m in diameter contained HepaRGTM cells. Two different ways of printing were explored. In the first way, the cells were mixed into the alginate solution as the beads were being printed, and so the beads ended up with a stochastic distribution of cells over the whole volume. In the second method, the medium with beads was printed in a double emulsion with the alginate. The product ends up being of liquid core of

medium containing the cells, surrounded by hydrogel. As the alginate sphere's refractive index was very close to the refractive index of water and the buoyancy was low, density matching of the solution was carried out to help the sample trapping against gravity. Alginate beads containing no cells were a promising specimen for calibration purposes as they have a long shelf life, are cheap to manufacture, sterile and of interesting size. Yet, their trapping could not be achieved. The refractive index difference of alginate and surrounding medium was not enough in order to exert sufficient trapping force.

However, cell containing hydrogel beads could be trapped. Figure 6–3 shows a bead with random cell distribution trapped inside an open-ferrule DBLT. The total trapping power at the centre of the trap was 570mW, while the fibres were spaced by 620 μ m. As shown in Figure 6–3 a), imaging the back scatter of the trapping laser light, by taking the IR-filter out of the imaging pathway, highlights the refractive index profile of the specimen. The randomly distributed cells were small scatterers. This resulted in the inhomogeneity of the scattering forces and is very dependent on the individual bead and its orientation. The sample engages in rotation as shown in Figure 6–3 b). A red and cyan overlay of two frames, separated 1s from each other, shows the continuous rotation of the sample around an axis perpendicular to the trapping axis. A yellow arrow points at a cell that was easy to follow through its gyration. As it came to the centre of the bead, the on the camera projected movement was faster per second (see overlay 3+4s). One revolution of the hydrogel bead took roughly 13s. It should be mentioned that the specimen dropped out of the trap after 30s thus the trapping was not fully stable for longer periods. This is grounded in the inhomogeneity of the sample and thus refractive index profile, since the cells inside the hydrogel were randomly distributed.

A different cell density and distribution changed the trapping ability. This is shown in Figure 6–4 for a cell-cluster-containing double emulsion alginate beads. The trapping laser scatter displayed a significantly more homogeneous profile. This resulted in an equivalence of optical forces and a stable trapping position and orientation of the object. The alginate bead was about 300 μ m in diameter with the cell cluster having a width of the long axis of roughly 200 μ m. Although, there were larger objects trapped in the past in optical traps such as optical tweezers¹³² or an optical vortex pipeline¹³³, to personal knowledge this is the largest object trapped in a DBLT.

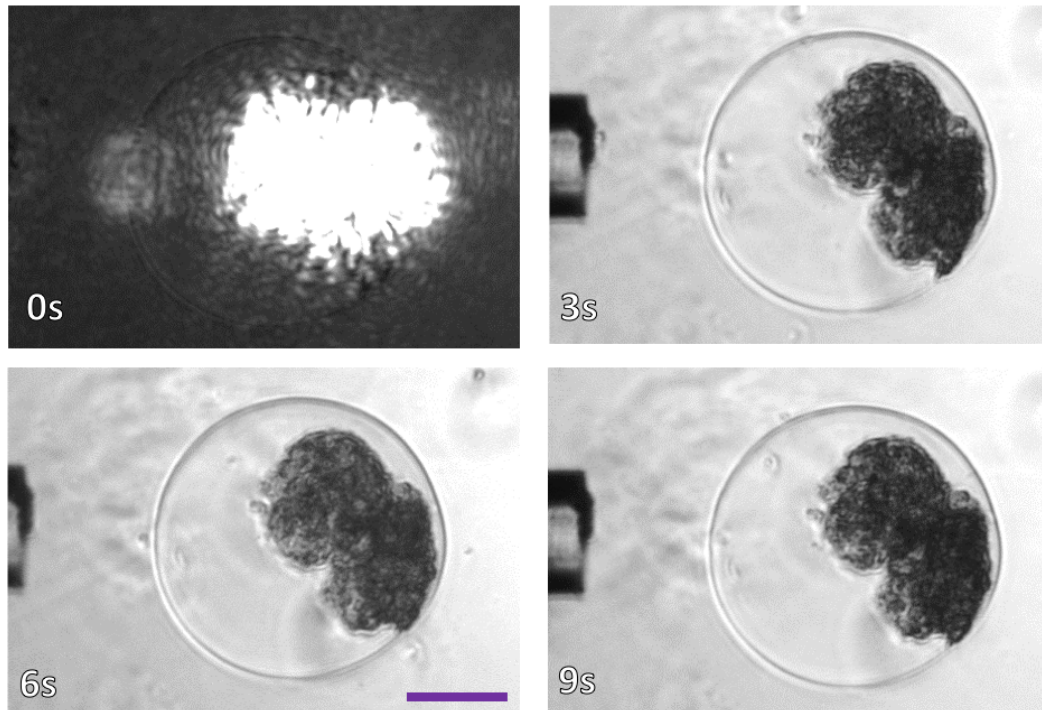


Figure 6-4 A more homogeneous refractive index distribution leads to stable trapping. An alginate bead with a dense cell population enclosed via double emulsion printing was controlled by the laser beams in a stable manner, when compared to the sparsely populated alginate bead in Figure 6-3. As shown at 0s the distribution of the backscatter of the trapping laser is more homogenous than in the previous figure (Image taken without infrared filter). The compilation of 3, 6, and 9s shows the rest of the object in the trapping position. The bead could be stably trapped and did not change its trapping position. The scale bar measures 100 μ m. The alginate bead being roughly 300 μ m big is one of the largest objects that was trapped in this work.

6.3 DISCUSSION

Although the complete result of the orientation of multi-cellular samples via the HOMCR could not be gathered during the time of the project, promising preliminary data of trapping and manipulating cell clusters in an open-ferrule DBLT was presented in this Chapter. The cell clusters were of 50 microns up to 200 microns in diameter, which is an interesting size range as the implementation of complex spheroid cultures in biology is growing¹³⁴. Using an open DBLT setup, sample loading was slow and inaccurate. To gain higher throughput this has to be improved. Picking up individual sample via micropipette aspiration was successfully performed. Designing a device with narrower trapping area than the presented open DBLTs could help the throughput although the traps would be then restricted to certain sized samples, without providing the option to pull the non HOM fibre back to increase the trap size for larger specimen. A further drawback of the open designs was that the fibre facets were not protected of collecting any dirt, thus making the traps less durable compared to a capillary based system. Coating the laser fibres with a non-stick agent such as Pluronic to repel dirt particles and keep the fibre ends clean, is proposed for the future device construction and experiments.

6.4 CONCLUSION

From the alignment of single cells, the capability of the HOMCR enabled DBLTs to trap multi-cellular samples up to 20 times the diameter was shown. Manipulation by a randomised higher order mode was capable to orient cell-cluster as shown in 6.1. This demonstrates that the HOMCR is the right tool for the alignment of larger samples. Increasing the obtainable 3D resolution for multi-cellular objects is an area of research with a fruitful outlook to improve the current state of the art. To achieve full tomographic reconstruction of a multi-cellular object could not be finished in the course of this project, yet it is a pivotal goal for future work. Towards this goal, methods were explored in brief: accurate sample loading via micropipettes and the manufacturing of more spherical specimens in micro wells¹³⁴ or by utilising the hanging drop method, but as the time of the project came to an end, could not be finalised. The different samples trapped successfully in the open-ferrule DBLT are prosperous for future work on various specimen. 3D culture modelling¹³⁴ is a rising area of research with the potential to mimic tumours¹³⁵ or organoids¹³⁶. In a complex 3D structure, it will be useful to gain the full 3D information. Again, as shown in the first part of this Chapter, the HOM signal can manipulate samples larger than single cells, this results in a fruitful outlook for the HOMCR to be applied to solve more questions across fundamental biology.

7 CONCLUSION & FUTURE OUTLOOK

During the course of this thesis, several applications of Dual Beam Optical Trap were explored: by increasing the laser power to stretch trapped mammalian cells, or the laser signal was shaped to align and rotate the cells. While following the first path allowed to gather mechanical information about different cell phenotypes, or mutant cells, using a well established technique, the second route led to a novel, promising tool, capable of controlled, stepwise, rotational alignment of cellular specimens, named the Higher Order Mode Cell Rotator, in short HOMCR.

Prior to the start of the engineering process of the novel device, it was necessary to develop experience in handling Dual Beam Optical Traps (DBLTs), using a particularly successful design of DBLT, the Optical Stretcher (OS). This phase led to a deep understanding of the usage of the technique of Dual Beam Laser Trapping, as well as specific scientific findings relating mechanical dissimilarities between different cell types. These findings have been outlined in Chapter 3 and are briefly summarised again below.

In the initial exploration of the Dual Beam Laser Trap (DBLT) of Chapter 3, the samples inspected with the Optical Stretcher (OS) ranged from stem cell derived, surface acoustic wave treated erythrocytes (Section 3.4.1); over tumour suppressor lacking leukaemia cells (Section 3.4.2); to human embryonic kidney cells with modifications in the FUS gene (Section 3.4.3); and finally the inspection of nuclei of Mouse Adult Fibroblasts (MAF), differing in content of a leading protein of the nuclear envelope (Section 3.4.4). A high level of statistical significance could be achieved in the majority of the Optical Stretcher measurements, detecting mechanical differences between the different cell types.

For example in Section 3.4.2, the investigated Glioblastoma cells, containing the tumour suppressor PTEN, were shown to be significantly stiffer than the control group (see Figure 3–6). In the past, cellular stiffness could be linked to a cell's metastatic potential and contribute one possible explanation of the tumour's suppressing properties the protein PTEN inherits.

The FUS gene, linked to neural motor disease such as Amyotrophic Lateral Sclerosis, could be shown to decrease cellular deformability in its wild type significantly, when compared to FUS null control cells and several FUS gene mutations (see Section 3.4.3; see Figure 3–8). FUS in its wild type seemed to increase the structural integrity of the

given cells. Moreover, AdOx a potential drug, preventing the accumulations of FUS outside of the nucleus, demonstrably increased deformability of FUS wild type cells (see Figure 3–9).

Further, not only whole cell deformability, but also nuclear deformation could be investigated by imaging nuclear-stained MAF-cells under EPI fluorescence. While the OS results of Section 3.4.4 could successfully support the publication “Optomechanical measurement of the role of lamins in whole cell deformability” by Kolb et al.⁹⁸ (see Figure 3–11), it also provided inspiration for future work. The nucleus is interconnected in the whole cell and plays an important part in the whole cell deformability, as shown in the mentioned publication, yet measuring both, the whole cell and the nuclear stiffness simultaneously, would open up added possible investigations, increasing the understanding in cellular rheology. This can be achieved by splitting the bright field signal of the whole cell and the fluorescent signal of the nucleus onto different areas of the camera chip, exploiting a diffraction grating. Using two cameras would be possible too, but this leads to an unnecessary requirement to synchronise more than one measuring device.

Extending this, not only the nucleus and the cell could be imaged in parallel. Other cellular contents that can be stained, could be imaged separately, thus multiple combinations could be observable. It is possible that the microtubules, will be discovered to stretch in a different way than the rest of the cytoskeleton. It would also be useful to consider how the mechanical load propagates in all of the various cells’ body and how the parts are effected by stretching. Hence, simultaneous fluorescent imaging potentially adds a new dimension to the power of the OS.

After gaining expertise in optical trapping using the OS, the core part of this thesis was to engineer an all-in-fibre, DBLT based, cell rotating tool, the HOMCR. Serving the goal of the controlled tomographical rotation of cellular specimen via the method of beam shaping, the suitability of a polarisation controlling device (PCD) to orient the dual lobe containing higher order mode LP_{11} , was probed in Chapter 4.

The PCD, with the functional principle based on piezo-electric fibre squeezing, was shown to be capable of more than manipulating the polarisation of single mode fibres, as it has been previously used for, but can also manipulate the modes within a few mode optical fibre. By launching a fundamental mode into a few mode fibre using an offset splice, the PCD showed great capabilities to cast and orientate LP_{11} modes in a fast and

repeatable manner, however due to the PCD applying phase changes to the propagating modes, there is not a one-to-one relationship between the voltage applied to the piezo and the angle of the resulting mode. The method of choice for uncovering this relationship was a calibration of the effect of the PCD, based on raster scanning (Section 4.4.3). By scanning through a preselected voltage range, applied to all four piezoelectric fibre squeezers, high quality LP_{11} modes suitable for cell trapping and orientation could be obtained for approximately 35% of the voltage combinations. After the scan was finished, the best mode examples for each angle were sorted according to quality. Picking and reproducing the very best examples, with increasing angle, could be shown (see Section 4.4.7; see Figure 4–15) and formed the stepping stone necessary in order to move forward towards the goal of engineering an all in fibre optical trap for the tomographic orientation of living specimen.

In the process of building a HOMCR, different trap designs were considered and tested. Firstly, a PDMS microfluidic chip based DBLT (Section 5.2.2) which was easy to manufacture, provided elegant sample loading and was easy to clean, but the chip was limited in regard of specimen size and direct inspection of the laser mode was impossible after assembly. The closed nature of the microfluidic chip demanded a PCD mode calibration prior to completing the optical trap via fibre insertion. Although, trapping and orientating could be shown in Section 5.3.1, the object was not tracked in detail. Considering the character of the LP_{11} mode, slight misalignment of the fibres could cause the various modes' qualities to suffer and as the microfluidic chip is closed, no re-inspection of the modes was possible. A higher certainty of the mode quality would be ensured if the imaging of the LP_{11} containing laser beam was enabled prior to the trapping without fundamental changes to the setup.

Newly designed open trapping devices (Section 5.2.3) and the custom manufacturing of small Aluminium mirrors (Section 5.2.4) made a highly convenient *in-situ* mode calibration possible. Using this approach, an accurate stepwise rotation around one-and-a-half rotations of a single K562 cell could be tracked, and showed the powerful capabilities of the HOMCR (see Section 5.4 and Figure 5–15). This proof of concept is highly motivating for future projects. While the agreement with the expected rotational alignment deviated slightly, overall the stepwise orientation was accurate, featuring more steps per full rotation than reported for any other non contact cell-rotation method in the current literature, as discussed in Section 5.1.

It should be mentioned that the state of polarisation of the trapping and manipulating LP_{11} modes was not probed prior to trapping during the experiments, only the intensity pattern. For one angular orientation of a LP_{11} mode, two orthogonal polarisations are possible. Cellular sample can provide birefringent components¹³⁷ and therefore the polarisation of the trapping beam can exert more or less angular momentum accordingly. Measuring the effect of polarisation control on trapped cellular sample, even for the use of the fundamental mode instead of the LP_{11} mode might have interesting findings and should be considered for future work.

One major motivation for building the HOMCR using a dual beam optical trap, was the potential for the trapping and orientation of larger biological samples, which have the largest to gain in resolution improvements through tomographic rotation. To bring this pursuit closer, the trapping of cell clusters inside an open DBLT environment was investigated in Chapter 0. Multi-cellular sample, up to a diameter of approximately 200 μm , were successfully trapped. The trapping stability of printed, cell containing, alginate beads was dependent on the homogeneity and surface area of the sample's refractive index profile, as cells printed inside alginate beads revealed (see Section 6.2). Large clusters, consisting of directly connected cells, however trapped without difficulty.

During the trapping of different clusters, the ability to manipulate their orientation via the higher order containing beam was tested by fibre twisting and proved effective as shown in Figure 6–1 and Figure 6–2. This directly indicates, that the torque of the higher order mode signal, not only suffices for tomographic alignment on the single cell level, but for samples much larger.

This paves the way towards immediate future plans involving the tomographic rotation of larger sample. In Heriot-Watt University collaborations were thought out researching the development of Pancreatic Eyelets and MCDK cyst clusters or of the printed HepaRGTM cells inside Alginate beads, bespoken in Section 6.2.

After their tomographic rotation, gaining a first 3D reconstruction of the object and measuring the resolution improvement compared to conventional z-stacking seems to offer a suitable step forward. For this the setup needs to leave the arrangement of a conventional bright field microscope and move most likely towards a confocal microscope. 3D tomography is commonly the product of multiple projections, in bright field microscopy the depths of field is too large, features out of focus contribute to the

current image and the reconstruction would become blurry. Confocal Laser Scanning Microscopy scans through the sample and minimises the background for each captured imaging plane. A state of the art confocal microscope is available at the ESRC facilities of Heriot-Watt University. But this is a shared facility and time on the microscopes is limited, therefore the HOMCR needs to be optimised furthermore. For example, the number of orientations for a high quality reconstruction needs to be ideally in the hundreds, higher than the number of orientations of $44/360^\circ$ provided in Section 5.4. Reconstructions without too many artefacts can be achieved for a number greater a value like sixty-four (dependent on sample and imaging system)¹³⁸. Further, the trapping needs to be stable, so that the specimen stays centred in the microscope. All in all, when acquiring the tomographic data new problems will arise that will be in need for optimisation, such as finding the best 3D reconstruction algorithm and method, and the search for which cellular components to stain and focus on, in order to provide the most exiting scientific studies.

Besides tomography, the torque aligning the sample could be potentially used in other ways to probe living specimen. Overall, the exploration of trapping larger sample motivates towards future work using the HOMCR on more complex cellular specimens. The ability to hold a multicellular object in a given orientation, without any physical contact allows a range of new biophysical studies to be carried out across a range of biological questions and scales, from individual cells to whole microorganisms. Phototaxis¹³⁹ is the active movement of living organisms optimising light absorption and is under discussion to mark the evolutionary beginning of the development of eyes¹⁴⁰. Several forms of algae orientate itself towards light¹⁴¹. Schaller *et al.*¹⁴² investigated the alga *Chlamydomonas* and presented findings on the alga's orientation regarding time dependence, photon flux and sensitivity subject to the light's wavelength. Similarly, different zooplankton provides an interesting sample size, fitting into the above presented DBLTs, whilst also being dependent on simple photoreceptors to perform phototaxis¹⁴³. Modifying the HOMCR, shining a second light source optimised for the alga's or plankton's receptors wavelength, while probing how much torque the sample can resist before it misaligns from the light source, could provide novel insight into the rotational forces which can be exerted by the animal. Alternatively, the light intensity threshold that is needed to align a specimen could be probed dependent on precise orientation. Further, the eyespot of the alga is not always at the same spot and will influence the phototactic alignment of the specimen which could be probed.

Another potential way to measure more complex biological processes via the HOMCR is during the application of drugs on tumour models. In the introduction of this thesis, the visionary approach to design more complex and heterogeneous tumours in 3D culture was mentioned. An often overlooked fact when studying new potential drugs for treating a tumour is the delivery of the substance into the tumour in a homogeneous way¹⁴⁴. The treatment, for example originating from the blood stream, diffuses into the tumour insufficiently and parts of the tumour stay intact. Directionally dependent effects of drug treatment could be studied by aligning a bio-printed tumour with the HOMCR, after it was treated by diffusing drugs into it, studying the differences of one side of the tumour compared to the other.

Going back to purely tomographical applications, mapping and gathering 3D data of biological objects, as for example the mouse atlas¹⁴⁵, enhances human knowledge and understanding which drives the depth of science forward. Engaging 3D visualisation technology like Virtual Reality and Augmented Reality, are about to get more advanced and implemented into human life. A myriad of related applications will appear. 3D visualisation of biological objects for training purposes in medicine is on the rise^{17,18}. To gather a vast collection of 3D data of biological objects will likely gain importance and the HOMCR could support this pursuit. To extend the usability in the laboratory an improvement of the HOMCR is easy to imagine. Similar to Augmented Reality, where a tablet or phone is used to orient the 3D virtual specimen, increasing the user's experience, a tablet could be synched directly to the HOMCR so that turning the tablet will align the specimen simultaneously, showing the gathered imaging on-screen live and in an interactive, immersive way.

To summarise, the creation of the HOMCR resulted in a powerful, affordable, non-alignment intensive, all-in-fibre based tool for tomographical cell rotation coming into existence. As first prosperous data could be recorded, the next step lies in crafting the concept and design to user friendly device that can be easily adapted on different imaging systems to conquer the biological lab. Finally, the fact that this apparatus has been proven to be able to handle a variety of different specimens under various laboratory settings means that there is robust space for growth in this field of research.

8 REFERENCES

1. Alberts B, Johnson A, Lewis J, et al. *Molecular Biology of the Cell*. (2002).
2. Bianconi, E. *et al.* An estimation of the number of cells in the human body. *Ann. Hum. Biol.* **40**, 463–471 (2013).
3. Knowlton, S., Onal, S., Yu, C. H., Zhao, J. J. & Tasoglu, S. Bioprinting for cancer research. *Trends Biotechnol.* **33**, 504–513 (2015).
4. Samavedi, S. & Joy, N. 3D printing for the development of in vitro cancer models. *Curr. Opin. Biomed. Eng.* **2**, 35–42 (2017).
5. Ozbolat, I. T., Peng, W. & Ozbolat, V. Application areas of 3D bioprinting. *Drug Discov. Today* **21**, 1257–1271 (2016).
6. Peng, W., Unutmaz, D. & Ozbolat, I. T. Bioprinting towards Physiologically Relevant Tissue Models for Pharmaceuticals. *Trends Biotechnol.* **34**, 722–732 (2016).
7. Wang, L. & Wu, H. *Biomedical optics : principles and imaging*. *Wiley-Interscience* (2007).
8. Ourselin, S., Roche, A., Subsol, G., Pennec, X. & Ayache, N. Reconstructing a 3D structure from serial histological sections. *Image Vis. Comput.* **19**, 25–31 (2001).
9. Ito, T. & Okazaki, S. Pushing the limits of lithography. *Nature* **406**, 1027–1031 (2000).
10. Hong, K. M. & Shin, Y. C. Prospects of laser welding technology in the automotive industry: A review. *J. Mater. Process. Technol.* **245**, 46–69 (2017).
11. MAIMAN, T. H. Stimulated Optical Radiation in Ruby. *Nature* **187**, 493 (1960).
12. Ashkin, A. Acceleration and Trapping of Particles by Radiation Pressure. *Phys. Rev. Lett.* **24**, 156–159 (1970).
13. Guck, J., Ananthakrishnan, R., Mahmood, H., Moon, T. J. & Cunningham, C. C. The Optical Stretcher : A Novel Laser Tool to Micromanipulate Cells. **81**, (2001).
14. Shimizu, H., Yamazaki, S., Ono, T. & Emura, K. Highly practical fiber squeezer

- polarization controller. *J. Light. Technol.* **9**, 1217–1224 (1991).
15. Brooks, F. P. What's Real About Virtual Reality? *Proc. IEEE Virtual Real.* 2–3 (1999).
 16. Slater, M. & Sanchez-Vives, M. V. Enhancing Our Lives with Immersive Virtual Reality. *Front. Robot. AI* **3**, 1–47 (2016).
 17. Riener, R. & Harders, M. *VR for Medical Training - Virtual Reality in Medicine. Virtual Reality in Medicine* (2012).
 18. Seymour, N. E. *et al.* Virtual reality training improves operating room performance: results of a randomized, double-blinded study. *Ann Surg* **236**, 454–458 (2002).
 19. Yang, T., Bragheri, F. & Minzioni, P. A Comprehensive Review of Optical Stretcher for Cell Mechanical Characterization at Single-Cell Level. *Micromachines* **7**, 90 (2016).
 20. Kreysing, M. K. *et al.* The optical cell rotator. *Opt. Express* **16**, 16984 (2008).
 21. Kreysing, M. *et al.* Dynamic operation of optical fibres beyond the single-mode regime facilitates the orientation of biological cells. *Nat. Commun.* **5**, 5481 (2014).
 22. Guck, J. *et al.* The optical stretcher: a novel laser tool to micromanipulate cells. *Biophys. J.* **81**, 767–784 (2001).
 23. Guck, J., Ananthakrishnan, R., Cunningham, C. C. & Käs, J. Stretching biological cells with light. *J. Phys. Condens. Matter* **14**, (2002).
 24. Ashkin, A. Optical Trapping and Manipulation of Neutral Particles Using Lasers. *Opt. Photonics News* **10**, 41 (1999).
 25. Bowman, R. W. & Padgett, M. J. Optical trapping and binding. *Reports Prog. Phys.* **76**, 026401 (2013).
 26. Padgett, M. & Bowman, R. Tweezers with a twist. *Nat. Photonics* **5**, 343–348 (2011).
 27. Ashkin, a, Dziedzic, J. M., Bjorkholm, J. E. & Chu, S. Observation of a single-

- beam gradient force optical trap for dielectric particles. *Opt. Lett.* **11**, 288 (1986).
28. Neuman, K. C. & Block, S. M. Optical trapping. *Rev. Sci. Instrum.* **75**, 2787–2809 (2004).
 29. Ashkin, A. Forces of a single-beam gradient laser trap on a dielectric sphere in the ray optics regime. *Biophys. J.* **61**, 569–582 (1992).
 30. Svoboda, K. & Block, S. M. Biological applications of optical forces. *Ann. Rev. Biophys. Biomol. Struct.* **23**, 247–285 (1994).
 31. Padgett, M. J. & Allen, L. The angular momentum of light: Optical spanners and the rotational frequency shift. *Opt. Quantum Electron.* **31**, 1–12 (1999).
 32. Grier, D. G. A revolution in optical manipulation. *Nature* **424**, 810–816 (2003).
 33. Phillips, D. B. *et al.* Surface imaging using holographic optical tweezers. *Nanotechnology* **22**, 285503 (2011).
 34. Phillips, D. B. *et al.* Shape-induced force fields in optical trapping. *Nat. Photonics* **8**, 400–405 (2014).
 35. Constable, A., Kim, J., Mervis, J., Zarinetchi, F. & Prentiss, M. Demonstration of a fiber-optical light-force trap. *Opt. Lett.* **18**, 1867–1869 (1993).
 36. Kolb, T., Albert, S., Haug, M. & Whyte, G. Dynamically reconfigurable fibre optical spanner. *Lab Chip* **14**, 1186–1190 (2014).
 37. Lincoln, B. *et al.* Reconfigurable microfluidic integration of a dual-beam laser trap with biomedical applications. *Biomed. Microdevices* **9**, 703–10 (2007).
 38. Guck, J. *et al.* Optical Deformability as an Inherent Cell Marker for Testing Malignant Transformation and Metastatic Competence. *Biophys. J.* **88**, (2005).
 39. Ekpenyong, A. E. *et al.* Viscoelastic properties of differentiating blood cells are fate- and function-dependent. *PLoS One* **7**, e45237 (2012).
 40. Franze, K. *et al.* Muller cells are living optical fibers in the vertebrate retina. *Proc. Natl. Acad. Sci.* **104**, 8287–8292 (2007).
 41. Chalut, K. J. *et al.* Chromatin decondensation and nuclear softening accompany

- Nanog downregulation in embryonic stem cells. *Biophys. J.* **103**, 2060–70 (2012).
42. Gloge, D. & Equation, C. Weakly Guiding Fibers. **10**, 2252–2258 (1971).
 43. Chen, C. L. Foundations for Guided-Wave Optics. *Found. Guid. Opt.* 1–462 (2005).
 44. Snitzer, E. Cylindrical Dielectric Waveguide Modes. *J. Opt. Soc. Am.* **51**, 491 (1961).
 45. Kotrotsios, G. & Parriaux, O. Mode-holding capability of dual-mode fibers. *Opt. Lett.* **15**, 360–362 (1990).
 46. Gloge, D. Weakly Guiding Fibers. *Appl. Opt.* **10**, 2252–2258 (1971).
 47. Kreysing, M. *et al.* Dynamic operation of optical fibres beyond the single-mode regime facilitates the orientation of biological cells. *Nat. Commun.* **5**, 5481 (2014).
 48. Snyder, A. W. & Young, W. R. Modes of optical waveguides. *J. Opt. Soc. Am.* **68**, 297–309 (1978).
 49. Padgett, M., Courtial, J. & Allen, L. Light's Orbital Angular Momentum. *Phys. Today* **57**, 35 (2004).
 50. Snitzer, E. & Osterberg, H. Observed Dielectric Waveguide Modes in the Visible Spectrum. *J. Opt. Soc. Am.* **51**, 499–505 (1961).
 51. Brewster, D. On the Effects of Simple Pressure in Producing That Species of Crystallization Which Forms Two Oppositely Polarised Images, and Exhibits the Complementary Colours by Polarised Light. *Philos. Trans. R. Soc. London* **105**, 60–64 (1815).
 52. Schlosser, B. W. O. Delay Distortion in Weakly Guiding Optical Fibers Due to Elliptic Deformation of the Boundary. **51**, 4–9 (1972).
 53. Nagano, K., Kawakami, S. & Nishida, S. Change of the refractive index in an optical fiber due to external forces. *Appl. Opt.* **17**, 2080–2085 (1978).
 54. Ulrich, R., Rashleigh, S. C. & Eickhoff, W. Bending-induced birefringence in single-mode fibers. *Opt. Lett.* **5**, 273 (1980).

55. Primak, W. & Post, D. Photoelastic constants of vitreous silica and its elastic coefficient of refractive index. *J. Appl. Phys.* **30**, 779–788 (1959).
56. Blake, J. N., Kim, B. Y. & Shaw, H. J. Fiber-optic modal coupler using periodic microbending. *Opt. Lett.* **11**, 177–179 (1986).
57. Li, S., Mo, Q., Hu, X., Du, C. & Wang, J. Controllable all-fiber orbital angular momentum mode converter. *Opt. Lett.* **40**, 4376–9 (2015).
58. Raddatz, L., White, I. H., Cunningham, D. G. & Nowell, M. C. An Experimental and Theoretical Study of the Offset Launch Technique for the Enhancement of the Bandwidth of Multimode Fiber Links. *J. Light. Technol.* **16**, 324–331 (1998).
59. Guck, J. *et al.* Optical deformability as an inherent cell marker for testing malignant transformation and metastatic competence. *Biophys. J.* **88**, 3689–3698 (2005).
60. Swaminathan, V. *et al.* Mechanical Stiffness grades metastatic potential in patient tumor cells and in cancer cell lines. *Cancer Res.* **71**, 5075–5080 (2011).
61. Fu, Y. *et al.* A study of cancer cell metastasis using microfluidic transmigration device. *Proc. IEEE Int. Conf. Micro Electro Mech. Syst.* 773–776 (2012).
62. Kießling, T. R. *et al.* Analysis of multiple physical parameters for mechanical phenotyping of living cells. *Eur. Biophys. J.* **42**, 383–394 (2013).
63. Boyde, L., Chalut, K. J. & Guck, J. Interaction of Gaussian beam with near-spherical particle : an analytic – numerical approach for assessing scattering and stresses. **26**, 1814–1826 (2009).
64. Fletcher, D. A. & Mullins, R. D. Cell mechanics and the cytoskeleton. *Nature* **463**, 485–92 (2010).
65. Mainardi, F. & Spada, G. Creep, relaxation and viscosity properties for basic fractional models in rheology. *Eur. Phys. J. Spec. Top.* **193**, 133–160 (2011).
66. Wottawah, F. *et al.* Characterizing single suspended cells by optorheology. *Acta Biomater.* **1**, 263–271 (2005).
67. Hochmuth, R. M. Micropipette aspiration of living cells. *J. Biomech.* **33**, 15–22 (2000).

68. Lange, J. R. *et al.* Microconstriction Arrays for High-Throughput Quantitative Measurements of Cell Mechanical Properties. *Biophys. J.* **109**, 26–34 (2015).
69. Otto, O. *et al.* Real-time deformability cytometry: on-the-fly cell mechanical phenotyping. *Nat. Methods* (2015).
70. Palermo, G., Joris, H., Devroey, P. & Van Steirteghem, A. C. Pregnancies after intracytoplasmic injection of single spermatozoon into an oocyte. *Lancet* **340**, 17–18 (1992).
71. Rowat, a C., Lammerding, J. & Ipsen, J. H. Mechanical properties of the cell nucleus and the effect of emerin deficiency. *Biophys. J.* **91**, 4649–4664 (2006).
72. Dahl, K. N., Kahn, S. M., Wilson, K. L. & Discher, D. E. The nuclear envelope lamina network has elasticity and a compressibility limit suggestive of a molecular shock absorber. *J. Cell Sci.* **117**, 4779–86 (2004).
73. Qi, D., Hoelzle, D. J. & Rowat, a C. Probing single cells using flow in microfluidic devices. *Eur. Phys. J. Spec. Top.* **204**, 85–101 (2012).
74. Byun, S. *et al.* Characterizing deformability and surface friction of cancer cells. *Proc. Natl. Acad. Sci.* **110**, 7580–7585 (2013).
75. Adamo, A. *et al.* Microfluidics-based assessment of cell deformability. *Anal. Chem.* **84**, 6438–6443 (2012).
76. Rowat, A. C. *et al.* Nuclear envelope composition determines the ability of neutrophil-type cells to passage through micron-scale constrictions. *J. Biol. Chem.* **288**, 8610–8618 (2013).
77. Kuznetsova, T. G., Starodubtseva, M. N., Yegorenkov, N. I., Chizhik, S. A. & Zhdanov, R. I. Atomic force microscopy probing of cell elasticity. *Micron* **38**, 824–833 (2007).
78. Pillarisetti, A. *et al.* Mechanical phenotyping of mouse embryonic stem cells: increase in stiffness with differentiation. *Cell. Reprogram.* **13**, 371–380 (2011).
79. Rosenbluth, M. J., Lam, W. a & Fletcher, D. a. Force microscopy of nonadherent cells: a comparison of leukemia cell deformability. *Biophys. J.* **90**, 2994–3003 (2006).

80. Rodriguez, M. L., McGarry, P. J. & Sniadecki, N. J. Review on cell mechanics: Experimental and modeling approaches. *Appl. Mech. Rev.* **65**, 060801 (2013).
81. Kollmannsberger, P. & Fabry, B. High-force magnetic tweezers with force feedback for biological applications. *Rev. Sci. Instrum.* **78**, 114301 (2007).
82. Mitchison, J. & Swann, M. The mechanical properties of the cell surface II. The unfertilized sea-urchin egg. *J. Exp. Biol.* **31**, 461–472 (1954).
83. Fontes, A. *et al.* Mechanical and electrical properties of red blood cells using optical tweezers. *J. Opt.* **13**, 044012 (2011).
84. Suresh, S. *et al.* Reprint of: Connections between single-cell biomechanics and human disease states: Gastrointestinal cancer and malaria. *Acta Biomater.* **23**, S3–S15 (2015).
85. Tibarewal, P. *et al.* PTEN Protein Phosphatase Activity Correlates with Control of Gene Expression and Invasion, a Tumor- Suppressing Phenotype, But Not with AKT Activity. **5**, 1–12 (2012).
86. Chu, E. C. & Tarnawski, A. S. PTEN regulatory functions in tumor suppression and cell biology. *Med. Sci. Monit.* **10**, RA235-A241 (2004).
87. LESLIE, N. R. & DOWNES, C. P. PTEN function: how normal cells control it and tumour cells lose it. *Biochem. J.* **382**, 1–11 (2004).
88. Davidson, L. *et al.* Suppression of cellular proliferation and invasion by the concerted lipid and protein phosphatase activities of PTEN. *Oncogene* **29**, 687–697 (2010).
89. Ochalek, T., Nordt, F. J., Tullberg, K., Variants, M. C. & Burger, M. M. Correlation between Cell Deformability and Metastatic Potential in B16-F1 Melanoma Cell Variants Correlation between Cell Deformability and Metastatic Potential in B16-F1. 5124–5128 (1988).
90. Suresh, S. Biomechanics and biophysics of cancer cells. *Acta Mater.* **55**, 3989–4014 (2007).
91. Fujii, S., Takanashi, K., Kitajo, K. & Yamaguchi, A. Treatment with a Global Methyltransferase Inhibitor Induces the Intranuclear Aggregation of ALS-Linked

- FUS Mutant In Vitro. *Neurochem. Res.* **41**, 826–835 (2016).
92. Dion, P. A., Daoud, H. & Rouleau, G. A. Genetics of motor neuron disorders: New insights into pathogenic mechanisms. *Nat. Rev. Genet.* **10**, 769–782 (2009).
 93. Bosco, D. A. *et al.* Mutant FUS proteins that cause amyotrophic lateral sclerosis incorporate into stress granules. *Hum. Mol. Genet.* **19**, 4160–4175 (2010).
 94. Murakami, T. *et al.* Als mutations in FUS cause neuronal dysfunction and death in *Caenorhabditis elegans* by a dominant gain-of-function mechanism. *Hum. Mol. Genet.* **21**, 1–9 (2012).
 95. Scaramuzzino, C. *et al.* Protein Arginine Methyltransferase 1 and 8 Interact with FUS to Modify Its Sub-Cellular Distribution and Toxicity In Vitro and In Vivo. *PLoS One* **8**, (2013).
 96. Lammerding, J. *et al.* Lamins a and C but not lamin B1 regulate nuclear mechanics. *J. Biol. Chem.* **281**, 25768–25780 (2006).
 97. Ho, C. Y. & Lammerding, J. Lamins at a glance. *J. Cell Sci.* **125**, 2087–2093 (2012).
 98. Kolb, T. *et al.* Optomechanical measurement of the role of lamins in whole cell deformability. *J. Biophotonics* **8**, 1–9 (2017).
 99. Geiger, S. K. *et al.* Incomplete nonsense-mediated decay of mutant lamin A/C mRNA provokes dilated cardiomyopathy and ventricular tachycardia. *J. Mol. Med. (Berl)*. **86**, 281–9 (2008).
 100. Ding, X. *et al.* On-chip manipulation of single microparticles, cells, and organisms using surface acoustic waves. *Proc. Natl. Acad. Sci.* **109**, 11105–11109 (2012).
 101. Chan, C. J., Li, W., Cojoc, G. & Guck, J. Volume Transitions of Isolated Cell Nuclei Induced by Rapid Temperature Increase. *Biophys. J.* **112**, 1063–1076 (2017).
 102. Imoto, N., Yoshizawa, N. & Tsuchiya, H. Birefringence in Singlemode Optical Fiber due to Elliptical Core Deformation and Stress Anisotropy. *IEEE J. Quantum Electron.* **16**, 1267–1271 (1980).
 103. Ramachandran, S. & Kristensen, P. Optical vortices in fiber. *Nanophotonics* **2**, 455–474 (2013).

104. Hong, Z., Fu, S., Yu, D., Tang, M. & Liu, D. All-Fiber Tunable LP₁₁ Mode Rotator With 360° Range. *IEEE Photonics J.* **8**, (2016).
105. Leon-Saval, S. G. *et al.* Mode-selective photonic lanterns for space-division multiplexing. *Opt. Express* **22**, 1036–1044 (2014).
106. Kim, B. Y. & Blake, J. N. All-fiber acousto-optic frequency shifter. **11**, 389–391 (1986).
107. Zhao, Y., Liu, Y., Wen, J. & Wang, T. Mode converter based on the long period fiber gratings written in two mode fiber. *2015 Opto-Electronics Commun. Conf. OECC 2015* **24**, 4580–4588 (2015).
108. Lefevre, H. C. Single-mode fibre fractional wave devices and polarisation controllers. *Electron. Lett.* **16**, 778 (1980).
109. T. A. Birks, I. Gris-Sánchez, S. Yerolatsitis, S. G. Leon-Saval, R. R. T. The photonic lantern. *Adv. Opt. Photonics* **7**, 293–339 (2015).
110. Amado M. Velázquez-Benítez. Optical trapping and micromanipulation with a photonic lantern mode multiplexer. *Opt. Lett.* **43**, 1303–1306 (2018).
111. Ulrich, R. Polarization stabilization on single-mode fiber. *Appl. Phys. Lett.* **35**, 840–842 (1979).
112. Johnson, M. Applied Optics Letters to the Editor. *Appl. Opt.* **18**, 504–505 (1979).
113. Noe, R., Heidrich, H. & Hoffmann, D. Endless Polarization Control Systems for Coherent Optics. *J. Light. Technol.* **6**, 1199–1208 (1988).
114. Honmou, H. *et al.* Stabilisation of Heterodyne Receiver Sensitivity with Automatic Polarisation Control System. *Electron. Lett.* **22**, 1181–1182 (1986).
115. Yan, L. Improved beam uniformity in multimode fibers using piezoelectric-based spatial mode scrambling for medical applications. *Opt. Eng.* **47**, 090502 (2008).
116. Chakravarthy, T. P., Naik, D. N. & Viswanathan, N. K. Geometric phase due to orbit-orbit interaction: rotating LP₁₁ modes in a two-mode fiber. (2017).
117. Holleczek, A., Aiello, A., Gabriel, C., Marquardt, C. & Leuchs, G. Classical and quantum properties of cylindrically polarized states of light. **19**, 9714–9736

- (2010).
118. Holzapfel, C., Vienken, J. & Zimmermann, U. Rotation of cells in an alternating electric field: theory and experimental proof. *J. Membr. Biol.* **67**, 13–26 (1982).
 119. Benhal, P., Chase, J. G., Gaynor, P., Oback, B. & Wang, W. AC electric field induced dipole-based on-chip 3D cell rotation. *Lab Chip* **14**, 2717–27 (2014).
 120. Shelby, J. P. & Chiu, D. T. Controlled rotation of biological micro- and nano-particles in microvortices. *Lab Chip* **4**, 168–170 (2004).
 121. Hayakawa, T., Sakuma, S. & Arai, F. On-chip 3D rotation of oocyte based on a vibration-induced local whirling flow. *Microsystems Nanoeng.* **1**, 15001 (2015).
 122. Bernard, I. *et al.* Lab on a Chip particles or living cells by surface acoustic waves †. *Lab Chip* **17**, 2470–2480 (2017).
 123. Miao, Q. *et al.* Dual-mode optical projection tomography microscope using gold nanorods and hematoxylin-stained cancer cells. *Opt. Lett.* **35**, 1037–1039 (2010).
 124. Miao, Q., Reeves, A. P., Patten, F. W. & Seibel, E. J. Multimodal 3D imaging of cells and tissue, bridging the gap between clinical and research microscopy. *Ann. Biomed. Eng.* **40**, 263–276 (2012).
 125. Habaza, M., Gilboa, B., Roichman, Y. & Shaked, N. T. Tomographic phase microscopy with 180° rotation of live cells in suspension by holographic optical tweezers. *Opt. Lett.* **40**, 1881 (2015).
 126. Habaza, M., Gilboa, B., Roichman, Y. & Shaked, N. T. Tomographic phase microscopy with 180° rotation of live cells in suspension by holographic optical tweezers. *Opt. Lett.* **40**, 1881 (2015).
 127. Zhang, Y. *et al.* Multi-Dimensional Manipulation of Yeast Cells Using a LP21 Mode Beam. *J. Light. Technol.* **32**, 1098–1103 (2014).
 128. Kolb, T., Albert, S., Haug, M. & Whyte, G. Optofluidic rotation of living cells for single-cell tomography. *J. Biophotonics* **8**, 1–8 (2014).
 129. Black, B. J. & Mohanty, S. K. Fiber-optic spanner. *Opt. Lett.* **37**, 5030 (2012).
 130. Beebe, D. J., Mensing, G. A. & Walker, G. M. Physics and Applications of

- Microfluidics in Biology. *Annu. Rev. Biomed. Eng.* **4**, 261–286 (2002).
131. Martienssen, W. & Warlimont, H. *Springer Handbook of Condensed Matter and Materials Data*. (2005).
132. Thalhammer, G., Steiger, R., Bernet, S. & Ritsch-Marte, M. Optical macro-tweezers: trapping of highly motile micro-organisms. *J. Opt.* **13**, 044024 (2011).
133. Shvedov, V. G. *et al.* Giant optical manipulation. *Phys. Rev. Lett.* **105**, 1–4 (2010).
134. Fennema, E., Rivron, N., Rouwkema, J., van Blitterswijk, C. & De Boer, J. Spheroid culture as a tool for creating 3D complex tissues. *Trends Biotechnol.* **31**, 108–115 (2013).
135. Thoma, C. R., Zimmermann, M., Agarkova, I., Kelm, J. M. & Krek, W. 3D cell culture systems modeling tumor growth determinants in cancer target discovery ☆. *Adv. Drug Deliv. Rev.* **69–70**, 29–41 (2014).
136. Skardal, A., Shupe, T. & Atala, A. chip systems for drug screening and disease modeling. *Drug Discov. Today* **21**, 1399–1411 (2016).
137. Tuchin, V. V. Polarized light interaction with tissues. *J. Biomed. Opt.* **21**, 071114 (2016).
138. Kharfi, F. & Kharfi, F. Mathematics and Physics of Computed Tomography (CT): Demonstrations and Practical Examples. *Imaging Radioanal. Tech. Interdiscip. Res. Cut. Edge Appl.* 82–106 (2013). doi:10.5772/52351
139. Wada, M., Shimazaki, K. & Iino, M. *Light Sensing in Plants*. (Springer Tokyo, 2005).
140. Randel, N. Phototaxis and the origin of visual eyes. (2015).
141. Kenneth, W. & Smyth, R. D. Light Antennas in Phototactic Algae. **44**, 572–630 (1980).
142. Schaller, K., David, R. & Uhl, R. How Chlamydomonas Keeps Track of the Light Once It Has Reached the Right Phototactic Orientation. *Biophys. J.* **73**, 1562–1572 (1997).
143. Colombelli, J., Hausen, H., Guy, K., Stelzer, E. & Arendt, D. Mechanism of

- phototaxis in marine zooplankton. **456**, 395–400 (2008).
144. Minchinton, A. I. & Tannock, I. F. Drug penetration in solid tumours. **6**, 583–592 (2006).
145. Dhenain, M., Ruffins, S. W. & Jacobs, R. E. Three-dimensional digital mouse atlas using high-resolution MRI. *Dev. Biol.* **232**, 458–470 (2001).